COMPOSITIONAL MEASUREMENTS OF SATURN'S UPPER ATMOSPHERE AND RINGS FROM CASSINI INMS

by

Joseph Serigano IV

A dissertation submitted to Johns Hopkins University

in conformity with the requirements for the degree of

Doctor of Philosophy

Baltimore, Maryland

July, 2021

Abstract

In September 2017, the Cassini-Huygens mission to the Saturn system came to an end as the spacecraft intentionally entered the planet's atmosphere. Prior to entry, the spacecraft executed a series of 22 highly inclined orbits, the Grand Finale orbits, through the previously unexplored region between Saturn and its innermost D ring, yielding the first in situ measurements of the planet's upper atmosphere and ring system. During these orbits, measurements from the Ion and Neutral Mass Spectrometer (INMS) revealed that the composition of Saturn's thermosphere is intricately connected to Saturn's D ring and much more chemically complex than previously believed. These measurements enable the investigation of the composition of the upper atmosphere and rings, the thermal structure and energetics of the upper atmosphere, and the transfer of material from the rings to the atmosphere.

In this thesis, we provide an in-depth compositional analysis of the mass spectra returned from INMS during Cassini's deepest Grand Finale orbits into Saturn's atmosphere. This includes four orbits that measured the isothermal region of Saturn's thermosphere (orbits 288, 290, 291, and 292) and atmospheric entry (orbit 293), which probed approximately 200 km deeper than

the other orbits and detected an increase in temperature in Saturn's thermosphere. Signal returned from the instrument includes native Saturn species, as expected, as well as a significant amount of signal attributed to ices and higher mass organics believed to be flowing into Saturn's atmosphere from the rings.

We identify species present in the spectra using a mass spectral deconvolution algorithm specifically designed to handle unit resolution spaceflight mass spectrometry data when limited calibration data is available. The retrieved mixing ratio and density profiles suggest that many species exhibit behavior indicative of an external source that is likely Saturn's innermost D ring, and that this ring material heavily influences Saturn's thermospheric composition. We use a 1-D diffusion model to analyze the distribution of species and calculate the downward external flux and mass deposition rates of ring volatile species into Saturn's atmosphere. During these observations ring material was being deposited into Saturn's equatorial region at a rate on the order of 10^4 kg/s. An influx of such magnitude would deplete the D ring on the order of thousands of years, leading to the speculation that the influx must be caused by a transient phenomenon that could be a consequence of recent perturbations in the region. This influx of material could have far reaching implications on the energetics, dynamics, and temperature structure in this region and could influence haze and cloud production in Saturn's atmosphere. These analyses are vital to improve our understanding of the interactions between Saturn and its rings, and the results are critical to advance photochemical modeling efforts of Saturn's upper atmosphere.

Thesis Committee

Primary Readers

Sarah Hörst (Primary Advisor)
      Associate Professor
      Department of Earth and Planetary Sciences
      Johns Hopkins University Krieger School of Arts and Sciences

Sabine Stanley
      Bloomberg Distinguished Professor
      Department of Earth and Planetary Sciences
      Johns Hopkins University Krieger School of Arts and Sciences

Acknowledgments

I'd like to thank my advisor, Sarah Hörst, whose incredible knowledge of Titan and the rest of the Saturn system always inspired me to be a better scientist. I'd also like to thank Chao He, my unofficial second advisor, who was an integral part of this work and always took time out of his busy days to help. I am grateful for all of the laughter, support, and intriguing science conversations with my fellow group members Xinting Yu, Michael Radke, Sarah Moran, Kristin Sotzen, and the rest of my planetary family in the department. I'd especially like to thank Sabine Stanley, Kevin Lewis, and Darrell Strobel who, along with Sarah, provided a welcoming and inclusive environment and a strong planetary science foundation through the courses they taught. It's been a privilege to work beside and learn from my collaborators throughout the research presented here: Thomas Gautier, Roger Yelle, Tommi Koskinen, and Melissa Trainer. This thesis would not have been possible without the extraordinary work of the Cassini-Huygens team. This mission came to fruition before I was even born and I'm so grateful to have been able to witness the amazing end.

My decision to pursue a Ph.D. at JHU is largely due to the unwavering support from my first advisor in planetary science, Conor Nixon, and the

rest of my colleagues at NASA Goddard Spaceflight Center. My journey into planetary science started with a summer internship with Conor after finishing my undergraduate degree from Boston University. I knew very little about Titan and was quickly thrown into a group of intimidatingly smart scientists but I felt like a full member of that team from day one. I was lucky enough to continue working with that group after the summer internship, culminating in my first lead author paper a year later which included the discovery of $C^{17}O$ in Titan's atmosphere. My deepest thanks to Conor, Martin Cordiner, Pat Irwin, Nick Teanby, Steven Charnley, Johan Lindberg, and the other incredible people on the Titan ALMA and NEMESIS teams. I'd especially like to thank Ned Molter and Xander Thelen who also joined the Titan ALMA team as interns and provided a great deal of laughter and support throughout the years.

To Mariah and Gaige, who kept me sane throughout my time at Hopkins and were always there for me, I could not have done this without you. An extra special thank you to Mariah, who put up with me as an officemate and was there for me every step of the way. You taught me how to actually appreciate Mars (no matter how boring it is!) and that it's okay to indulge in drinks that are way too sweet and foods that are way too salty. I truly would have been lost without you. And, of course, to Tommy - thank you for supporting me through my most stressed and depressed times. It means the world to me.

This thesis would not have been possible without the unwavering support from my family. I dedicate this to them. To my grandparents, who always

encouraged me to pursue whatever I wanted and sat in amazement as I taught them all about Titan at their kitchen table after learning I was offered an internship at Goddard. To my parents, who taught me the meaning of hard work and unconditional love. To my sisters, who are always there for me and shaped me into the person I am today more than they'll ever know.

Table of Contents

List of Tables

List of Figures

Chapter 1

Introduction

The enigmatic Saturn system is a planetary scientist's playground. The success and longevity of the Cassini-Huygens mission has provided the community with a wealth of data spanning nearly half of a Saturnian year and exploring all aspects of the system. The 12 instruments aboard the Cassini spacecraft allowed for in-depth investigations and new discoveries pertaining to the planet's axisymmetric magnetic field, banded atmospheric structure and vibrant storms, unique polar domains, geologically-interesting icy satellites, and extensive ring system whose density waves and spiral patterns driven by periodic gravitational perturbations offer an additional avenue to study the planet's interior.

In September 2017, the mission came to an end as the spacecraft intentionally entered the planet's atmosphere. Prior to entry, the spacecraft executed a series of 22 highly inclined orbits, the Grand Finale orbits (26 April 2017 to 15 September 2017), through the previously unexplored region between Saturn and its innermost D ring, yielding the first in situ measurements of

the planet's upper atmosphere and ring system. During Cassini's final orbits and atmospheric entry, measurements from the Ion and Neutral Mass Spectrometer (INMS) revealed that the composition of Saturn's upper atmosphere is intricately connected to Saturn's D ring and much more chemically complex than previously believed. These INMS measurements, which are the focus of this thesis, enable the investigation of the chemical composition of Saturn's thermosphere and inner rings, the thermal structure and energetics of the upper atmosphere, and the transfer of material from the rings to the atmosphere.

1.1   Saturn's thermosphere

Saturn's thermosphere, the neutral region of the uppermost atmosphere, is characterized by a steep temperature gradient from the mesopause (at a minimum temperature of ~150 K) up to exospheric temperatures ranging from ~400 K at equatorial latitudes and up to 600 K near the poles (Strobel, Koskinen, and Muller-Wodarg, 2018). The dramatic increase in temperature in the thermosphere is due mainly to the rapid decrease in abundance of native CH_4 and other species below the thermosphere that regulate temperature through radiative cooling. Consequently, the start of the thermosphere roughly coincides with Saturn's homopause, the level below which an atmosphere is well-mixed and assumes a scale height ($H = \frac{kT}{mg}$) in accordance with the mean mass of an atmospheric molecule. Above the homopause, the atmosphere is governed by gravitational diffusive separation in which molecules assume scale heights based on their independent masses. Thus, a molecule

2

whose mass is heavier than the bulk atmosphere will decrease in abundance above the homopause more rapidly than a lighter molecule. At the top of the thermosphere, the temperature reaches an asymptotic value, the exospheric temperature (T_∞), due to the strong vertical transfer of heat as a consequence of the very long atomic mean free paths at such high altitudes. The exobase is located around 0.01 nbar (2,500 to 3,000 km above Saturn's 1-bar pressure level) and the homopause is located around 0.01 to 1 μbar, although these locations are variable and highly dependent on latitude and time of observation (Koskinen et al., 2015; Koskinen and Guerlet, 2018).

Prior to Cassini's Grand Finale orbits, the composition of Saturn's thermosphere was expected to be relatively simple. At this level above the homopause Saturn's main constituents, H_2 and He, were expected to dominate the region with minor contributions from H and water group molecules (O, OH, and H_2O). Water group molecules enter Saturn's upper atmosphere from two major sources: the rings and the plumes of Enceladus. Water from the rings are susceptible to atmospheric drag from Saturn's extended exosphere that ultimately leads to an inflow of water near the equator and, alternatively, charged water enters Saturn's mid-latitude regions via magnetic field lines that link the rings to the atmosphere (see e.g., Connerney and Waite (1984), Feuchtgruber et al. (1997), and O'Donoghue et al. (2013)). The plumes of Enceladus produce Saturn's diffuse E ring and supply the Saturn system, including the upper atmospheres of Saturn and Titan, with water group molecules (see e.g., Hörst, Vuitton, and Yelle (2008), Cassidy and Johnson (2010), and Cavalié et al. (2019)).

During Cassini's last few orbits, the spacecraft obtained measurements near the equatorial ring plane at various heights above the planet's 1-bar pressure level with atmospheric entry (orbit 293) returning measurements down to approximately 1 nbar ($\sim$1370 km above the 1-bar pressure level) before losing contact with Earth. Two main objectives during these orbits were to determine the abundances of H_2 and He and characterize any potential interactions between the upper atmosphere and the rings using measurements from INMS. As a result of mass-dependent diffusive separation in the region, it was assumed that only the abundant native species (H_2 and He) would be detected in diffusive equilibrium, while any external water species inflowing from the rings were expected to have a constant mixing ratio with altitude, and any other heavier minor species would be well below the instrument's detection limit. However, the INMS observations revealed a surprisingly large amount of heavier constituents influencing the upper atmosphere, with a great deal of evidence suggesting that a material influx from the rings is the most likely source of these heavier molecules, which will be discussed throughout this thesis.

1.2   The rings of Saturn

The expansive and dynamic rings, depicted in Figure 1.1, provide a unique opportunity to study in close proximity an evolving and structurally complex system akin to many astrophysical disks. The main rings, the A, B, and C rings, span nearly 300,000 km yet have a vertical extent of only tens of meters (Tiscareno and Murray, 2018). They are composed of mostly millimeter- to

meter-sized particles that are constantly colliding and interacting under the influence of their own gravity, producing short-lived aggregates of particles of various shapes that can be tens of meters in size (Tiscareno et al., 2019). Due to the diffuse nature of the ring system and its many small particles, observations of the rings are notoriously difficult. Although Cassini revolutionized our understanding of the rings, instruments aboard the spacecraft lacked the necessary resolution to directly image ring particles, leaving fundamental aspects of particle properties such as size and size distribution, shape, color, and orientation poorly constrained. Despite their massive presence in the Saturn system and decades of dedicated observations, the formation, age, and evolution of the rings still remain largely a mystery.
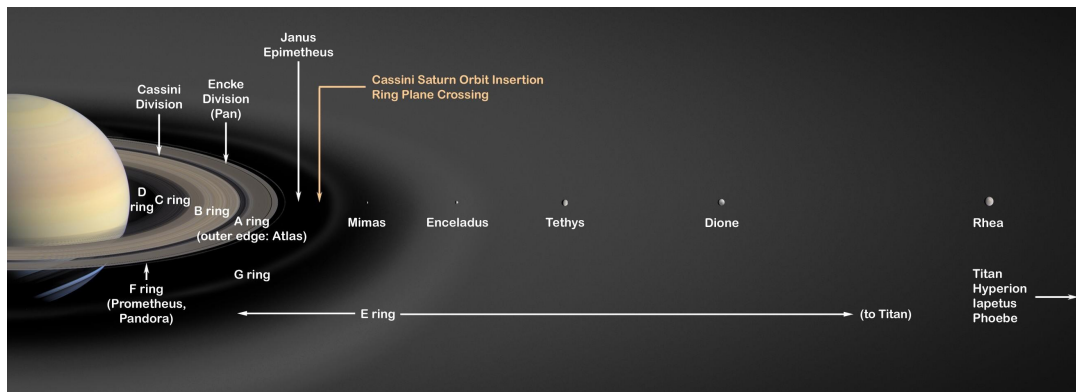
Figure 1.1: Artist's depiction of Saturn's rings and satellites. Cassini's Grand Finale orbits occurred between Saturn and the very faint, innermost D ring. INMS measured an influx of material flowing into Saturn's upper atmosphere and likely originating from the D ring during these orbits. Image credit: NASA/JPL

Saturn's rings are puzzling in a compositional sense as well. While the ring systems of Jupiter, Uranus, and Neptune are composed of primarily dark, dusty material, Saturn's rings appear mostly bright, relatively pristine, and dominated by crystalline water ice (see e.g., Esposito and De Stefano (2018)).

However, spectroscopic observations reveal a spectrum with a steep slope at wavelengths less than 550 nm, indicative of a UV absorbing material intricately mixed with water ice whose origin and composition is still debated (Cuzzi et al., 2018). Proposed compositions include both organic materials (tholin-like complex organics and polycyclic aromatic hydrocarbons) and inorganic materials such as nanophases of iron, hematite, and amorphous carbon (see e.g., Estrada and Cuzzi (1996), Cuzzi and Estrada (1998), Poulet et al. (2003), Cruikshank, Imanaka, and Dalle Ore (2005), and Cuzzi, Filacchione, and Marouf (2018)). Recent analysis of spectra taken with HST-STIS of Saturn's rings suggests that a small fraction of the A and B rings could be composed of complex organics along with some silicate and amorphous carbon, likely from meteoritic infall (Cuzzi et al. (2018)). Ciarniello et al. (2019) modeled observations from Cassini VIMS and came to a similar conclusion that the ring spectra can be reproduced by water ice grains with the inclusion of organics along with variable amounts of carbon, silicates, or other compounds depending on the ring region one is observing. Cassini RADAR and microwave observations from VLA, which probe ring particle composition deeper than surface level, have also provided further evidence of silicates embedded within ring particles (Zhang et al. (2017a), Zhang et al. (2017b), and Zhang et al. (2019)). Despite the range of potential non-water ice materials considered, all studies constrain the non-water ice fraction to be only a few percent by mass, which varies depending on the region one is observing.

The D ring is a very faint region consisting of several ringlets that lie interior to the C ring. Most notable of these is the D68 ringlet, the innermost

narrow ringlet of Saturn. Observational emphasis was placed on this ringlet after 2014 because Cassini's final orbits before atmospheric entry brought the spacecraft to within just a few thousand kilometers of the ringlet (Hedman, 2019). The D ring is very optically thin, $\tau \ll 0.1$, with a "dirtier" (more non-water ice material than other ring regions) and dustier (more micrometer-sized particles) particle population. The faintness and close proximity to Saturn and the C ring, both much brighter, make D ring observations difficult. Models suggest the D ring is depleted in water relative to the main rings, with water ice fractions possibly being below 30% by mass (Hedman and Showalter, 2016). However these values are heavily model dependent and rely on particle shape and size distribution, which are very poorly constrained for this region. The origin of D ring material is not known but it is likely a mix of native material that has drifted inward towards the planet from the main rings (e.g., via viscous spread from the C ring) as well as material from micrometeorite and interplanetary dust bombardment (Cuzzi, Filacchione, and Marouf, 2018). Although poorly constrained in a compositional sense, the D ring is known to be fairly dynamic, with evidence of many perturbing events throughout the years. Observations of the D and C rings have recorded brightness variations and wrapped spiral vertical corrugations due to large interlopers and collisions of larger objects in the region. These events have occurred multiple times in the last few decades, including 1979, two separate events in 1983, 2011, and most recently in 2014 (Hedman et al., 2007; Hedman et al., 2011; Hedman, Burns, and Showalter, 2015; Hedman and Showalter, 2016; Hedman, 2019). Periodic brightness variations due to the 2011 perturbation can be seen in Figure 1.2 from Hedman and Showalter (2016). It is likely that dynamic

events of this nature disrupt the region and trigger the infall of exogenous material in Saturn's equatorial region, which will be discussed throughout this work.
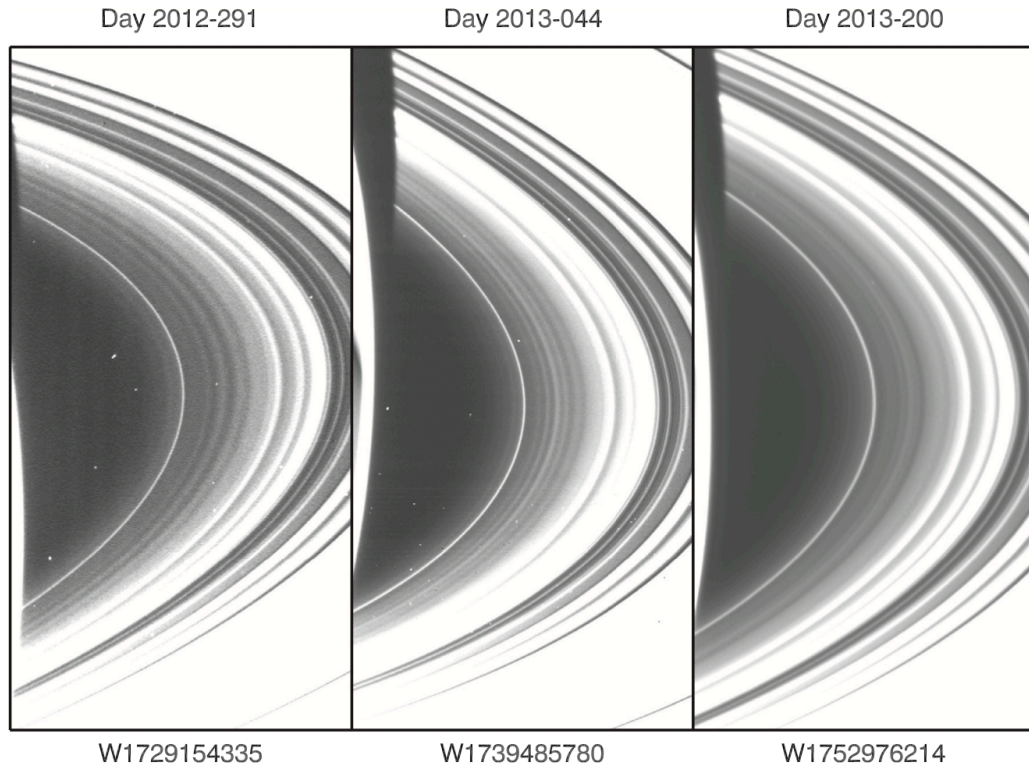
Figure 1.2: Three images of Saturn's D ring showing periodic brightness variations due to sporadic perturbations in the region occurring in December 2011. The bright, narrow ring closest to Saturn (left side of each figure) is the D68 ringlet, the closest ringlet to Saturn. All three images were obtained by Cassini's Wide Angle Camera at similar phase angles, ~176°. Image taken from Hedman and Showalter (2016).

1.3   Ring-atmosphere coupling

Interactions among various bodies in the Saturn system have been noted for decades and evidence for "ring rain" at Saturn, where external material from

the rings enters Saturn's upper atmosphere, has existed since the Voyager era. Using radio occultation data from the Pioneer and Voyager spacecraft, Connerney and Waite (1984) proposed the first ionospheric model of Saturn in which exogenous charged water particles from the rings were used to explain the observed electron density at Saturn. They postulated that the ionospheric electron density, which was an order of magnitude less than previous models predicted, was being depleted by a series of charge exchange reactions with water products. Feuchtgruber et al. (1997) reported the first definitive detection of H_2O in Saturn's upper atmosphere with spectra from the Infrared Space Observatory (ISO), which they attributed to interactions with the rings, icy satellites, and interplanetary dust. More recently, ground based observations from the Keck telescope discovered variations in Saturn's midlatitude H_3^+ intensity that they attribute to the presence of charged species derived from H_2O that were transported to Saturn's midlatitudes via regions of the rings that are magnetically linked to the atmosphere (O'Donoghue et al., 2013; O'Donoghue et al., 2017; O'Donoghue et al., 2019).

The Grand Finale orbits have allowed for in situ analysis of the region between Saturn and its rings for the first time, further revolutionizing our understanding of the rings' composition and influence on Saturn's upper atmosphere. Ionospheric measurements from the Radio and Plasma Wave Science (RPWS) instrument detected a highly variable electron density as a consequence of the rings casting shadow onto Saturn (Wahlund et al. (2018)). Measurements from the Open Source Ion (OSI) mode of the Ion and Neutral Mass Spectrometer (INMS) suggest that the lighter ions detected in Saturn's

ionosphere are likely due to the influence of heavier molecules in the region originating from the rings (Cravens et al. (2019)), an idea which is also supported through recent ionospheric modeling (Moore et al. (2018)). Mitchell et al. (2018) used measurements from Cassini's Magnetospheric Imaging Instrument (MIMI), which measures particles in the mass range 8,000 to 40,000 amu, to conclude that interactions between the upper atmosphere and inner edge of the D ring (mostly atmospheric drag due to collisions with H atoms) resulted in small dust grains entering Saturn's atmosphere from the rings in a narrow region near the equatorial ring plane at a rate of about 5.5 kg/s. Using the Cosmic Dust Analyzer (CDA), which is sensitive to larger particles than MIMI, Hsu et al. (2018) observed a greater influx of exogenous material with a greater latitudinal spread than the MIMI results that reached into Saturn's mid latitude region at rates on the order of 10^2 to 10^3 kg/s. Using INMS in Closed Source Neutral (CSN) mode, Waite et al. (2018) found a surprising amount of non-water ices and higher mass organics entering Saturn's equatorial region from the rings. They conclude that approximately 35% by mass of the inflowing material is organic and that the total mass influx from the rings is on the order of 10^4 kg/s, which was later confirmed by Miller et al. (2020). Comparison to the inflow rates reported by other instruments suggests that the neutral molecules detected by INMS may be the predominant source of inflowing material from the rings (Perry et al. (2018)). We report here further evidence for strong interactions between Saturn and the D ring using measurements from INMS in CSN, which will be outlined in the following Section and detailed throughout this thesis.

1.4 Focus of this work

This thesis presents a compositional analysis of the mass spectra returned by INMS in CSN mode during Cassini's last orbits and atmospheric entry. These measurements directly sampled Saturn's thermosphere and returned a surprising amount of signal that we attribute to volatile ices and high mass organic species as well as native Saturn species. We identify and quantify species present in the spectra using a new, sophisticated mass spectral deconvolution algorithm specifically designed to handle the complexities involved with unit resolution spaceflight mass spectrometry data when limited calibration data is available. We develop a 1-D diffusion model to analyze the distribution of species present in the spectra using results from our deconvolution and calculate the downward external flux and mass deposition rates of ring volatile species into Saturn's atmosphere.

In Chapter 2 I describe the INMS instrument and Grand Finale observations utilized here and in Chapter 3 I detail the methods used to calibrate and correct the raw data. Methods for data reduction are published in Serigano et al. (2020) and further corrections are detailed in Serigano et al. (submitted). The corrected data used throughout this thesis are also found in Yelle et al. (2018), the first Grand Finale INMS publication from our collaboration that focuses on the distribution of H_2, He, and CH_4 in these measurements.

In Chapter 4 I describe the mass spectral deconvolution algorithm we developed to analyze these INMS measurements, as well as the database of species we use to fit the measurements. Results from our deconvolution are found in Chapter 5. Our deconvolution method is published in Gautier et al.

(2020) and utilized in Serigano et al. (2020) and Serigano et al. (submitted). Results in Chapter 5 are found in Serigano et al. (submitted). Serigano et al. (2020) focused on a detailed analysis of INMS measurements in the mass range from m/z 1 to 20 amu. Serigano et al. (submitted) updates and expands on the work presented in Serigano et al. (2020) by using the same approach and analyzing the full mass range of the instrument. This includes an important correction to mass channels associated with H_2O and NH_3 that was not performed in Serigano et al. (2020). For these reasons, the results presented in this thesis focus primarily on the results reported in Serigano et al. (submitted).

In Chapter 6 we use the results from our mass spectral deconvolution to determine the atmospheric mixing ratio and density profiles of species included in the database, which are also found in Serigano et al. (submitted). We use these results to quantify the influx of ring material and mass deposition rates into Saturn's upper atmosphere using our 1-D diffusion model, which is published in Yelle et al. (2018) and detailed in Chapter 7. Finally, we summarize the major findings of this thesis in Chapter 8

Two separate studies have also utilized our corrected INMS data which are not discussed in the contents of this thesis. Müller-Wodarg et al. (2019) further analyze the H_2 density profiles from our work to discover atmospheric waves in Saturn's thermosphere for the first time. They conclude that since wave amplitudes are roughly constant in the sampled region, the waves are likely being damped, which in turn may enhance the eddy friction within the thermosphere and have a significant impact on Saturn's global thermal structure. Additionally, Chadney et al. (submitted) utilize INMS results from

atmospheric entry within an energy deposition model and find that the addition of an influx of CH_4 into Saturn's thermosphere leads to photodissociated products in the region that are crucial to initiate complex organic chemical processes in Saturn's upper atmosphere and lead to the formation of higher mass molecules.

References

Cassidy, TA and RE Johnson (2010). "Collisional spreading of Enceladus' neutral cloud". In: *Icarus* 209.2, pp. 696–703.

Cavalié, Thibault, V Hue, Paul Hartogh, R Moreno, E Lellouch, H Feuchtgruber, Christopher Jarchow, T Cassidy, LN Fletcher, F Billebaud, et al. (2019). "Herschel map of Saturn's stratospheric water, delivered by the plumes of Enceladus". In: *Astronomy & Astrophysics* 630, A87.

Chadney, JM, TT Koskinen, X Hu, M Galand, P Lavvas, YC Unruh, J Serigano, SM Hörst, and RV Yelle (submitted). "Energy deposition in Saturn's equatorial upper atmosphere". In: *Submitted to Icarus*.

Ciarniello, M, G Filacchione, E D'Aversa, F Capaccioni, PD Nicholson, JN Cuzzi, RN Clark, MM Hedman, CM Dalle Ore, P Cerroni, et al. (2019). "Cassini-VIMS observations of Saturn's main rings: II. A spectrophotometric study by means of Monte Carlo ray-tracing and Hapke's theory". In: *Icarus* 317, pp. 242–265.

Connerney, J. E. P. and J. H. Waite (1984). "New model of Saturn's ionosphere with an influx of water from the rings". In: *Nature* 312.5990, p. 136.

Cravens, T. E., L. Moore, J. H. Waite, R. Perryman, M. Perry, J. E. Wahlund, A. Persoon, and W. S. Kurth (2019). "The ion composition of Saturn's equatorial ionosphere as observed by Cassini". In: *Geophysical Research Letters* 46.12, pp. 6315–6321.

Cruikshank, Dale P, Hiroshi Imanaka, and Cristina M Dalle Ore (2005). "Tholins as coloring agents on outer Solar System bodies". In: *Advances in Space Research* 36.2, pp. 178–183.

Cuzzi, J. N., G. Filacchione, and E. A. Marouf (2018). "The Rings of Saturn". In: *Planetary Ring Systems: Properties, Structure, and Evolution*. Ed. by M. S. Tiscareno and C. D.Editor Murray. Cambridge Planetary Science. Cambridge University Press, pp. 51–92. DOI: 10.1017/9781316286791.003.

Cuzzi, J. N., R. G. French, A. R. Hendrix, D. M. Olson, T. Roush, and S. Vahidinia (2018). "HST-STIS spectra and the redness of Saturn's rings". In: *Icarus* 309, pp. 363–388.

Cuzzi, Jeffrey N and Paul R Estrada (1998). "Compositional evolution of Saturn's rings due to meteoroid bombardment". In: *Icarus* 132.1, pp. 1–35.

Esposito, LW and M De Stefano (2018). "Space Age Studies of Planetary Rings". In: *Planetary Ring Systems: Properties, Structure, and Evolution* 19, p. 1.

Estrada, Paul R and Jeffrey N Cuzzi (1996). "Voyager observations of the color of Saturn's rings". In: *Icarus* 122.2, pp. 251–272.

Feuchtgruber, H, E Lellouch, Th de Graauw, B Bézard, Th Encrenaz, and M Griffin (1997). "External supply of oxygen to the atmospheres of the giant planets". In: *Nature* 389.6647, pp. 159–162.

Gautier, T., J. Serigano, J. Bourgalais, S. M. Hörst, and M. G. Trainer (2020). "Decomposition of electron ionization mass apectra for space application using a Monte-Carlo approach". In: *Rapid Communications in Mass Spectrometry* 34.8, e8684.

Hedman, M. M., J. A. Burns, M. R. Showalter, C. C. Porco, P. D. Nicholson, A. S. Bosh, M. S. Tiscareno, R. H. Brown, B. J. Buratti, K. H. Baines, et al. (2007). "Saturn's dynamic D ring". In: *Icarus* 188.1, pp. 89–107.

Hedman, MM (2019). "Bright clumps in the D68 ringlet near the end of the Cassini Mission". In: *Icarus* 323, pp. 62–75.

Hedman, MM, JA Burns, and MR Showalter (2015). "Corrugations and eccentric spirals in Saturn's D ring: New insights into what happened at Saturn in 1983". In: *Icarus* 248, pp. 137–161.

Hedman, MM and MR Showalter (2016). "A new pattern in Saturn's D ring created in late 2011". In: *Icarus* 279, pp. 155–165.

Hedman, MM, JA Burns, MW Evans, MS Tiscareno, and CC Porco (2011). "Saturn's curiously corrugated C ring". In: *Science* 332.6030, pp. 708–711.

Hörst, Sarah M, Véronique Vuitton, and Roger V Yelle (2008). "Origin of oxygen species in Titan's atmosphere". In: *Journal of Geophysical Research: Planets* 113.E10.

Hsu, H-W, J. Schmidt, S. Kempf, F. Postberg, G. Moragas-Klostermeyer, M. Seiß, H. Hoffmann, M. Burton, S. Ye, W. S. Kurth, et al. (2018). "In situ collection of dust grains falling from Saturn's rings into its atmosphere". In: *Science* 362.6410, eaat3185.

Koskinen, T. T. and S. Guerlet (2018). "Atmospheric structure and helium abundance on Saturn from Cassini/UVIS and CIRS observations". In: *Icarus* 307, pp. 161–171.

Koskinen, T. T., B. R. Sandel, R. V. Yelle, D. F. Strobel, I. C. F. Müller-Wodarg, and J. T. Erwin (2015). "Saturn's variable thermosphere from Cassini/UVIS occultations". In: *Icarus* 260, pp. 174–189.

Miller, K. E., J. H. Waite, R. S. Perryman, M. E. Perry, A. Bouquet, B. A. Magee, B. Bolton, T. Brockwell, M. M. Hedman, and C. R. Glein (2020). "Cassini INMS constraints on the composition and latitudinal fractionation of Saturn ring rain material". In: *Icarus* 339, p. 113595.

Mitchell, D. G., M. E. Perry, D. C. Hamilton, J. H. Westlake, P. Kollmann, H. T. Smith, J. F. Carbary, J. H. Waite, R. Perryman, H-W Hsu, et al. (2018). "Dust grains fall from Saturn's D-ring into its equatorial upper atmosphere". In: *Science* 362.6410, eaat2236.

Moore, L., T. E. Cravens, I. C. F. Müller-Wodarg, M. E. Perry, J. H. Waite, R. S. Perryman, A. Nagy, D. Mitchell, A. Persoon, J. E. Wahlund, et al. (2018). "Models of Saturn's equatorial ionosphere based on in situ data from Cassini's Grand Finale". In: *Geophysical Research Letters* 45.18, pp. 9398–9407.

Müller-Wodarg, ICF, TT Koskinen, L Moore, J Serigano, RV Yelle, S Hörst, JH Waite, and M Mendillo (2019). "Atmospheric waves and their possible effect on the thermal structure of Saturn's thermosphere". In: *Geophysical Research Letters* 46.5, pp. 2372–2380.

O'Donoghue, J., L. Moore, J. E. P. Connerney, H. Melin, T. S. Stallard, S. Miller, and K. H. Baines (2017). "Redetection of the Ionospheric Signature of Saturn's 'Ring Rain'". In: *Geophysical Research Letters* 44.23, pp. 11–762.

O'Donoghue, J., T. S. Stallard, H. Melin, G. H. Jones, S. W. H. Cowley, S. Miller, K. H. Baines, and J. S. D. Blake (2013). "The domination of Saturn's low-latitude ionosphere by ring 'rain'". In: *Nature* 496.7444, p. 193.

O'Donoghue, James, Luke Moore, Jack Connerney, Henrik Melin, Tom S Stallard, Steve Miller, and Kevin H Baines (2019). "Observations of the chemical and thermal response of 'ring rain'on Saturn's ionosphere". In: *Icarus* 322, pp. 251–260.

Perry, M. E., J. H. Waite, D. G. Mitchell, K. E. Miller, T. E. Cravens, R. S. Perryman, L. Moore, R. V. Yelle, H-W Hsu, M. M. Hedman, et al. (2018). "Material flux from the rings of Saturn into its atmosphere". In: *Geophysical Research Letters* 45.19, pp. 10–093.

Poulet, F, DP Cruikshank, JN Cuzzi, TL Roush, and RG French (2003). "Compositions of Saturn's rings A, B, and C from high resolution near-infrared spectroscopic observations". In: *Astronomy & Astrophysics* 412.1, pp. 305–316.

Serigano, J, SM Hörst, C He, Thomas Gautier, RV Yelle, TT Koskinen, and MG Trainer (2020). "Compositional Measurements of Saturn's Upper Atmosphere and Rings from Cassini INMS". In: *Journal of Geophysical Research: Planets* 125.8, e2020JE006427.

Serigano, J, SM Hörst, C He, Thomas Gautier, RV Yelle, TT Koskinen, and MG Trainer (submitted). "Compositional Measurements of Saturn's Upper Atmosphere and Rings from Cassini INMS: An Extended Analysis of Measurements from Cassini's Grand Finale Orbits". In: *Submitted to the Journal of Geophysical Research: Planets*.

Strobel, Darrell F, Tommi T Koskinen, and Ingo Muller-Wodarg (2018). "Saturn's Variable Thermosphere". In: *Saturn in the 21st Century* 20, p. 224.

Tiscareno, M. S., P. D. Nicholson, J. N. Cuzzi, L. J. Spilker, C. D. Murray, M. M. Hedman, J. E. Colwell, J. A. Burns, S. M. Brooks, R. N. Clark, et al. (2019). "Close-range remote sensing of Saturn's rings during Cassini's ring-grazing orbits and Grand Finale". In: *Science* 364.6445, eaau1017.

Tiscareno, Matthew S and Carl D Murray (2018). *Planetary ring systems: properties, structure, and evolution*. Cambridge University Press.

Wahlund, J. E., M. W. Morooka, L. Z. Hadid, A. M. Persoon, W. M. Farrell, D. A. Gurnett, G. Hospodarsky, W. S. Kurth, S-Y Ye, D. J. Andrews, et al. (2018). "In situ measurements of Saturn's ionosphere show that it is dynamic and interacts with the rings". In: *Science* 359.6371, pp. 66–68.

Waite, J. H., R. S. Perryman, M. E. Perry, K. E. Miller, J. Bell, T. E. Cravens, C. R. Glein, J. Grimes, M. Hedman, J. Cuzzi, et al. (2018). "Chemical interactions between Saturn's atmosphere and its rings". In: *Science* 362.6410, eaat2382.

Yelle, R. V., J. Serigano, T. T. Koskinen, S. M. Hörst, M. E. Perry, R. S. Perryman, and J. H. Waite (2018). "Thermal structure and composition of Saturn's upper atmosphere from Cassini/Ion Neutral Mass Spectrometer measurements". In: *Geophysical Research Letters* 45.20, pp. 10–951.

Zhang, Z, AG Hayes, MA Janssen, PD Nicholson, JN Cuzzi, I de Pater, DE Dunn, PR Estrada, and MM Hedman (2017a). "Cassini microwave observations provide clues to the origin of Saturn's C ring". In: *Icarus* 281, pp. 297–321.

Zhang, Z, AG Hayes, MA Janssen, PD Nicholson, JN Cuzzi, I de Pater, and DE Dunn (2017b). "Exposure age of Saturn's A and B rings, and the Cassini Division as suggested by their non-icy material content". In: *Icarus* 294, pp. 14–42.

Zhang, Z, AG Hayes, I de Pater, DE Dunn, MA Janssen, PD Nicholson, JN Cuzzi, BJ Butler, RJ Sault, and S Chatterjee (2019). "VLA multi-wavelength

microwave observations of Saturn's C and B rings". In: *Icarus* 317, pp. 518–548.

Chapter 2

Instrument and Observations

2.1 Cassini Ion and Neutral Mass Spectrometer

Measurements presented in this thesis rely on data from the Cassini space-craft's Ion and Neutral Mass Spectrometer (INMS) operating in Closed Source Neutral (CSN) mode. The primary focus of INMS was to characterize the composition, density, and temperature structure of Titan's upper atmosphere and its interaction with Saturn's magnetospheric plasma. The instrument's excellent performance throughout the spacecraft's 13 years in orbit allowed for a large number of studies that drastically improved our understanding of Titan's atmosphere (see e.g., Waite et al. (2005b), Vuitton, Yelle, and Anicich (2006), Vuitton, Yelle, and McEwan (2007), Waite et al. (2007), Vuitton, Yelle, and Cui (2008), Cui, Yelle, and Volk (2008), Cui et al. (2009a), Cui et al. (2009b), Cui et al. (2012), and Waite et al. (2017)). The instrument also directly sampled the plumes of Enceladus multiple times, providing constraints on the composition, density, and structure of the plumes (see e.g., Waite et al. (2006), Waite et al. (2009), Teolis et al. (2010), and Waite et al. (2017)). During

the spacecraft's last orbits, known as the Grand Finale orbits, INMS was used to obtain compositional measurements of the region between Saturn and the inner edge of the D ring. The measurements returned from these Grand Finale orbits have already been utilized in multiple studies (Yelle et al., 2018; Perry et al., 2018; Waite et al., 2018; Miller et al., 2020) and are the focus of this thesis.

In CSN mode, INMS is able to directly sample and analyze the neutral composition of the inflowing gas. A schematic of the instrument, taken from Waite et al. (2004), is shown in Figure 2.1. The material enters a spherical antechamber where it thermally accommodates to the chamber temperature through wall collisions before traveling to an ionization region. The neutral molecules are then ionized by a collimated electron beam at 70 eV, resulting in ionized fragments of the parent molecule that are detected by the instrument. This process produces unique fragmentation patterns for each neutral species based on the composition and structure of the molecule. The resulting ions are deflected onto the instrument's detectors by a dual radio frequency quadrupole mass analyzer which filters the ions according to their mass-to-charge (m/z) ratio. The instrument's dual detector system is electronically biased, with the majority of ions deflected onto the primary detector and a small fraction making it to the low gain secondary detector which is utilized only in instances when the count rate of the primary detector saturates. In this way, the instrument's overall dynamic range of signal detection is increased by about a factor of 1500 (Waite et al., 2004). Data are recorded in mass channels from 1 to 8 and 12 to 99 atomic mass units (amu). The instrument has a mass resolution of M/ΔM of 100 at 10% of the mass peak height and a resolving

power of 1 amu. Thus, the mass spectra returned by INMS is a combination of overlapping signal from all species present in the sample. Determination of the composition of the sample requires accurate knowledge of how each species fragments within the instrument, which can then be used to reconstruct the signal and determine the relative intensities of different species in the measured spectra. A detailed description of the instrument can be found in Waite et al. (2004).
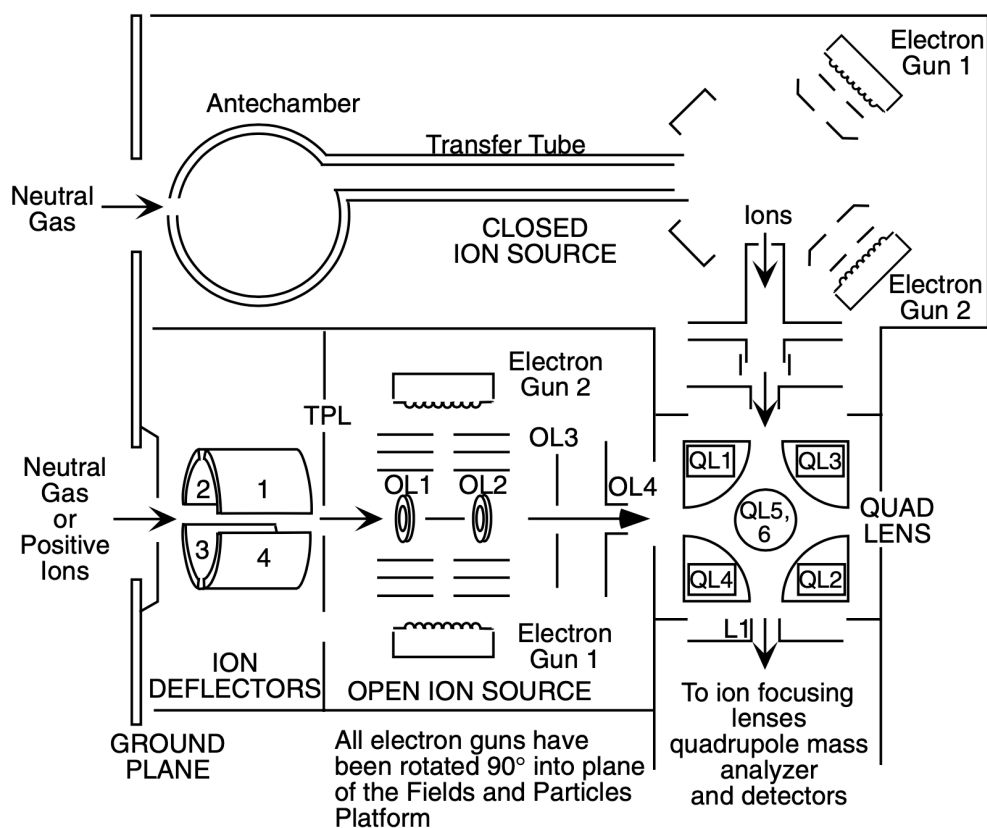
Figure 2.1: A schematic of INMS taken from Waite et al. (2004). In CSN mode, neutral gas enters the antechamber (top left of figure) and thermally accommodates to the chamber temperature through wall collisions. The molecules are then ionized by a 70 eV electron beam and the ionized fragments are detected by the instrument's dual detector system.

2.2 INMS Grand Finale observations of Saturn

This thesis focuses on measurements taken during Cassini Grand Finale orbits 288, 290, 291, 292, and 293. These orbits comprise the last and deepest orbits of Cassini, which directly sampled Saturn's thermosphere, as well as atmospheric entry (orbit 293), which sampled Saturn down to approximately 1370 km above the 1-bar pressure level, or approximately 1 nbar. Orbits 288 to 292 sampled Saturn's atmosphere down to an altitude of about 1600 to 1700 km above Saturn's 1-bar pressure level, or approximately 0.1 nbar. Orbit 289 was not optimized for INMS observations and is not used in this analysis. INMS measurements in mass channel 2 are used to determine the H_2 density in the atmosphere and were taken every $\sim$0.6 s around closest approach (C/A). Measurements in other mass channels of particular interest were taken every $\sim$1 s. The spacecraft's velocity during these orbits was between 30 and 31 km/s. This corresponds to a spatial resolution of 18 km and 30 km, respectively, along the spacecraft trajectory. The raw data associated with this analysis can be found in the Planetary Plasma Interactions (PPI) node of the NASA Planetary Data System (PDS) public archive (https://pds-ppi.igpp.ucla.edu) (Waite et al., 2005a).

The top panels of Figure 2.2 highlight some characteristics of the orbits analyzed here and additional orbital information can be found in Table 2.1. All orbits aside from atmospheric entry (orbit 293) probed similar latitudinal and altitudinal regions in close proximity to the ring plane and near the same local solar time. Thus, one would expect the resulting mass spectra from these orbits to be similar, aside from possible compositional differences
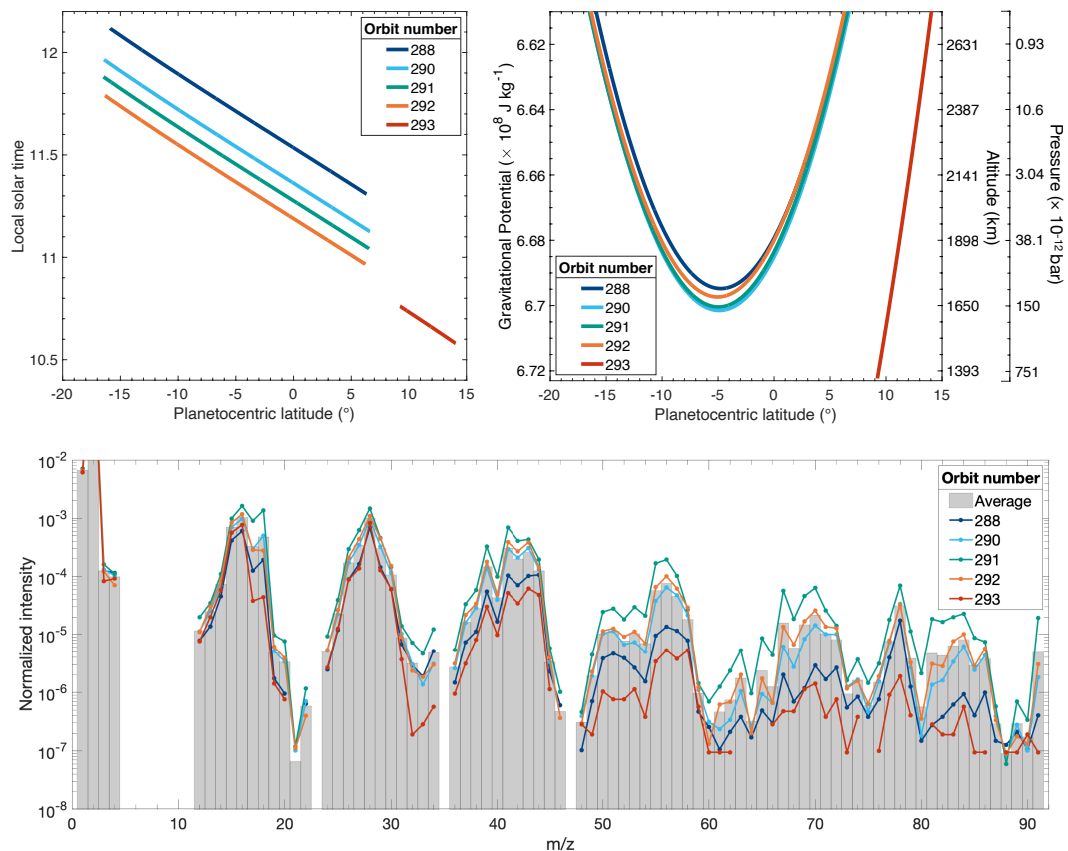
Figure 2.2: Local solar time (top left) and gravitational potential (top right) as function of Saturn planetocentric latitude for the Cassini orbits discuss in this analysis. Pressure and altitude above the 1-bar pressure level of Saturn are presented on the right y axis. All orbits aside from orbit 293 (atmospheric entry) occurred during similar conditions. Bottom: Mass spectra for all orbits normalized to H_2 (*m/z* 2 amu) for comparison.

stemming from general dynamical and temporal fluctuations. All orbits sampled the composition of Saturn's isothermal region of the thermosphere aside from atmospheric entry which returned measurements approximately 200 km lower than the other orbits and detected an increase in temperature in the thermosphere (Yelle et al., 2018). The lower panel of Figure 2.2 shows the resulting mass spectra from these orbits normalized to m/z 2 amu for comparison. The spectra have strong signal at m/z 2 and 4 amu as expected since these mass channels represent H_2 and He, the bulk constituents of Saturn's atmosphere. The spectra also include a surprisingly large signal throughout the entirety of the instrument's mass range due to the coupling of this region of Saturn's atmosphere to the D ring. The complex mass spectra includes signal from various ices and organics, which we attribute to ring material falling into the atmosphere. Mass spectra for all orbits follow a similar trend with slight variations that are likely due to temporal and dynamical fluctuations in the region. For example, the spectrum returned during orbit 291 includes a much larger signal in mass channels attributed to exogenous species while the spectrum returned during atmospheric entry is depleted in these mass channels relative to other orbits.

2.2.1 Other orbits

Although this thesis focuses entirely on measurements returned from the Cassini orbits described above, INMS did measure other regions relevant to our analysis. However, due to the very low signal of these other measurements we do not attempt to analyze these spectra in detail. The signal that is above

Table 2.1: Orbital information for the measurements used in this study. These were the last orbits of the Cassini spacecraft and represented the lowest altitude sampling of Saturn's upper atmosphere. Cassini entered Saturn's atmosphere during orbit 293.

Orbit Number	Date	Latitude (°)	Longitude (°)	LST (hr)	Altitude (km)	Grav. Potential ($\times 10^8$ J kg^{-1})
288	14 August 2017	-4.8	-167.5	11.7	1705	6.695
290	27 August 2017	-4.9	160.5	11.5	1626	6.702
291	2 September 2017	-5.0	-34.0	11.4	1639	6.700
292	9 September 2017	-5.0	130.4	11.4	1675	6.697
293	15 September 2017	9.2	-54.3	10.8	1367	6.722

Note. Values in this table correspond to the spacecraft's closest approach to Saturn. Spacecraft velocity at this time was between 30.1 to 31 km/s for these orbits. LST = local solar time.

the background in these observations provides additional evidence of the non-water ice composition of the rings, which will be discussed throughout this thesis. These measurements are shown in Figure 2.3 and include mass spectra from the F ring-grazing orbits (C/A ~2.47 R_S) as well as middle (C/A ~2840 km) and high (C/A ~3400 km) altitude orbits between Saturn and the D ring. The F ring-grazing spectrum is a combination of measurements from Cassini orbits 256, 258, 265, 267, and 268, the middle altitude spectrum is a combination of measurements from orbits 271 to 275 and 283 to 287, and the high altitude spectrum is a combination of measurements from orbits 278 to 280. Mass channels that are consistently above the noise level include channels associated with H_2, CH_4, 28 amu (mostly CO and N_2), and CO_2.

A schematic from NASA/JPL detailing the trajectory of all the Grand Finale orbits relative to Saturn can be found in Figure 2.4. The green orbits, which represent the start of the Grand Finale phase of the mission, represent the F ring grazing measurements shown in the top panel of Figure 2.3. The blue orbits consist of the middle and high orbits as well as the lower orbit passes detailed in this thesis. The red trajectory represents atmospheric entry into Saturn, orbit 293.

2.2.2 Potential contamination

Of great concern with INMS neutral measurements is the potential for contamination from previous measurements to create false signal during subsequent encounters. Particularly, certain organics from Titan's atmosphere have the potential to adhere to the walls of the INMS antechamber and contribute to
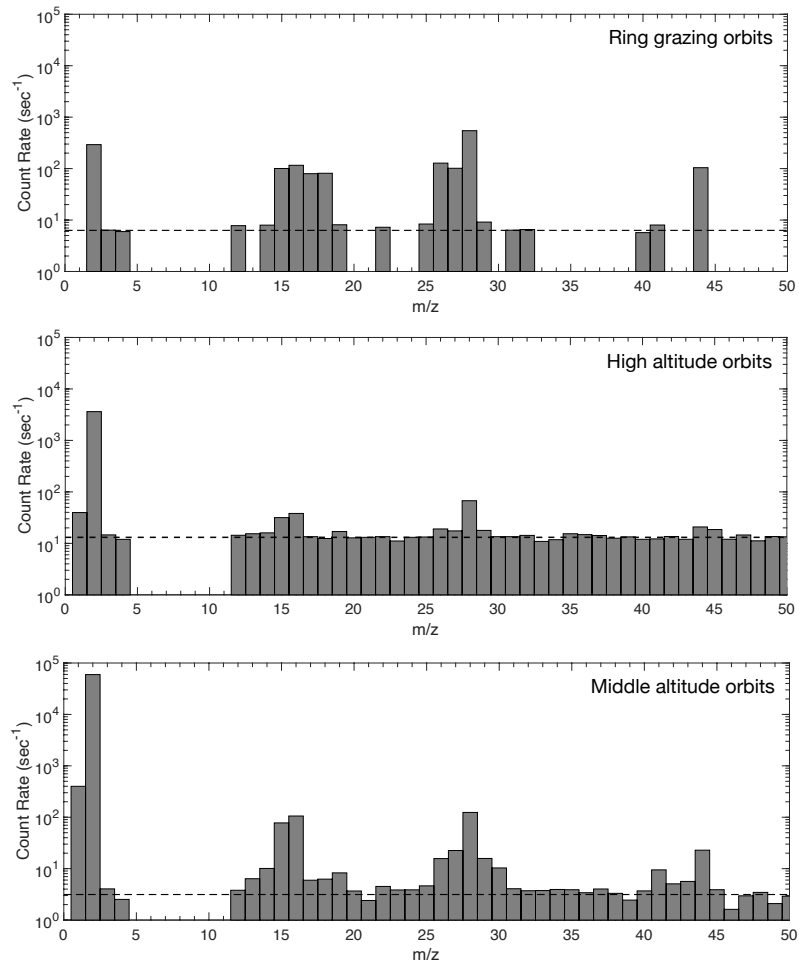
Figure 2.3: Mass spectra from the F ring-grazing orbits (C/A $\sim$2.47 R$_S$) as well as middle (C/A $\sim$2840 km) and high (C/A $\sim$3400 km) altitude orbits between Saturn and the D ring. The F ring-grazing spectrum is a combination of measurements from Cassini orbits 256, 258, 265, 267, and 268. Middle altitude spectrum is a combination of measurements from orbits 271 to 275 and 283 to 287. High altitude spectrum is a combination of measurements from orbits 278 to 280. Spectra from these orbits are much lower in signal, however mass channels that are consistently above the noise level include channels associated with H_2, CH_4, 28 amu (mostly CO/N_2), and CO_2. All channels above *m/z* 50 amu are at the noise level.
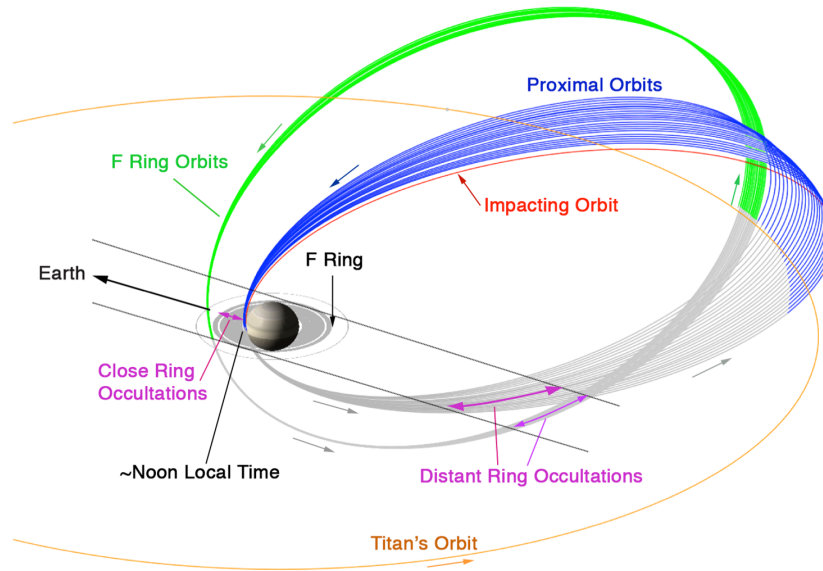
Figure 2.4: Trajectory of the Grand Finale orbits of Cassini. Image from NASA/JPL.

the signal of a subsequent encounter at a later time. Contamination from a previous target would culminate in two ways: (1) a similar signal from the contaminating source as compared to the signal detected at the new source, which could correspond to signal from fragmented material that had adhered to the instrument walls, and (2) a larger signal in the contaminated mass channels at the original source as compared to the new source. Figure 2.5 compares INMS measurements obtained at Saturn during orbit 290 to measurements taken during the Titan T30 flyby, which recorded measurements down to approximately 960 km ($\sim$0.5 nbar, similar to pressure conditions at Saturn), and the Enceladus E5 flyby, the highest signal to noise encounter of the Enceladus plumes. The mass spectra from different environments are distinct and do not follow similar trends. This is especially notable in the

$m/z \sim 12$ to 20 amu region where the highest signal occurs in different mass channels for all encounters: m/z 14 amu at Titan (N_2), m/z 16 amu at Saturn (CH_4 and H_2O), and m/z 18 amu at Enceladus (H_2O). Additionally, at higher masses ($> m/z \sim 50$ amu) where contamination from Titan organics is most likely, the heavier organic signal at Titan deviates significantly from the signal obtained at Saturn. Particularly, the region surrounding the peak near m/z 50 amu at Titan is not present in the Saturn measurements. Additionally, certain regions in the Saturn measurements (near m/z 56 amu and 70 amu) are absent from the Titan observations. We conclude through comparison of these mass spectra at different environments that contamination from Titan is likely insignificant.
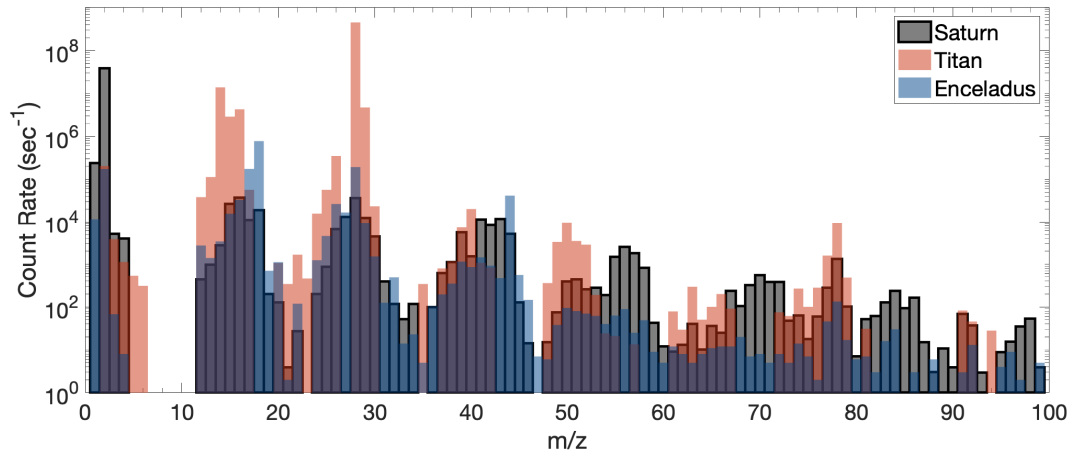
Figure 2.5: Comparison of INMS mass spectra from Saturn (orbit 290, grey), Titan (T30 flyby, red), and Enceladus (E5 flyby, blue). Variation of signal among targets suggests that contamination within the instrument is not significant.

2.2.3 Spacecraft speed

Cassini orbited Saturn at $\sim$30 km/s during these final observations, approximately 5 times faster than typical Titan flybys. As a consequence, the energy associated with the interaction between molecules entering the antechamber and the walls of the instrument was much higher than typical interactions. Such energetic impacts could dissociate molecules entering the instrument's antechamber before ionization, which could potentially result in fragments of molecules larger than the INMS mass range contributing to the observed signal. However, as noted in Waite et al. (2018), studies of surface-induced dissociation indicate that only about 25% of the impact energy is converted to internal energy of the molecule in the collision process (Maaijer-Gielbert et al., 1998). This translates to approximately 1.25 eV of added kinetic energy per nucleon based on the spacecraft's speed at the time of these orbits, which would be sufficient to dissociate some incoming larger nanograins. Thus, it is likely that a fraction of the signal is from fragments of larger molecules however, as seen in Figure 2.2, signal drops significantly at higher masses: two to three orders of magnitude when comparing the signal around *m/z* 12 amu to that of the highest mass channels. Thus, fragments of larger molecules would not have a very significant impact on the measured abundances of lower mass species such as the lighter species native to Saturn and the volatile ices detected in the spectrum. Other recent studies also find no significant effects on the measurements from the spacecraft's high speed (Yelle et al., 2018; Perry et al., 2018; Miller et al., 2020) and our analysis here shows no evidence of issues stemming from the spacecraft's speed.

2.2.4   Gravitational potential units

Saturn's high rotation rate and significantly oblate shape invalidates the common assumption that atmospheric variations are purely radial, and instead adds a latitudinal component to atmospheric properties. We assume here that Saturn's atmospheric properties vary with gravitational potential, ϕ, and that constant potential surfaces are isobars and we use ϕ as the vertical coordinate in our analysis. This modification, first detailed in Yelle et al. (2018), includes adopting the gravitational potential for Saturn found in Anderson and Schubert (2007). We adopt the standard Legendre expansion of the gravitational potential:

$$\phi = \frac{GM}{r}\left(1 - \sum_{n=1}^{4}\left(J_{2n}P_{2n}(\sin(\theta))\left(\frac{r_{\text{eq}}}{r}\right)^{2n}\right)\right) - \frac{1}{2}(r\cos(\theta)\Omega)^2 \qquad (2.1)$$

where G is the gravitational constant, M is the mass of Saturn, r is the radial distance from Saturn, r_{eq} is Saturn's equatorial radius, Ω is the atmosphere's rotation rate, θ is the latitude, J_{2n} are the expansion coefficients that describe the departure of the gravitational field from spherical symmetry, and P_{2n} are the Legendre polynomials. Numerical values for these quantities are taken from Anderson and Schubert (2007) and are listed in Table 2.2. Expressing the vertical coordinate as a function of gravitational potential allows us to construct a temperature profile that is independent of latitude, which will be further discussed in Chapter 5. The pressure level and the altitude above the 1-bar pressure level that correspond to the gravitational potential field used here can be found on the right y-axis of figures when appropriate.

Table 2.2: Parameters for Saturn's gravitational field. Values are taken from Anderson and Schubert (2007).

Parameter	Value
GM	3.793×10^{16} J m kg^{-1}
Ω	1.655×10^{-4} s^{-1}
r_{eq}	6.033×10^{7} m
J_2	1.629×10^{-2}
J_4	-9.355×10^{-4}
J_6	8.53×10^{-5}
J_8	-1.0×10^{-5}

References

Anderson, J. D. and G. Schubert (2007). "Saturn's gravitational field, internal rotation, and interior structure". In: *Science* 317.5843, pp. 1384–1387.

Cui, J., R. V. Yelle, and K. Volk (2008). "Distribution and escape of molecular hydrogen in Titan's thermosphere and exosphere". In: *Journal of Geophysical Research: Planets* 113.E10.

Cui, J., R. V. Yelle, V. Vuitton, J. H. Waite, W. T. Kasprzak, D. A. Gell, H. B. Niemann, I. C. F. Müller-Wodarg, N. Borggren, G. G. Fletcher, et al. (2009a). "Analysis of Titan's neutral upper atmosphere from Cassini Ion Neutral Mass Spectrometer measurements". In: *Icarus* 200.2, pp. 581–615.

Cui, J., M. Galand, R. V. Yelle, V. Vuitton, J. E. Wahlund, P. P. Lavvas, I. C. F. Müller-Wodarg, T. E. Cravens, W. T. Kasprzak, and J. H. Waite (2009b). "Diurnal variations of Titan's ionosphere". In: *Journal of Geophysical Research: Space Physics* 114.A6.

Cui, J., R. V. Yelle, D. F. Strobel, I. C. F. Müller-Wodarg, D. S. Snowden, T. T. Koskinen, and M. Galand (2012). "The CH_4 structure in Titan's upper atmosphere revisited". In: *Journal of Geophysical Research: Planets* 117.E11.

Maaijer-Gielbert, Janine de, Árpád Somogyi, Vicki H Wysocki, Piet G Kistemaker, and Tina L Weeding (1998). "Surface-induced dissociation of diphenyl ether". In: *International journal of mass spectrometry and ion processes* 174.1-3, pp. 81–94.

Miller, K. E., J. H. Waite, R. S. Perryman, M. E. Perry, A. Bouquet, B. A. Magee, B. Bolton, T. Brockwell, M. M. Hedman, and C. R. Glein (2020). "Cassini INMS constraints on the composition and latitudinal fractionation of Saturn ring rain material". In: *Icarus* 339, p. 113595.

Perry, M. E., J. H. Waite, D. G. Mitchell, K. E. Miller, T. E. Cravens, R. S. Perryman, L. Moore, R. V. Yelle, H-W Hsu, M. M. Hedman, et al. (2018). "Material flux from the rings of Saturn into its atmosphere". In: *Geophysical Research Letters* 45.19, pp. 10–093.

Teolis, B. D., M. E. Perry, B. A. Magee, J. Westlake, and J. H. Waite (2010). "Detection and measurement of ice grains and gas distribution in the Enceladus plume by Cassini's Ion Neutral Mass Spectrometer". In: *Journal of Geophysical Research: Space Physics* 115.A9.

Vuitton, V., R. V. Yelle, and J. Cui (2008). "Formation and distribution of benzene on Titan". In: *Journal of Geophysical Research: Planets* 113.E5.

Vuitton, V, RV Yelle, and VG Anicich (2006). "The nitrogen chemistry of Titan's upper atmosphere revealed". In: *The Astrophysical Journal Letters* 647.2, p. L175.

Vuitton, V, RV Yelle, and MJ McEwan (2007). "Ion chemistry and N-containing molecules in Titan's upper atmosphere". In: *Icarus* 191.2, pp. 722–742.

Waite, J. H., C. R. Glein, R. S. Perryman, B. D. Teolis, B. A. Magee, G. Miller, J. Grimes, M. E. Perry, K. E. Miller, A. Bouquet, et al. (2017). "Cassini finds molecular hydrogen in the Enceladus plume: evidence for hydrothermal processes". In: *Science* 356.6334, pp. 155–159.

Waite, J. H., M. R. Combi, W-H Ip, T. E. Cravens, R. L. McNutt, W. Kasprzak, R. V. Yelle, J. G. Luhmann, H. B. Niemann, D. A. Gell, et al. (2006). "Cassini Ion and Neutral Mass Spectrometer: Enceladus plume composition and structure". In: *Science* 311.5766, pp. 1419–1422.

Waite, J. H., W. T. Kasprzak, J. G. Luhman, T. E. Cravens, R. V. Yelle, R. L. McNutt, W-H Ip, R. L. Thorpe, and D. A. Gell (2005a). "CASSINI S INMS LEVEL 1A EXTRACTED DATA V1.0". In: *NASA Planetary Data System* CO-S-INMS-3-L1A-U-V1.0.

Waite, J. H., R. S. Perryman, M. E. Perry, K. E. Miller, J. Bell, T. E. Cravens, C. R. Glein, J. Grimes, M. Hedman, J. Cuzzi, et al. (2018). "Chemical interactions between Saturn's atmosphere and its rings". In: *Science* 362.6410, eaat2382.

Waite, J. H., H. B. Niemann, R. V. Yelle, W. T. Kasprzak, T. E. Cravens, J. G. Luhmann, R. L. McNutt, W-H Ip, D. A. Gell, V. De La Haye, et al. (2005b). "Ion Neutral Mass Spectrometer results from the first flyby of Titan". In: *Science* 308.5724, pp. 982–986.

Waite, J. H., W. S. Lewis, B. A. Magee, J. I. Lunine, W. B. McKinnon, C. R. Glein, O. Mousis, D. T. Young, T. Brockwell, J. Westlake, et al. (2009). "Liquid water on Enceladus from observations of ammonia and ^{40}Ar in the plume". In: *Nature* 460.7254, p. 487.

Waite, J. H., W. S. Lewis, W. T. Kasprzak, V. G. Anicich, B. P. Block, T. E. Cravens, G. G. Fletcher, W-H Ip, J. G. Luhmann, R. L. McNutt, et al. (2004). "The Cassini Ion and Neutral Mass Spectrometer (INMS) investigation". In: *The Cassini-Huygens Mission*. Springer, pp. 113–231.

Waite, J. H., D. T. Young, T. E. Cravens, A. J. Coates, F. J. Crary, B. Magee, and J. Westlake (2007). "The process of tholin formation in Titan's upper atmosphere". In: *Science* 316.5826, pp. 870–875.

Yelle, R. V., J. Serigano, T. T. Koskinen, S. M. Hörst, M. E. Perry, R. S. Perryman, and J. H. Waite (2018). "Thermal structure and composition of Saturn's upper atmosphere from Cassini/Ion Neutral Mass Spectrometer measurements". In: *Geophysical Research Letters* 45.20, pp. 10–951.

Chapter 3

Data Reduction

Although INMS has been extensively characterized for studies of Titan's N_2-dominated atmosphere (see e.g., Yelle et al. (2006), Yelle, Cui, and Müller-Wodarg (2008), Müller-Wodarg et al. (2008), Cui, Yelle, and Volk (2008), Cui et al. (2009a), Cui et al. (2009b), Magee et al. (2009), Teolis et al. (2010), and Cui et al. (2012)), it is crucial to ensure that the instrument is still behaving as expected in Saturn's H_2-dominated atmosphere. Thus, data reduction is an especially important procedure for this particular data set since the instrument was performing in a new environment for which it was not designed. Many factors affect the response of the instrument and have been extensively characterized for Titan's atmosphere. Methods for correction are detailed in the analyses listed above. We adopt similar methods from these previous works, as explained below, and recharacterize the corrections to ensure that they are suitable for Saturn conditions. These include background subtraction and dead time correction for detector fatigue, calibration sensitivity, and ram pressure enhancement. Further Saturn-specific characterization and corrections for saturation of the primary detector and for wall adsorption of H_2O and

NH$_3$ are also detailed below. We do not perform corrections for contamination from thruster firings of the spacecraft, which occasionally affect the counts in mass channel 2 during Titan flybys, since thrusters were not used during the C/A measurements we use here.

3.1 Previous data reduction techniques

3.1.1 Background subtraction

Residual gas present in the INMS chamber is responsible for outgassing and enhancing the signal in certain mass channels. Far from Saturn, this background tends to a constant level which must be properly subtracted in order to remove this enhancement. Additionally, the radiation background, which is a mass independent enhancement in signal that is due mainly to the detection of energetic charged particles in the instrument from Saturn's magnetosphere, must also be removed. We determine the radiation background using the signal in mass channels 5 to 8, where no signal is expected and thus the only signal detected here is due to external radiation. To determine the mean background signal for each orbit we average data taken well before closest approach to Saturn where signal in mass channel 2 has not yet begun to increase, which would indicate the detection of Saturn's extended atmosphere, and subtract this background from the overall mass spectrum.

3.1.2 Sensitivity calibration

The INMS flight unit (FU) was calibrated at Goddard Spaceflight Center with neutral species relevant to Titan's atmosphere before launch and additional calibration of other species continued after launch using the identical refurbished engineering unit (REU). Pre-flight calibration included a handful of neutral species relevant to Titan's atmosphere as well as He (a reference species) and Kr, which was used to characterize the FU performance in higher mass channels. Due to response differences between the FU and REU, calibration of the peak sensitivity of each species must be performed in order to utilize REU calibration measurements to understand observations using the FU. The algorithm used to characterize sensitivity calibration is detailed extensively in Cui et al. (2009a) based on measurements of species that were calibrated using both units. We utilize these results here since many of these molecules are also relevant to Saturn's upper atmosphere.

3.1.3 Ram pressure enhancement

The ram pressure of the inflowing sample in CSN mode leads to a density enhancement in the instrument by limiting the conductance of the inflowing sample through the transfer tube to the ionization region (see Figure 2.1) and maintaining the high conductance through the entrance aperture into the antechamber. The ram enhancement factor varies as a function of molecular mass, angle of attack of the instrument, temperature of the ambient gas, and speed of the spacecraft. This factor was previously characterized in Cui et al. (2009a) for Titan flybys, and we use this approach to characterize the ram

enhancement factor for Saturn as well.

3.2   Primary detector saturation

The instrument's dual detector system includes a high gain primary detector which is known to saturate near closest approach in mass channels relevant to the most abundant species in the atmosphere. This leads to signal decay at closest approach as seen in the right panel of Figure 3.1. When this occurs, counts from the secondary detector, albeit with a lower signal-to-noise ratio, can be utilized to obtain an accurate determination of the density profile. In order to take advantage of the primary detector's much higher signal-to-noise ratio, we use a nonlinear conversion technique between the primary and secondary detectors as detailed in Cui et al. (2012). In doing so, we are able to utilize slightly saturated count rates from the primary detector, significantly reducing the amount of noise in the density profile. Saturation of the primary detector is a species dependent process. At Titan, detector saturation occurred in mass channels associated with the atmosphere's major constituents (N_2, $^{14}N^{15}N$, and CH_4) at m/z 14, 15, 16, 28, and 29 amu (Cui et al., 2012). At Saturn, the only channel that experiences saturation is m/z 2 amu, which tracks H_2 in the atmosphere. This saturation can be seen in the left panel of Figure 3.1, where the count rate from the primary detector (C_1) in mass channel 2 is plotted against the count rate from the secondary detector (C_2) in mass channel 2 after dead time correction for detector fatigue (32.6 ns (Waite et al., 2004)). At lower counts the detectors are linearly correlated but as the count rate of the primary detector increases, the signal begins to decay and the

detectors lose their linear correlation. The relationship between the detectors can be described using an empirical equation, as described in Cui et al. (2012):

$$C_2 = a_0 C_1 \exp\{\tan[(a_1 C_1)^{a_2}]\},\tag{3.1}$$

where a_0, a_1, and a_2 are free parameters constrained by the data. The free parameters for each orbit are listed in Table 3.1. Characterizing this relationship allows us to use slightly saturated counts from the primary detector up to 4.2×10^6 counts/s. At this point, the empirical relationship no longer traces the primary detector's signal decay and the correction is no longer applicable, prompting the use of counts from the secondary counter. However, an instantaneous switch from the primary to secondary detector at 4.2×10^6 counts/s could introduce discontinuities in the derived density profiles, which in turn would affect the retrieved temperature profile. To remove this effect, we introduce continuously varying weighting functions, W_1 and W_2, constructed from hyperbolic tangents for each detector to calculate densities in the transition region as first detailed in Cui et al. (2012):

$$W_1^{(2)}(t) = 1 - \frac{1}{2}\tanh\left[\frac{t - t_i^{(2)}}{\Delta t}\right] + \frac{1}{2}\tanh\left[\frac{t - t_o^{(2)}}{\Delta t}\right]\tag{3.2}$$

$$W_2^{(2)}(t) = 1 - W_1^{(2)}\tag{3.3}$$

where t is time from C/A, $t_i^{(2)}$ and $t_o^{(2)}$ correspond to the time when the primary detector reaches 4.2×10^6 counts/s during the inbound and outbound portions of each orbit, and Δt is the timescale for the transition which is approximately 10 seconds. Since atmospheric entry (orbit 293) does not have
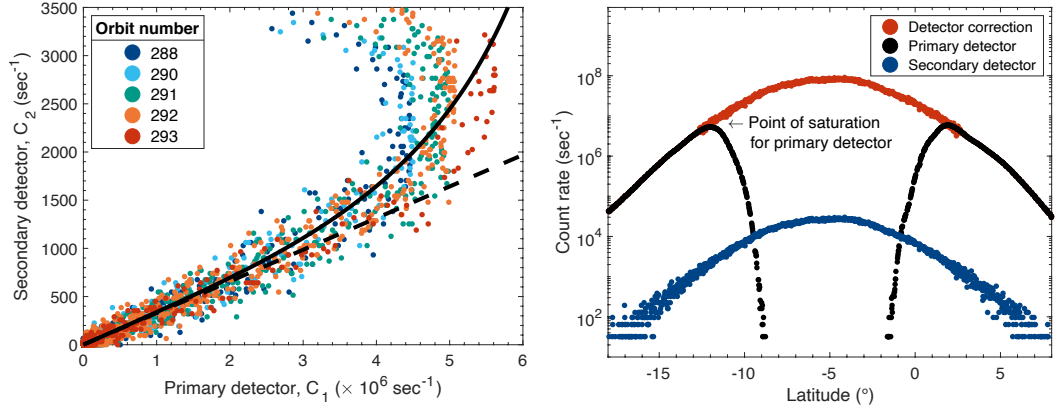
Figure 3.1: Left: Count rate in mass channel 2 (H_2) from the secondary detector (C_2) as a function of count rate in mass channel 2 from the primary detector (C_1) for all five orbits analyzed here. The dashed line represents the linear correlation between these detectors at lower count rates and is the trend that the signal would follow if the primary detector was not affected by saturation. The solid line represents the nonlinear empirical relationship (Equation 6) used to correct for saturation in the primary detector. Doing so increases the signal-to-noise ratio in our results and allows us to use measurements from the primary detector up to 4.2×10^6 counts/s. Right: Count rate of both detectors in mass channel 2 as a function of latitude for orbit 290. Closest approach to Saturn, where the signal is highest, occurs near -5° latitude. As the spacecraft approaches Saturn, the primary detector (black) saturates which leads to a signal decay, while the lower signal secondary detector (blue) does not. We are able to combine measurements from both detectors and determine a corrected count rate to be used to determine a proper H_2 density in Saturn's atmosphere (red).

outbound measurements, we modify Equation 3.2 to handle only the inbound measurements:

$$W_1^{(2)}(t) = 0.5 - \frac{1}{2} \tanh\left[\frac{t - t_i^{(2)}}{\Delta t}\right] \tag{3.4}$$

Utilizing these continuously varying weighting functions allow for a smooth transition between the detectors and a retrieved density profile that is continuous and is sufficient for temperature retrievals of the region.

Table 3.1: Free parameters used in the empirical relationship between the count rates from the primary and secondary detectors for mass channel 2 (H_2.)

Orbit Number	a_0	a_1	a_2
288	3.291×10^{-4}	1.689×10^{-7}	2.556
290	3.975×10^{-4}	1.506×10^{-7}	3.223
291	3.718×10^{-4}	1.362×10^{-7}	3.061
292	3.632×10^{-4}	1.351×10^{-7}	3.117
293	3.528×10^{-4}	1.507×10^{-7}	7.020
All	3.378×10^{-4}	1.373×10^{-7}	2.620

3.3   Wall adsorption corrections

As noted in previous studies (see e.g., Magee et al. (2009), Cui et al. (2009a), and Teolis et al. (2010)), some neutral species are more likely to adsorb on the walls of the antechamber during sampling. This adsorption leads to a time delay in the signal of the adsorbed species and falsely reduces the relative abundance during inbound measurements. Desorption from the chamber walls at a later time leads to an artificial abundance enhancement of that species after closest approach. Wall sticking effects are most notable near closest approach, when the number density of molecules entering the instrument is highest. This predominantly affects outbound measurements, as the adsorbed material begins to desorb after closest approach and contribute to the signal or chemically react with other species within the instrument. Various methods have been used in previous studies to attempt to correct for this issue. Magee et al. (2009) determine a "desorption constant" based on the declining signal of outbound measurements and use an empirical model at Titan in an attempt to remove outbound desorption effects from NH_3.

Similarly, Cui et al. (2009a) assume a species-specific adsorption probability and a desorption time constant in their model to reproduce the observed outbound behavior of heavier species in the instrument. Teolis et al. (2010) develop a more detailed model to correct for water adsorption and desorption during the instrument's encounters with the plumes of Enceladus.

Since INMS outbound measurements are known to suffer more significantly from adsorption issues, our analysis here focuses only on inbound measurements. For this reason, our approach to correct for adsorption and desorption effects within the instrument focuses primarily on inbound adsorption corrections, not outbound desorption corrections. Our analysis does not show any strong evidence of sticking in any mass channels aside from the main parent peaks associated with H_2O (*m/z* 18 amu) and NH_3 (*m/z* 17 amu). Our approach to correct for adsorption includes (1) corrections for the signal time delay of H_2O and NH_3 relative to the signal of all other mass channels and (2) corrections for the artificial reduction in signal due to H_2O and NH_3 sticking to the chamber walls. We use the following equations for these corrections and assume for simplicity that all of the signal in mass channel 17 is from NH_3 and all of the signal in mass channel 18 is from H_2O.

$$Total(t) = Detected(t + t_{des}) + Adsorbed(t) - Desorbed(t) \qquad (3.5)$$

$$Adsorbed(t) = P \times Total(t) \times (1 - \frac{\Delta(t)}{S}) \qquad (3.6)$$

$$Desorbed(t) = Adsorbed(t - t_{des}) \qquad (3.7)$$

$$\Delta(t) = a \times V \times \sum_{t-t_{des}}^{t} \left(Total(t) - Detected(t + t_{des}) + Desorbed(t) \right) \quad (3.8)$$

where P is the sticking coefficient for the adsorbing species ($\sim$0.5 for H_2O at 300K (Waite et al. (2009)), $\sim$0.4 for NH_3 (Diebold and Madey (1992)), S is the surface area of the chamber walls (11 cm^2 (Waite et al. (2004))), Δ is the amount of surface area occupied by the adsorbing species, a is the surface area of one molecule of the adsorbing species, and V is the volume of the chamber (3.5 cm^3 (Waite et al. (2004))). t_{des} is the characteristic time constant for an adsorbing molecule to spend on the chamber walls before desorption, leading to the time delay in signal for adsorbing species. We define this value as the time difference in maximum count rate between H_2O and NH_3 compared to H_2. As a consequence of sticking, the signal for H_2O and NH_3 peak on average about 60 seconds after H_2 and all other species.

Results from our correction for NH_3 (*m/z* 17 amu) and H_2O (*m/z* 18 amu) can be seen in Figure 3.2 for orbit 290 compared to H_2, He, and *m/z* 15 amu (a proxy for CH_4), which do not show signs of adsorption. The top figure shows the normalized density for each of these species as a function of time from closest approach for both inbound (before C/A) and outbound (after C/A) measurements. Prior to correction, H_2O and NH_3 peak 62.9 s after signal from all other channels. The right figure shows the inbound density profile of the same species. Adsorption corrections to H_2O and NH_3 improve the density enhancement issue at lower altitudes that were first noted in Serigano et al. (2020) and also improve the shape of the density profile to more closely

follow that of H_2 and CH_4, which is expected for a species with an external source entering the atmosphere. After corrections, the signal in mass channel 17 increases by an average of 2.32 for orbits analyzed here, and mass channel 18 increases by an average of 2.30. These corrections utilize some outbound data in order to determine t_{des}. Since no outbound data exist for orbit 293 (atmospheric entry), we are not able to perform this correction. Consequently, we use the average correction for all other orbits to correct H_2O and NH_3 during orbit 293 and throughout this paper we include both corrected and uncorrected results for orbit 293.

While wall adsorption leads to difficulties in properly interpreting these measurements for some mass channels, this effect is actually valuable in determining what species might be present in the sample. As noted previously, only certain species are affected by wall adsorption and subsequent chemistry within the instrument. Inert species and CH_4 are known not to contribute to wall adsorption (see e.g., Cui, Yelle, and Volk (2008) and Cui et al. (2009a)), whereas other species, notably H_2O and NH_3, exhibit significant effects due to wall adsorption. Using this knowledge, it can be deduced whether certain species are present in the measurements based solely on the inbound/outbound asymmetry of relevant mass channels. An example of this is seen in Figure 3.3. Mass channel 4, which tracks He (an inert species), exhibits a symmetric profile before and after closest approach. On the other hand, mass channel 18 (H_2O) exhibits a significant asymmetric distribution before and after closest approach indicative of wall effects for this species. Mass channel 15 is a combination of signal predominantly from fragments
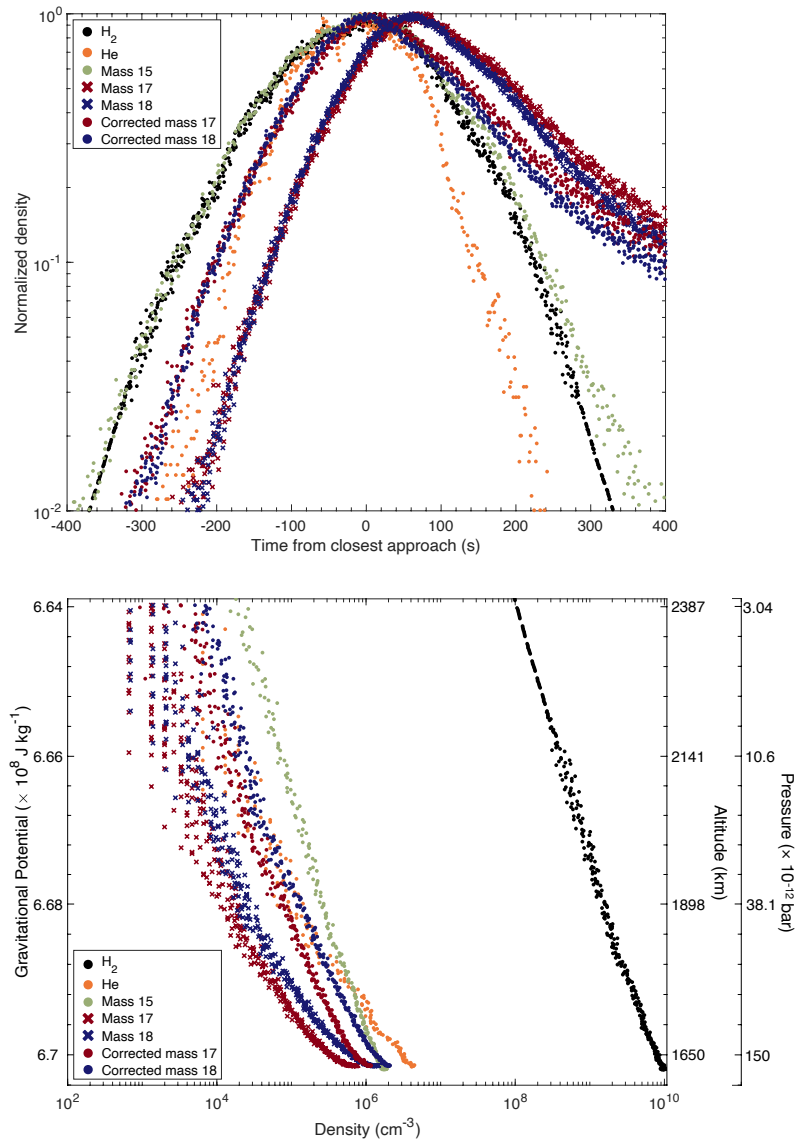
Figure 3.2: Results of inbound adsorption corrections for NH_3 (*m/z* 17 amu) and H_2O (*m/z* 18 amu) compared to other species that do not show signs of adsorption issues within the instrument. *m/z* 15 amu is a proxy for CH_4. Adsorption leads to a time delay in signal for the adsorbing species and an artificial reduction in the relative abundance. Top: Normalized density as a function of time from closest approach to Saturn's ring plane. Compared to H_2, He, and mass channel 15, the uncorrected signal from mass channels 17 and 18 (red and blue x symbols, respectively) peak approximately 60 seconds after the rest of the signal. After adsorption corrections, mass channels 17 and 18 (red and blue circles) follow a similar trend to channels not affected by adsorption. Bottom: Density results before (x symbols) and after (circles) adsorption corrections for NH_3 and H_2O as compared to other species.

46

associated with CH_4 and/or NH_3. The asymmetric distribution implies that the signal measured in this mass channel must have some contribution from NH_3 since the signal from a lack of NH_3 would have had no asymmetry at closest approach.
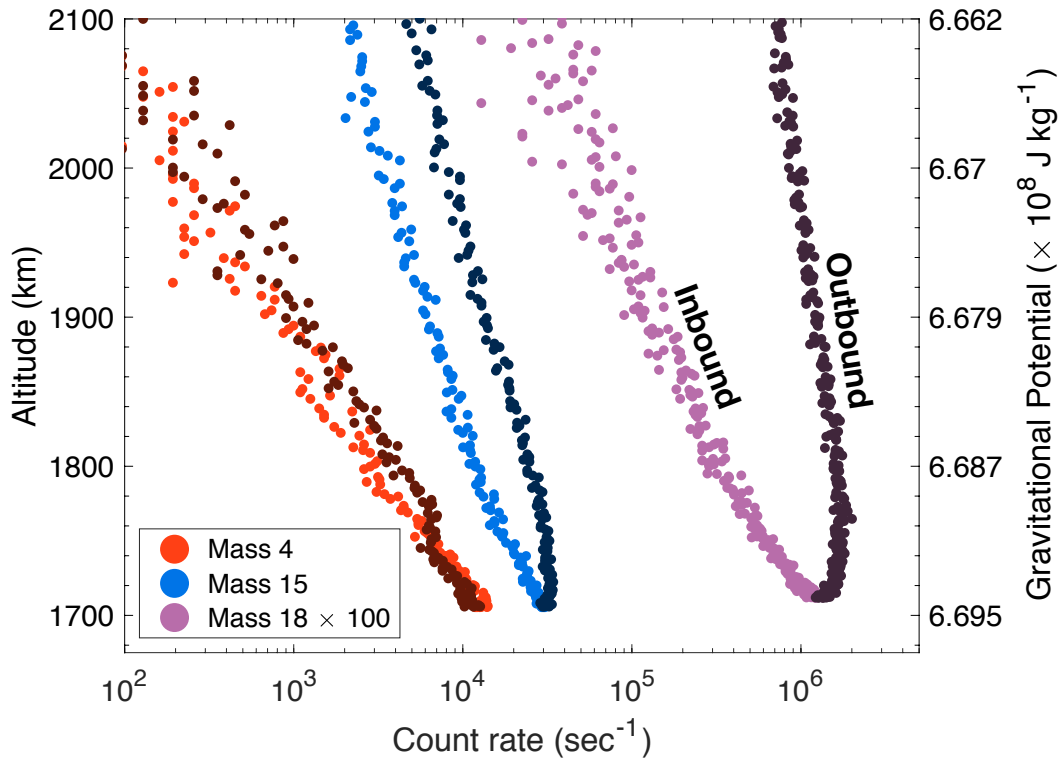
Figure 3.3: Count rate of mass channels 4, 15, and 18 as a function of altitude and gravitational potential from orbit 290. The lighter shade for each mass channel represents the inbound profile and the darker shade represents the outbound profile. The inbound and outbound profiles of mass channel 4 (He) are nearly identical since this species does not adsorb to the instrument's chamber walls or participate in wall chemistry. Mass channel 18 (H_2O) is known to be affected by wall adsorption and chemistry in the instrument, which is the reason for the significant inbound/outbound asymmetry. Mass channel 15 is a combination of signal from CH_4 and NH_3. Since CH_4 is not affected by wall adsorption in the instrument, this asymmetry indicates that NH_3 must be contributing to the signal.

References

Cui, J., R. V. Yelle, and K. Volk (2008). "Distribution and escape of molecular hydrogen in Titan's thermosphere and exosphere". In: *Journal of Geophysical Research: Planets* 113.E10.

Cui, J., R. V. Yelle, V. Vuitton, J. H. Waite, W. T. Kasprzak, D. A. Gell, H. B. Niemann, I. C. F. Müller-Wodarg, N. Borggren, G. G. Fletcher, et al. (2009a). "Analysis of Titan's neutral upper atmosphere from Cassini Ion Neutral Mass Spectrometer measurements". In: *Icarus* 200.2, pp. 581–615.

Cui, J., M. Galand, R. V. Yelle, V. Vuitton, J. E. Wahlund, P. P. Lavvas, I. C. F. Müller-Wodarg, T. E. Cravens, W. T. Kasprzak, and J. H. Waite (2009b). "Diurnal variations of Titan's ionosphere". In: *Journal of Geophysical Research: Space Physics* 114.A6.

Cui, J., R. V. Yelle, D. F. Strobel, I. C. F. Müller-Wodarg, D. S. Snowden, T. T. Koskinen, and M. Galand (2012). "The CH_4 structure in Titan's upper atmosphere revisited". In: *Journal of Geophysical Research: Planets* 117.E11.

Diebold, U and TE Madey (1992). "Adsorption and electron stimulated desorption of NH3/TiO2 (110)". In: *Journal of Vacuum Science & Technology A: Vacuum, Surfaces, and Films* 10.4, pp. 2327–2335.

Magee, B. A., J. H. Waite, K. E. Mandt, J. Westlake, J. Bell, and D. A. Gell (2009). "INMS-derived composition of Titan's upper atmosphere: analysis methods and model comparison". In: *Planetary and Space Science* 57.14-15, pp. 1895–1916.

Müller-Wodarg, I. C. F., R. V. Yelle, J. Cui, and J. H. Waite (2008). "Horizontal structures and dynamics of Titan's thermosphere". In: *Journal of Geophysical Research: Planets* 113.E10.

Serigano, J, SM Hörst, C He, Thomas Gautier, RV Yelle, TT Koskinen, and MG Trainer (2020). "Compositional Measurements of Saturn's Upper Atmosphere and Rings from Cassini INMS". In: *Journal of Geophysical Research: Planets* 125.8, e2020JE006427.

Teolis, B. D., M. E. Perry, B. A. Magee, J. Westlake, and J. H. Waite (2010). "Detection and measurement of ice grains and gas distribution in the Enceladus plume by Cassini's Ion Neutral Mass Spectrometer". In: *Journal of Geophysical Research: Space Physics* 115.A9.

Waite, J. H., W. S. Lewis, B. A. Magee, J. I. Lunine, W. B. McKinnon, C. R. Glein, O. Mousis, D. T. Young, T. Brockwell, J. Westlake, et al. (2009). "Liquid water on Enceladus from observations of ammonia and ^{40}Ar in the plume". In: *Nature* 460.7254, p. 487.

Waite, J. H., W. S. Lewis, W. T. Kasprzak, V. G. Anicich, B. P. Block, T. E. Cravens, G. G. Fletcher, W-H Ip, J. G. Luhmann, R. L. McNutt, et al. (2004). "The Cassini Ion and Neutral Mass Spectrometer (INMS) investigation". In: *The Cassini-Huygens Mission*. Springer, pp. 113–231.

Yelle, R. V., J. Cui, and I. C. F. Müller-Wodarg (2008). "Methane escape from Titan's atmosphere". In: *Journal of Geophysical Research: Planets* 113.E10.

Yelle, R. V., N. Borggren, V. De La Haye, W. T. Kasprzak, H. B. Niemann, I. C. F. Müller-Wodarg, and J. H. Waite (2006). "The vertical structure of Titan's upper atmosphere from Cassini Ion Neutral Mass Spectrometer measurements". In: *Icarus* 182.2, pp. 567–576.

Chapter 4

Mass spectral deconvolution algorithm

The instrument's unit resolution resolving power complicates identification and quantification of species present in the data since the fragmented signal of multiple species overlap and contribute to the signals of the same mass channels. This creates a complex combination of mass peaks associated with a mix of the fragmentation patterns of the species within the sample. Thus, analyzing a complex mixture requires prior knowledge of how each species fragments after ionization within the instrument. These calibration fragmentation patterns can then be used to determine the relative contribution of species to the signal, and ultimately determine the mixing ratios and densities of each species in the sampled region of the atmosphere. Determining the best fitting composition to the data requires solving a system of linear equations:

$$I_i = \sum_{j1}^{n} F_{i,j} N_j \tag{4.1}$$

where I_i is the measured intensity in mass channel i, $F_{i,j}$ is the fragmentation intensity for species j in mass channel i, and N_j is the concentration of species j. Our approach uses a least-squares fitting on multiple linear regressions and we find the least squares minimum of the Euclidian norm of Equation 4.1 using

$$\min_{N} \frac{1}{2} \|F \times N - MS\|_2^2 \tag{4.2}$$

with the condition

$$L \leq N \leq U \tag{4.3}$$

where F is the matrix containing the fragmentation database of species, as detailed in Section 4.1, N is the output vector containing the relative concentration of species, MS is the measured mass spectrum from INMS, and L and U are the vectors containing the lower and upper limits of each species, if applicable. We minimize Equation 4.2 using an interior-point method that is suitable for large matrices such as the mass spectra we analyze here.

The relative fragment intensities of a species vary from instrument to instrument, so it is crucial to have a robust calibration database specific to the instrument for mass spectral deconvolution. Unfortunately, this is not always attainable because it is not always known what constituents will be present in an atmosphere before spacecraft arrival and because some gases can be very harmful or difficult to work with in a lab setting. INMS was calibrated for only a handful of species relevant to Titan's atmosphere, so we must use fragmentation patterns from a similar instrument as a stand-in when data is unavailable. As an alternative, we use calibration data from the National Institute of Standard and Technology (NIST) mass spectral library when INMS

calibration data does not exist. NIST fragmentation patterns are an acceptable proxy since the ionization energy of the NIST library and INMS are the same (70 eV), however fragmentation patterns are highly instrument dependent so the NIST library is not a perfect substitute. Figures 5.2a and b compare the INMS calibration data of CH_4 and H_2O to data from NIST. An example of the signal measured by INMS in this region is shown in Figure 5.2d for orbit 290 and a comparison of the calibration data of overlapping fragmentation patterns for CH_4, H_2O, and NH_3, three volatile ices whose fragmentation patterns overlap significantly, are shown in Figure 5.2c. Although NIST calibrations provide an adequate estimate as to what to expect during the flight instrument's performance, there are significant deviations in fragmentation peak intensity in certain mass channels for both species, notably in minor peaks that are lower in intensity. Furthermore, the instrument's calibration on Earth was performed in an environment very different from that of Saturn, which could lead to discrepancies between the existing calibration data and the returned measurements during the Grand Finale orbits. Deviations stemming from the aging of the instrument, which was launched in 1997, could also affect the instrument's performance over time and lead to further discrepancies between calibration values and returned measurements. Although a calibration database is of utmost importance, an accurate and complete database of fragmentation patterns relevant to this study does not exist.

In order to overcome the challenges brought about by the calibration data
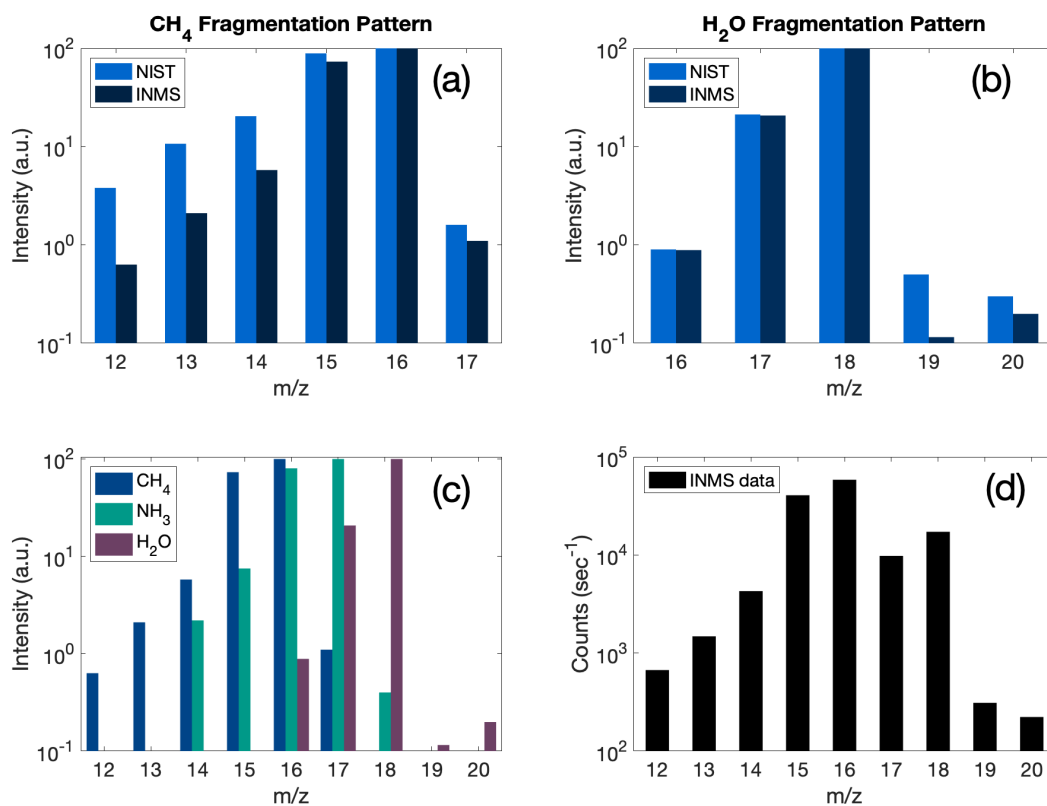
Figure 4.1: (a and b) Comparison of INMS and NIST calibration data for CH_4 (a) and H_2O (b). The differences in fragmentation peak intensities, along with a lack of INMS calibration data for some species, complicate analysis of the spectra returned by INMS. (c) Overlapping fragmentation patterns of CH_4, H_2O, and NH_3 which all contribute to the INMS signal in the region m/z = 12 - 20 amu. CH_4 and H_2O data are from INMS calibration measurements. NH_3 data are from the NIST spectral library. (d) Signal from INMS from orbit 290 extracted between ϕ of 6.69 and 6.66 $\times$ 10^8 J kg^{-1} (1700 to 2050 km).

from INMS, our mass spectral deconvolution algorithm employs a Monte-Carlo based approach to handle the uncertainty in fragmentation peak intensities of each species. This approach is detailed in Gautier et al., 2020 with minor modifications (detailed below) to the overall approach in order to handle the mass range and much larger database of species in our analysis. The Monte-Carlo randomization is applied only to the intensity (y-axis) of each fragmentation peak for each species in the database, not to the *m/z* ratio (x-axis) of the fragmentation peaks. The initial calibration database (see Section 4.1) is a combination of INMS calibration data when available and NIST calibration data. We allow fragmentation peak intensities for all species to vary by $\pm30\%$, although the best-fitting simulations we save for analysis typically vary less than 15%. When deconvolving the spectra, we save 500,000 simulations that meet a residual fitting threshold and analyze the top 10% (50,000) of these simulations. This allows us in the end to retrieve a statistical solution to our issue, providing the most probable concentration for a given species as well as a probability density function (PDF) in order to quantify the variation in a species' concentration throughout the best-fitting simulations saved for analysis. The output of the deconvolution includes the relative abundances of each species in the database based on the randomized fragmentation pattern database that was input into the model. A flowchart of this process is outlined in Figure 4.2.

INMS returned spectra from Saturn with a very large range of signal spanning seven orders of magnitude. This complicates residual best fits since mass channels with higher signal dominate the resulting residual. To handle

this, we separate the spectra into three different sections and fit each section individually. These sections include (1) the high mass, low signal region (m/z 31 to 36 amu, 46 to 100 amu), (2) the low mass, high signal region (m/z 3 to 30 amu, 37 to 45 amu), and (3) H_2, which has a much higher signal than any other mass channels. The m/z 37 to 45 amu section is included with the lower mass, higher signal region because some of the more prominent species (e.g., CO_2, C_3H_6, C_3H_8) contribute to this region, making the signal here significantly higher than the surrounding mass channels. Since some high mass species have base peaks that are much lower in mass than their molecular ion we do not divide the database based solely on location of a species' base peak. If a minor species has a base peak that is overwhelmed by signal from more abundant species then we use other prominent peaks of considerable intensity in order to fit these species. For example, the base peak of ethyl cyanide (C_2H_5CN) is m/z 28 amu which is fit mostly by CO and N_2. For this reason, we fit ethyl cyanide using the second most prominent peak, m/z 54 amu, which is ∼70% of the intensity of the base peak, and consider ethyl cyanide part of the high mass region. The fragmentation database is therefore also split up accordingly, with most species added to the appropriate database based on the location of the base peak and some species added to the database that corresponds to a prominent secondary peak, as listed in Table 4.1.

We first deconvolve the high mass region with the relevant database. Although these species have fragmentation peaks at lower masses that contribute to signal outside of this region, we do not include these peaks in the Monte-Carlo fitting routine. Instead, after deconvolving the spectra and acquiring

the 50,000 best fitting simulations for this region, we use the resulting average fragmentation peak intensity of each species' base peak (or most prominent peak in the region) and the ratio of that peak's intensity to the intensity of peaks outside of the fitting region to determine the contribution of these species to the lower mass channels. Since the lower mass peaks are mostly minor for the species, and since the INMS signal at the higher masses is much lower than the signal at lower masses, these species do not contribute much signal in the lower mass channels. For example, when analyzing the lower mass channels with the highest signal, the higher mass species constitute on average 1.5% of the signal in mass channel 15, 0.1% in channel 16, and 3.6% of the signal in mass channel 28. In total, the high mass species account for 8.4% of the total signal of the lower mass region.

After determining the contribution of the high mass species to the low mass signal we subtract this contribution and deconvolve the remaining low mass signal using the appropriate portion of the database, again saving the 50,000 best-fitting simulations for analysis. Results for the high mass fit, low mass fit, and H_2 are combined before analysis. We perform this analysis on the data in two different forms: (1) an averaged mass spectrum for each orbit that allows us to directly compare the results from all orbits, and (2) binned mass spectra for each orbit that allow us to retrieve mixing ratio and density profiles. The averaged mass spectra consist of data from the region of Saturn's atmosphere where reliable data exists for all orbits, which includes measurements taken between ϕ of 6.69 and 6.66 $\times$ 10^8 J kg^{-1} ($\sim$1700 to 2050 km). The binned mass spectra are divided into regions with a width of ϕ =
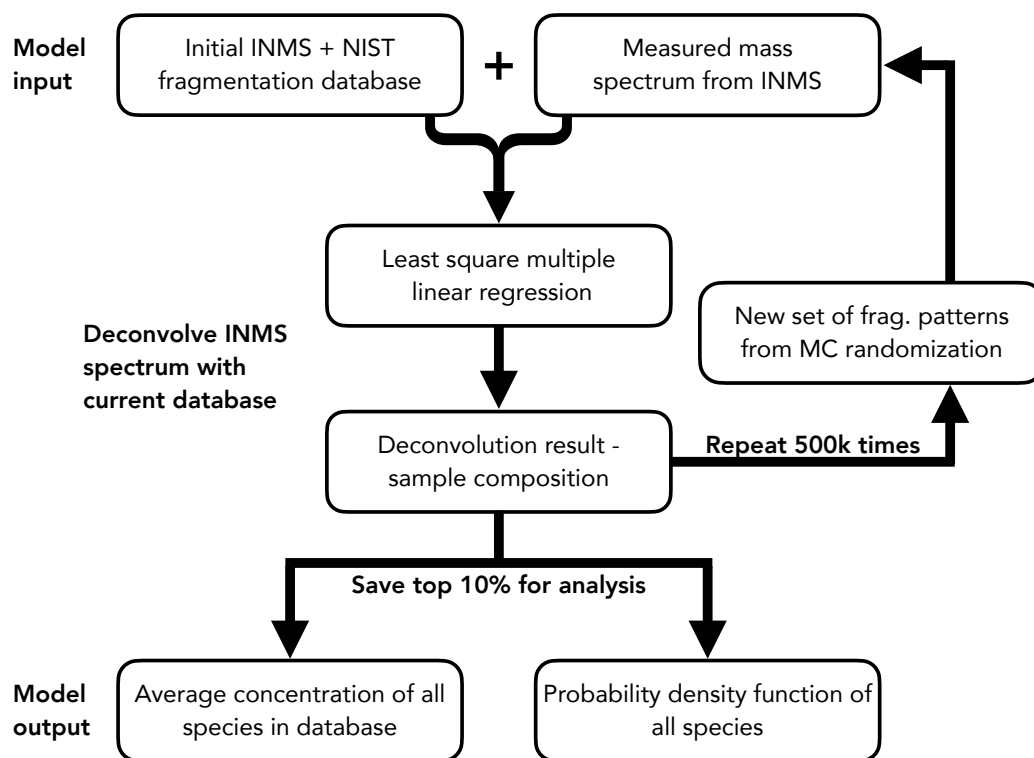
Figure 4.2: Outline of the steps of the Monte-Carlo method used to deconvolve the INMS mass spectra, adapted from Gautier et al. (2020). This process is done three separate times for each mass spectrum in order to deconvole the separate regions before combining results for analysis. These regions are (1) the high mass, low signal region (m/z 31 to 36 amu, 46 to 100 amu), (2) the low mass, high signal region (m/z 3 to 30 amu, 37 to 45 amu), and (3) H_2.

0.01×10^8 J kg^{-1} and the deconvolution is performed separately on each bin.

4.1 Database

The fragmentation pattern database used in this analysis includes 80 species, which can be found in Table 4.1. Our decision to include species in the database is determined by the current understanding of the volatile composition of diffuse environments in the outer solar system as well as the signal returned

from INMS. Diffuse environments include comets (see e.g., Goesmann et al. (2015) and Altwegg et al. (2017)), Pluto (Grundy et al. (2016)), and icy moons including Enceladus (Waite et al. (2009)), Triton (Cruikshank et al. (1993)), and the upper atmosphere of Titan (see e.g, Cui et al. (2009a) and Hörst (2017)). These environments provide evidence of organic compounds in comets and at Enceladus, as well as many complex hydrocarbons and nitriles seen in Titan's N_2/CH_4-rich atmosphere. The most prominent species in our database include the native components of Saturn, H_2, HD, and He, and the most abundant ices of the outer solar system, H_2O, NH_3, CH_4, CO, N_2, and CO_2, all of which have fragmentation patterns that are compatible with the returned INMS signal. UV irradiation and other dissociative processes of these ices provide plausible formation pathways to a variety of hydrocarbons and nitrogen- or oxygen-bearing species that we also include in the database. Isomers of higher mass species are included if the isomer is relatively stable. H_2 and HD are the only isotopologues that we separate and treat as individual species in our analysis since INMS was calibrated for these separately. Since these measurements are taken above the homopause, HD will have less of a vertical extent in the atmosphere as compared to H_2 and separating these species allows us to retrieve a more accurate density profile of HD in this region.

Although the INMS mass range extends to *m/z* 99 amu, our database and modeling efforts focus mainly on lower masses with much higher signal. We include only five species in our database with base peaks above 70 amu since most of the signal above 70 amu is significantly lower than the rest of the

58

spectrum. Adding additional heavier species complicates the deconvolution and significantly increases computational time without significant improvement to the overall fit. Furthermore, it is possible that some of the signal in the instrument's mass range comes from fragmented pieces of molecules with masses exceeding the instrument's mass range. We do not include species with signal above the mass range of the instrument, however, as it is likely that any contribution of larger species is not very significant. In fact, other Cassini instruments with mass ranges higher than INMS reported a much smaller influx of material in this region, suggesting that the ring material entering Saturn's atmosphere may be predominantly smaller molecules like those measured by INMS. The Magnetospheric Imaging Instrument (MIMI), which measures particles in the mass range 8,000 to 40,000 amu, reported a mass deposition rate of about 5.5 kg/s while the Cosmic Dust Analyzer (CDA), which measures even larger nanograins, reported a mass deposition rate on the order of 10^2 to 10^3 kg/s. Both of these instruments measured ring material inflow at much lower rates than INMS ($>10^4$ kg/s, discussed in Chapter 7). We include toluene (C_7H_8) and o-xylene (C_8H_{10}) as our highest mass species, both with base peaks at *m/z* 91 amu and use this base peak as the end of our mass range. Due to a lack of species in our database with higher mass fragments, mass channels above $\sim$70 amu display a larger amount of underfit peaks. As a consequence, our modeling efforts may return larger abundances for these higher mass species since we do not include many other species that might contribute to the signal in this region.

Table 4.1: Species included in our database.

Species name	Species formula	Base peak (amu)	σ (Å^2)	Cal. source
Hydrogen	H_2	2	1.02	INMS
Hydrogen deuteride	HD	3	1.02	INMS
Helium	He	4	0.33	NIST
Ammonia	NH_3	17	3.04	NIST
Methane	CH_4	16	3.52	INMS
Water	H_2O	18	2.28	INMS
Acetylene	C_2H_2	26	4.37	INMS
Hydrogen cyanide	HCN	27	3.44	INMS
Nitrogen	N_2	28	2.51	INMS
Carbon monoxide	CO	28	2.52	INMS
Ethylene	C_2H_4	28	5.12	INMS
Ethane	C_2H_6	28	6.42	INMS
Formaldehyde	H_2CO	29	4.14	NIST
Acetaldehyde	C_2H_4O	29	6.96	NIST
Propane	C_3H_8	29	8.62	INMS
Methylamine	CH_5N	30	6.36	NIST
Ethylamine	C_2H_7N	30	9.25	NIST
Argon	Ar	40	2.77	INMS
Allene	CH_2CCH_2	40	8.08	INMS
Propyne	CH_3CCH	40	7.66	INMS
Ethylenimine	C_2H_5N	40	7.79	NIST
Acetonitrile	CH_3CN	41	6.33	INMS
Propene	C_3H_6	41	8.74	NIST
Ketene	C_2H_2O	42	5.50	NIST
Acetone	C_3H_6O	43	9.85	NIST
Butane	C_4H_10	43	11.7	NIST
Isobutane	C_4H_10	43	13.1	NIST
Pentane	C_5H_12	43	16.0	NIST
Isohexane	C_6H14	43	18.9	NIST
Carbon dioxide	CO_2	44	3.52	INMS
Dimethylamine	C_2H_7N	44	9.25	NIST
Dimethyl Ether	C_2H_6O	45	8.42	NIST
Formamide	CH_3NO	45	6.00	NIST
				Continued on next page

60

Table 4.1 – continued from previous page

Species name	Species formula	Base peak (amu)	σ (Å^2)	Cal. source
Isopropyl alcohol	C_3H_8O	45	11.3	NIST
Ethyl cyanide	C_2H_5CN	28 (54)	9.22	INMS
Formic Acid	CH_2O_2	29 (46)	5.17	NIST
Ethyl isocyanide	C_3H_5N	29 (55)	9.22	NIST
Glyoxal	$C_2H_2O_2$	29 (58)	6.60	NIST
Ethanol	C_2H_6O	31	8.42	NIST
Hydroxy-acetaldehyde	$C_2H_4O_2$	31	8.06	NIST
Methyl Formate	$C_2H_4O_2$	31	8.06	NIST
1-propanol	C_3H_8O	31	11.3	NIST
1,2-ethanediol	$C_2H_6O_2$	31	9.52	NIST
Oxygen	O_2	32	2.44	NIST
Hydrogen sulfide	H_2S	34	4.15	NIST
Phosphine	PH_3	34	4.18	NIST
1,3-Butadiene	C_4H_6	39 (54)	10.9	INMS
1-butene	C_4H_8	41 (56)	11.7	NIST
Acetic Acid	$C_2H_4O_2$	43 (60)	8.06	NIST
2-methyl-butane	C_5H_12	43 (57)	16.0	NIST
Hydroxylamine, O-methyl-	CH_5NO	47	7.46	NIST
Diacetylene	C_4H_2	50	8.90	INMS
Propiolonitrile	C_2HCN	51	6.56	INMS
Cyanogen	C_2N_2	52	5.79	INMS
1-buten-3-yne	C_4H_4	52	8.72	NIST
Acrylonitrile	C_2H_3CN	53	7.76	INMS
2-propynal	C_3H_2O	53	6.93	NIST
2-propenenitrile	C_3H_3N	53	7.76	NIST
3-methyl-1-butene	C_5H_10	55	14.5	NIST
2,3-Dimethyl-2-pentene	C_7H14	55	20.3	NIST
Propargyl alcohol	C_3H_4O	55	8.39	NIST
1-hexene	C_6H_12	56	17.4	NIST
2-propenal	C_3H_4O	56	8.39	NIST
2,2-dimethyl propane	C_5H_12	57	16.0	NIST
Propanal	C_3H_6O	58	9.85	NIST
Methylamine, N,N-dimethyl-	C_3H_9N	58	12.1	NIST
1,3-cyclopentadiene	C_5H_6	66	11.6	NIST
			Continued on next page	

Table 4.1 – continued from previous page

Species name	Species formula	Base peak (amu)	σ (Å^2)	Cal. source
trans-1,3-pentadiene	C_5H_8	67	13.1	NIST
Pyrrole	C_4H_5N	67	10.7	NIST
Furan	C_4H_4O	68	9.82	NIST
Pyridine	C_5H_5N	79	12.1	NIST
Acetaldoxime	C_2H_5NO	59	8.89	NIST
Formamide, N-methyl-	C_2H_5NO	59	8.89	NIST
Acetamide	C_2H_5NO	59	8.89	NIST
Methanamine, N-methoxy-	C_2H_7NO	61	10.4	NIST
Methyl Alcohol	CH_4O	31	5.53	NIST
Benzene	C_6H_6	78	11.7	NIST
E,E-1,3,5-heptatriene	C_7H_10	79	17.4	NIST
o-xylene	C_8H_10	91	20.4	NIST
Toluene	C_7H_8	91	16.0	INMS

Note. σ = ionization cross-section. Mass spectra are fit in 3 separate sections: (1) the high mass, low signal region (m/z 31 to 36 amu, 46 to 100 amu), (2) the low mass, high signal region (m/z 3 to 30 amu, 37 to 45 amu), and (3) H_2. Species in this table are separated according to region. Species with multiple base peaks listed are fit using a predominant peak (in parenthesis) that is not the base peak in order to include these species in the high mass, low signal region (see text for further description).

References

Altwegg, Kathrin, Hans Balsiger, Jean-Jacques Berthelier, André Bieler, Ursina Calmonte, Stephen A Fuselier, Fred Goesmann, Sébastien Gasc, Tamas I Gombosi, Léna Le Roy, et al. (2017). "Organics in comet 67P–a first comparative analysis of mass spectra from ROSINA–DFMS, COSAC and Ptolemy". In: *Monthly Notices of the Royal Astronomical Society* 469.Suppl_2, S130–S141.

Cruikshank, Dale P, Ted L Roush, Tobias C Owen, Thomas R Geballe, Catherine De Bergh, Bernard Schmitt, Robert H Brown, and Mary Jane Bartholomew (1993). "Ices on the surface of Triton". In: *Science* 261.5122, pp. 742–745.

Cui, J., R. V. Yelle, V. Vuitton, J. H. Waite, W. T. Kasprzak, D. A. Gell, H. B. Niemann, I. C. F. Müller-Wodarg, N. Borggren, G. G. Fletcher, et al. (2009a). "Analysis of Titan's neutral upper atmosphere from Cassini Ion Neutral Mass Spectrometer measurements". In: *Icarus* 200.2, pp. 581–615.

Gautier, T., J. Serigano, J. Bourgalais, S. M. Hörst, and M. G. Trainer (2020). "Decomposition of electron ionization mass apectra for space application using a Monte-Carlo approach". In: *Rapid Communications in Mass Spectrometry* 34.8, e8684.

Goesmann, F., H. Rosenbauer, J. H. Bredehöft, M. Cabane, P. Ehrenfreund, T. Gautier, C. Giri, H. Krüger, L. Le Roy, A. J. MacDermott, et al. (2015). "Organic compounds on comet 67P/Churyumov-Gerasimenko revealed by COSAC mass spectrometry". In: *Science* 349.6247, aab0689.

Grundy, WM, RP Binzel, BJ Buratti, JC Cook, DP Cruikshank, CM Dalle Ore, AM Earle, K Ennico, CJA Howett, AW Lunsford, et al. (2016). "Surface compositions across Pluto and Charon". In: *Science* 351.6279.

Hörst, Sarah M (2017). "Titan's atmosphere and climate". In: *Journal of Geophysical Research: Planets* 122.3, pp. 432–482.

Waite, J. H., W. S. Lewis, B. A. Magee, J. I. Lunine, W. B. McKinnon, C. R. Glein, O. Mousis, D. T. Young, T. Brockwell, J. Westlake, et al. (2009). "Liquid

water on Enceladus from observations of ammonia and ^{40}Ar in the plume".
In: *Nature* 460.7254, p. 487.

Chapter 5

Mass spectral deconvolution results

Fitting a unit resolution mass spectrum whose signal is a combination of many different species is a degenerate process with many plausible solutions. Thus, we report here our best understanding and interpretation of the signal returned by the instrument based on our best fitting models and present a set of species for which the combination of relative intensities and fragmentation patterns are consistent with the measured mass spectra. An example of the resulting best fit for averaged data from orbit 290 is shown in Figure 5.1. The fits for all orbits follow a similar trend and can be found in Figure 5.3 of Section 5.4. The blue mass spectrum represents the average of the top 10% best-fitting simulations, the black outline bars represent the measured INMS spectrum, and the inset figure represents the residual to each mass channel fit. Residuals for mass channels 1 to 4, which are not shown in this figure, are always below 1%. Residuals for any mass channel with less than 20 counts are not shown as these mass channels do not contribute significantly to the overall fit of the spectrum.
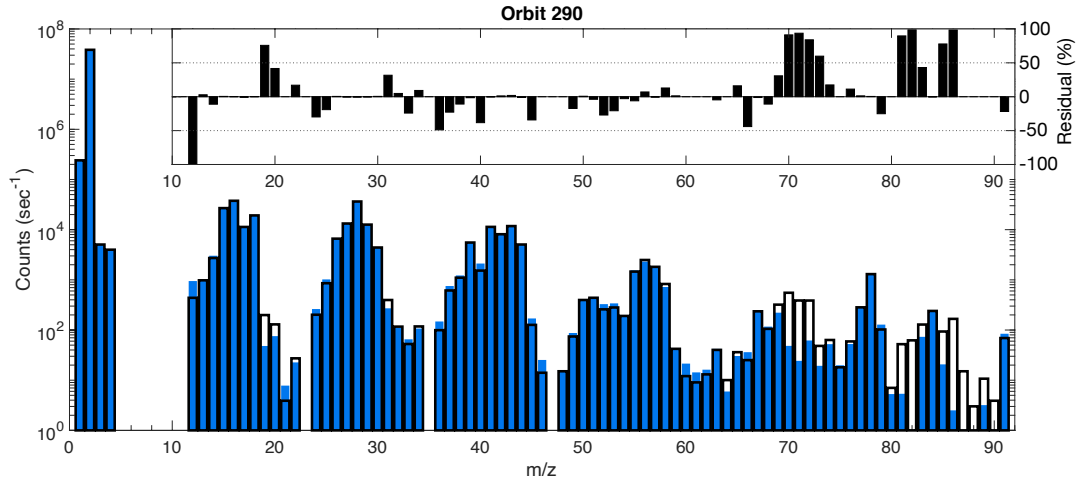
Figure 5.1: Mass spectral deconvolution result for the averaged mass spectrum returned from orbit 290. Black outline bars represent the measured INMS spectrum and blue bars represent the average of the top 10% (50,000) best-fitting simulations. The inset figure in the top right represents the residual to each mass channel. Residuals for mass channels 1 to 4 are not shown and are always below 1%. Residuals for any mass channel with less than 20 counts are not shown. Fits for other orbits analyzed here can be found in Section 5.4.

Our simulated mass spectra for all mass channels with counts above 10^3, which make up on average 94.5% of the non-H_2 signal, are fit to within 1.95% and mass channels with counts above 10^4 (70.1% of the non-H_2 signal) are fit to within 0.38% percent. These values exclude H_2, which dominates the signal, and is always fit to within 0.001%. Although isotopic values can be deduced from our best fitting models, we do not report any isotopic measurements in this analysis since these measurements were taken in Saturn's diffuse uppermost atmosphere which makes it difficult to discern any meaningful isotopic information. Probability density functions, which allow us to quantify the variation in a species' concentration throughout the best-fitting simulations, are also included in Figures 5.4 to 5.8 in Section 5.4 for all averaged orbits.

We allow fragment intensities to vary by ±30%, however most fragments

only vary by a few percent. Figure 5.2 shows an example of the typical variation of fragmentation peak intensities for CH_4, H_2O, and NH_3 for orbit 290, which are three of the most abundant species detected in the spectra and have overlapping fragmentation patterns. Intensities (in arbitrary units) are normalized to the base peak. In most instances the higher intensity fragments, which contribute more to the overall signal and residual, vary more than their lower intensity counterparts. For example, the two highest intensity peaks for CH_4, *m/z* 15 and 16 amu, vary on average 15% and 11%, respectively, for all orbits, whereas *m/z* 13 and 14 amu vary by 1.7% and 1.4%, respectively.

Variations in the peak intensities due to our Monte-Carlo fitting routine are moderate but do have a noticeable impact on the resulting abundances. In order to assess our modeling efforts, we perform an additional simulation for each mass spectra using the original database without varying the fragmentation patterns of species within the database. The lack of variations leads to a poorer fit overall, with non-H_2 counts above 10^3 fit to within 8.57% and counts above 10^4 fit to within 1.83%. The mixing ratios of species, which are discussed in the following Chapter, are also affected. For example, the mixing ratio of CH_4 increases on average by 25.6% when using the original database, while H_2O increases by 25.4% and NH_3 increases by 16.1%. Mixing ratio results for all species from our modeling efforts can be found in Table 6.2 in Chapter 6. A comparison of the results using the original database with no Monte-Carlo variations for orbit 290 can be found in Table 5.1 in Section 5.4.

Despite separate data reduction and mass spectral deconvolution techniques, the results presented in this analysis arrive at similar conclusions to
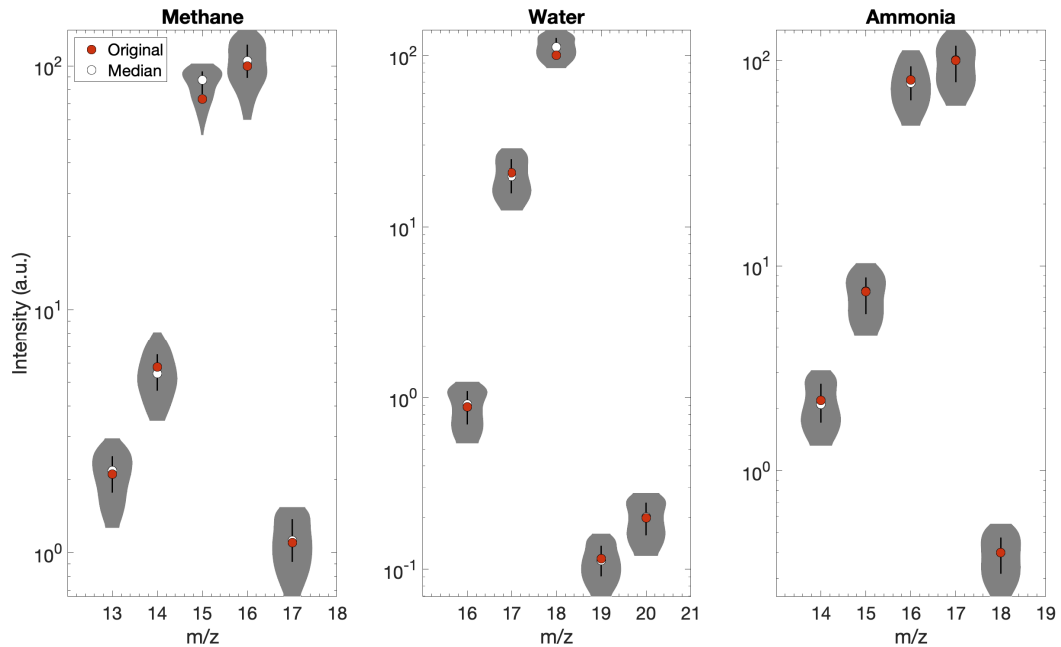
Figure 5.2: Example of fragmentation peak intensity variations for CH_4, H_2O, and NH_3 for orbit 290. The shaded grey region represents the probability density of all 50,000 best-fitting simulations and the black bars represent one standard deviation of the results.

previous reports exploiting the same data set (Waite et al. (2018) and Miller et al. (2020)). All analyses conclude that the major components of the signal include the low mass native Saturn species (H_2 and He) as well as notable volatile ices in the outer solar system: H_2O, NH_3, CH_4, CO, N_2, and CO_2. Differences in compositional results arise mostly in lower signal regions that are attributed to more minor species in our database, which is unsurprising given the major differences in techniques involved with each analysis. While Miller et al. (2020) provide a compositional analysis comprising all species in the NIST mass spectral library with a mass under 100 amu (1996 species in total), the database in this study includes only 80 species that we deem likely to be present in the spectrum based on our understanding of the sampled

environment. Additionally, instead of prioritizing certain species in our fit, which could influence the final result and subjectively increase the abundance of particular species, we fit all species in each region simultaneously. Importantly, since NIST calibration data is not a perfect substitute when INMS calibration data do not exist, we allow fragmentation peak intensities to vary throughout our deconvolution, as described above. We believe this method of mass spectral deconvolution is a powerful new tool that can increase the scientific retrieval of planetary mass spectrometry data when calibration of the instrument is not sufficient.

5.1 Mass 1-20

The mass range from m/z 1 to 20 amu includes many prominent peaks associated with H_2, HD, He, CH_4, H_2O, and NH_3, as well as contribution from fragments of other higher mass species. There is no signal detected from 5 to 11 amu. The signal below 5 amu is attributed to H_2, HD, and He, and above 11 amu is mostly a combination of CH_4, H_2O, and NH_3 along with a smaller contribution of signal from fragments of higher mass species. Mass channels below 5 are always very well fit by our model and residuals are always below 1%. The signal in mass channels 12 through 14 is attributed to fragments of carbon- and nitrogen-bearing species in the form of C^+, CH^+, and CH_3^+/N^+, respectively. CH_4 accounts for the majority of the signal in mass channels 15 and 16, making up 90% and 83% of the signal in these channels, respectively. The signal in mass channels 17 and 18, the main peaks associated with NH_3

and H_2O, increased twofold after the adsorption corrections described in Section 3.3 and the contributions in these channels are mainly due to fragments of these two species along with CH_4, which contributes to mass channel 17 in the form of $^{13}CH_4$.

While the most prominent peaks are always fit very well in this region, mass channel 12, which is always on the order of 10^2 counts, is a minor peak in our analysis with a resulting fit that does not match well with the measured spectra returned by the instrument. In extending our analysis to include higher mass species and the entirety of the mass range, it is evident that the signal in mass channel 12 is lower than anticipated when compared to peaks in the surrounding area and to the calibration data available. The peak intensity in mass channel 12 is typically much higher in the NIST calibration data than it is for the INMS data when comparing species that are present in both data sets. For example the peak intensities for mass channel 12 for CH_4 and CO_2 are 6.3 and 7.3 times higher, respectively, in the NIST calibration data. Since NIST data must be used for many carbon-bearing species, the tendency of NIST calibration data to be higher than that of INMS in mass channel 12 could be responsible for the discrepancy between the measured spectra and our best-fitting simulations. Given the age of INMS it's possible that the instrument has degraded over time, which could also affect mass channel 12.

The signal in mass channels 19 and 20 are consistently underfit and always slightly elevated near C/A. For mass channel 19 this includes C/A during orbits that sampled the less dense outer F ring and regions higher in altitude

than the deepest orbits discussed here (found in Figure 2.3). Signal in mass channels 19 and 20 could be attributed to certain species, including Ar and H_2O, but even with contributions from these species the signal still remains underfit. Isotopes of H_2O are responsible for the H_2O contributions to these channels (in the form $H_2^{17}O$ in *m/z* 19 amu and $H_2^{18}O$ in *m/z* 20 amu), however the level of isotope enrichment needed to fit these peaks is unlikely. The Ar abundance that would be needed to fit these peaks is also unlikely in this region. It is more likely that mass channel 19 suffers from internal instrument contamination from filament desorption most likely due to fluorine (see e.g, Perry et al. (2010) and Perry et al. (2015)), however this is a poorly constrained source of contamination. The high signal associated with mass channel 20 might also be associated with fluorine contamination. Fluorine is the most electronegative element, meaning it's possible that any fluorine in the antechamber readily reacts with hydrogen to form HF which would contribute to mass channel 20.

5.2 Mass 28

The signal in mass channel 28 is significant and the potential species contributing to this channel could have major implications for the inner ring composition. N_2 and CO both share *m/z* 28 amu as their base peak and stand out as prominent volatile ices with abundant reservoirs on airless bodies throughout the outer solar system. This makes their presence in the rings plausible, however no ring composition studies to date have definitively detected these volatiles in the rings. C_2H_4 and C_2H_6 are additional organics with

71

plausible formation pathways in this region that could also have significant contributions to mass channel 28. The degeneracy involved with deconvolving the signal in mass channel 28 is further complicated by the lack of notable fragmentation peaks for these species in other mass channels. For example, the next most prominent peaks for CO include mass channels 12 and 16, both of which are overwhelmed by signal from other species. Similarly, the next most prominent peak for N_2, mass channel 14, is swamped by signal from fragments of CH_4 and NH_3. Without higher resolution data, which would allow for unique identification, we must rely on our modeling efforts and careful analysis of the deconvolution to determine the best fitting results to these measurements. Our best fits for all orbits have a similar contribution from both N_2 and CO to mass channel 28, with less of a contribution from C_2H_4, C_2H_6, and other organics contributing to the mass channel. On average, CO contributes 37% to the total signal at mass 28, while N_2 contributes 34% percent, C_2H_6 contributes 10%, C_2H_4 contributes 7%, with the remaining 12% attributed to other species.

5.3   Other masses

As previously noted, the complexity of the mass spectra returned by INMS was unexpected and the higher mass organic signal was particularly surprising. Hydrocarbons, nitriles, oxygen-bearing species, and high mass organics all have significant contributions in our modeled spectra, with a handful of species in the database comprising the majority of the remaining signal. The bulk of the signal surrounding mass channel 28 is dominated by HCN, C_2H_2,

and H_2CO. The following region, around $m/z \sim 40$ amu, is dominated by C_3H_6, C_3H_8, C_2H_4O, and CO_2, with additional contributions from fragments of butane and isobutane (isomers of C_4H_{10}). Above this region, the signal is dominated mostly by four species: benzene (C_6H_6), 1-hexene (C_6H_{12}), 2-propenal (C_3H_4O), and 2-methyl-butane (C_5H_{12}), which make up 60.1% of the higher mass contribution on average.

The unexpected complexity of the mass spectra leads one to question the origin of this material. Although they have never been detected in the rings before, the existence of native ices other than H_2O (e.g., CH_4, NH_3, CO, N_2, CO_2) is likely. In fact, INMS measurements from the F ring-grazing orbits and higher altitude orbits between Saturn and the D ring (Figure 2.3) found additional evidence of non-water ices. Spectra from these orbits are much lower in signal, however mass channels that are consistently above the noise level include channels associated with H_2, CH_4, 28 amu (mostly CO/N_2), and CO_2. This signal, along with the density profile of these species at lower altitudes matching that of H_2 (as detailed in Chapter 6), suggest that this ring material is likely the external source for the material falling into Saturn's atmosphere. The difficulty of remotely measuring the diffuse, tenuous rings may have allowed these volatiles to elude detection until now. Additionally, Saturn's D ring is much darker in appearance than the other main rings, indicating that the D ring has a higher concentration of non-water ice material. The higher mass constituents, on the other hand, could be native to the rings and/or could be products of photochemistry in Saturn's thermosphere.

Photodissociation of CH_4 in Titan's thermosphere is largely responsible

for the organically rich atmosphere found there (see e.g., Hörst (2017)). Many laboratory studies using initial gas mixtures of N_2 and CH_4 in an attempt to reproduce Titan's atmosphere and study the subsequent organic chemistry occurring have reported photochemical haze aerosol production analogous to aerosol found in Titan's atmosphere (see e.g., Sciamma-O'Brien et al. (2010), Trainer et al. (2012), Sciamma-O'Brien, Ricketts, and Salama (2014), and Hörst et al. (2018)). Further studies incorporating minor species such as C_6H_6, CO, and other aromatic precursors have demonstrated that including trace amounts of these species has a significant impact on the composition and production rates of aerosol. These trace species can lead to the formation of larger polycyclic aromatic hydrocarbons (PAHs) and polycyclic aromatic nitrogen heterocycles (PANHs) which are thought to play a significant role in Titan's organic haze layers (see e.g., Trainer et al. (2013), Yoon et al. (2014), Hörst and Tolbert (2014), Sebree et al. (2014), and Gautier et al. (2017)).

Similar to Titan, EUV photons, high energy electrons from Saturn's magnetosphere, other energetic particles, and trace species detected in the INMS spectra are available in Saturn's thermosphere, making it possible that photochemistry could be happening in this region of Saturn as well. Indeed, using INMS results from atmospheric entry, Chadney et al. (submitted) found that the addition of an influx of CH_4 into Saturn's thermosphere leads to photodissociated products in the region which could contribute to further chemistry and lead to the formation of higher mass molecules. Furthermore, Koskinen et al. (2016) previously highlighted the idea of CH_4 photochemistry at high altitudes in Saturn to initiate the chemistry that produces benzene and

ultimately PAHs and stratospheric haze in Saturn.

5.4   Supplementary information

Table 5.1: Modeled mixing ratio results for orbit 290 compared to results using the original database (DB) with no peak intensity variations. Species are listed from highest to lowest mixing ratio for orbit 290 modeled results. Mixing ratio results are discussed in detail in the following Chapter. Errors for the original database (not shown) are only from counting statistics from INMS which are typically under 20%.

Species name	Species formula	Modeled result	Original DB result	Relative diff. (%)
Hydrogen	H_2	$0.99 \pm (2.7 \times 10^{-5})$	9.98×10^{-1}	0
Helium	He	$3.5 \pm 1 \times 10^{-4}$	4.0×10^{-4}	13.8
Water	H_2O	$2.4 \pm 0.7 \times 10^{-4}$	2.8×10^{-4}	14.4
Methane	CH_4	$2.2 \pm 0.5 \times 10^{-4}$	3.0×10^{-4}	26.2
Carbon monoxide	CO	$1.5 \pm 0.5 \times 10^{-4}$	1.4×10^{-4}	-4.7
Hydrogen deuteride	HD	$1.4 \pm 0.4 \times 10^{-4}$	1.6×10^{-4}	13.6
Nitrogen	N_2	$1.3 \pm 0.4 \times 10^{-4}$	1.5×10^{-4}	16.8
Ammonia	NH_3	$6.4 \pm 2.4 \times 10^{-5}$	7.5×10^{-5}	14.7
Hydrogen cyanide	HCN	$3.5 \pm 1.7 \times 10^{-5}$	2.7×10^{-5}	-29.2
Formaldehyde	H_2CO	$2.3 \pm 1.2 \times 10^{-5}$	2.0×10^{-5}	-18.4
Carbon dioxide	CO_2	$2 \pm 1.1 \times 10^{-5}$	2.0×10^{-5}	-1.3
Acetylene	C_2H_2	$1.6 \pm 0.8 \times 10^{-5}$	1.5×10^{-5}	-8.2
Ethylene	C_2H_4	$1.5 \pm 1.1 \times 10^{-5}$	2.1×10^{-5}	26.8
Ethane	C_2H_6	$1.5 \pm 1.1 \times 10^{-5}$	3.3×10^{-5}	54.4
Propene	C_3H_6	$7.7 \pm 2.8 \times 10^{-6}$	1.3×10^{-5}	41
Propane	C_3H_8	$6.7 \pm 4.5 \times 10^{-6}$	5.1×10^{-6}	-31.6
Acetaldehyde	C_2H_4O	$6.1 \pm 5.7 \times 10^{-6}$	1.3×10^{-5}	50.9
Pentane	C_5H_{12}	$5.4 \pm 3.5 \times 10^{-6}$	8.2×10^{-7}	-563.9
Isobutane	C_4H_{10}	$4.6 \pm 3.8 \times 10^{-6}$	7.1×10^{-6}	36
Methylamine	CH_5N	$4.2 \pm 3.2 \times 10^{-6}$	1.3×10^{-6}	-234.3
Acetonitrile	CH_3CN	$3.4 \pm 2.5 \times 10^{-6}$	6.8×10^{-6}	49.7
Butane	C_4H_{10}	$3.3 \pm 2 \times 10^{-6}$	5.9×10^{-6}	43.1
Isohexane	C_6H_{14}	$3.2 \pm 2.3 \times 10^{-6}$	3.7×10^{-6}	14.3
Benzene	C_6H_6	$2.8 \pm 0.7 \times 10^{-6}$	3.7×10^{-6}	23.4
2-propenal	C_3H_4O	$2.4 \pm 0.4 \times 10^{-6}$	3.1×10^{-6}	22
2-methyl-butane	C_5H_{12}	$1.7 \pm 0.4 \times 10^{-6}$	4.8×10^{-6}	63.9
1-butene	C_4H_8	$1.7 \pm 0.4 \times 10^{-6}$	2.2×10^{-6}	20.8
Propanal	C_3H_6O	$1.7 \pm 0.5 \times 10^{-6}$	1.4×10^{-6}	-21.5
Ketene	C_2H_2O	$1.5 \pm 1.4 \times 10^{-6}$	1.8×10^{-7}	-730.2
2,2-dimethyl propane	C_5H_{12}	$1.3 \pm 0.2 \times 10^{-6}$	1.0×10^{-6}	-32.1
1-hexene	C_6H_{12}	$1.2 \pm 0.2 \times 10^{-6}$	1.6×10^{-6}	23.6

Continued on next page

Table 5.1 – continued from previous page

Species name	Species formula	Modeled result	Original DB result	Relative diff. (%)
Argon	Ar	$9.8 \pm 9 \times 10^{-7}$	3.4×10^{-7}	-185.4
Glyoxal	$C_2H_2O_2$	$5.8 \pm 2.8 \times 10^{-7}$	8.3×10^{-7}	30.4
Propiolonitrile	C_2HCN	$5.6 \pm 2.9 \times 10^{-7}$	5.6×10^{-7}	-1
Pyrrole	C_4H_5N	$5.4 \pm 1.6 \times 10^{-7}$	6.2×10^{-7}	13.4
Phosphine	PH_3	$4.8 \pm 2.2 \times 10^{-7}$	7.2×10^{-7}	33.9
Propyne	CH_3CCH	$3.6 \pm 5.1 \times 10^{-7}$	6.8×10^{-8}	-428.1
Allene	CH_2CCH_2	$3.5 \pm 4.8 \times 10^{-7}$	5.4×10^{-8}	-546.8
Diacetylene	C_4H_2	$3.4 \pm 1.4 \times 10^{-7}$	3.2×10^{-7}	-6.8
Oxygen	O_2	$2.8 \pm 2.4 \times 10^{-7}$	3.4×10^{-7}	17.4
Furan	C_4H_4O	$2.8 \pm 0.9 \times 10^{-7}$	3.3×10^{-7}	17
Acetone	C_3H_6O	$2.6 \pm 2.3 \times 10^{-7}$	3.8×10^{-7}	31.2
3-methyl-1-butene	C_5H_{10}	$2.3 \pm 1.4 \times 10^{-7}$	9.5×10^{-7}	75.5
Ethylenimine	C_2H_5N	$1.9 \pm 2.6 \times 10^{-7}$	6.1×10^{-8}	-203.9
Hydrogen sulfide	H_2S	$1.8 \pm 1.6 \times 10^{-7}$	1.3×10^{-7}	-36.3
1,3-Butadiene	C_4H_6	$1.7 \pm 0.9 \times 10^{-7}$	2.6×10^{-8}	-567.6
Ethyl cyanide	C_2H_5CN	$1.3 \pm 1.3 \times 10^{-7}$	1.2×10^{-6}	89.3
Ethanol	C_2H_6O	$1.3 \pm 1.1 \times 10^{-7}$	2.2×10^{-7}	42.5
2,3-Dimethyl-2-pentene	C_7H_{14}	$1.1 \pm 0.7 \times 10^{-7}$	2.2×10^{-7}	49
Formic Acid	CH_2O_2	$8.8 \pm 3.7 \times 10^{-8}$	1.3×10^{-7}	30.3
Hydroxy-acetaldehyde	$C_2H_4O_2$	$7.9 \pm 8.8 \times 10^{-8}$	1.2×10^{-7}	33.8
Toluene	C_7H_8	$7.8 \pm 5 \times 10^{-8}$	1.8×10^{-7}	55.7
Propargyl alcohol	C_3H_4O	$7.7 \pm 9.6 \times 10^{-8}$	8.0×10^{-8}	3.7
Methyl Alcohol	CH_4O	$6.8 \pm 7 \times 10^{-8}$	1.1×10^{-7}	38.9
Cyanogen	C_2N_2	$6.5 \pm 8 \times 10^{-8}$	2.1×10^{-7}	69.6
Ethyl isocyanide	C_3H_5N	$6.3 \pm 7.1 \times 10^{-8}$	2.2×10^{-7}	71.8
E,E-1,3,5-heptatriene	C_7H_{10}	$5.2 \pm 4.8 \times 10^{-8}$	3.4×10^{-8}	-53.2
Acetic Acid	$C_2H_4O_2$	$4.9 \pm 2.2 \times 10^{-8}$	9.9×10^{-8}	51
o-xylene	C_8H_{10}	$4.8 \pm 3.4 \times 10^{-8}$	8.6×10^{-8}	44.8
2-propynal	C_3H_2O	$4.2 \pm 6.2 \times 10^{-8}$	1.7×10^{-7}	74.7
1,2-ethanediol	$C_2H_6O_2$	$3.6 \pm 3.6 \times 10^{-8}$	7.3×10^{-8}	50.7
1-buten-3-yne	C_4H_4	$3.6 \pm 4.4 \times 10^{-8}$	8.0×10^{-8}	54.9
Methyl Formate	$C_2H_4O_2$	$3.1 \pm 2.2 \times 10^{-8}$	1.0×10^{-7}	70.2
1,3-cyclopentadiene	C_5H_6	$2.9 \pm 1.3 \times 10^{-8}$	3.5×10^{-8}	16.4
Ethylamine	C_2H_7N	$2.7 \pm 2.1 \times 10^{-8}$	1.2×10^{-8}	-128.4
Formamide	CH_3NO	$2.3 \pm 2 \times 10^{-8}$	1.1×10^{-7}	78.2
Pyridine	C_5H_5N	$2.1 \pm 2.5 \times 10^{-8}$	3.9×10^{-8}	46.1
2-propenenitrile	C_3H_3N	$1.8 \pm 1.6 \times 10^{-8}$	2.8×10^{-7}	93.6
Acrylonitrile	C_2H_3CN	$1.7 \pm 1.6 \times 10^{-8}$	2.9×10^{-7}	94
trans-1,3-pentadiene	C_5H_8	$1.7 \pm 1.7 \times 10^{-8}$	6.4×10^{-8}	73
Dimethylamine	C_2H_7N	$1.6 \pm 1.3 \times 10^{-8}$	2.8×10^{-8}	44.2
Methanamine, N-methoxy-	C_2H_7NO	$1.3 \pm 0.5 \times 10^{-8}$	2.3×10^{-8}	40.8
Dimethyl Ether	C_2H_6O	$1.2 \pm 1.7 \times 10^{-8}$	4.9×10^{-8}	75.3

Table 5.1 – continued from previous page

Species name	Species formula	Modeled result	Original DB result	Relative diff. (%)
Methylamine, N,N-dimethyl-	C_3H_9N	$1 \pm 0.9 \times 10^{-8}$	5.0×10^{-8}	79.1
1-propanol	C_3H_8O	$8.3 \pm 8 \times 10^{-9}$	1.6×10^{-8}	49.7
Isopropyl alcohol	C_3H_8O	$6.6 \pm 7.2 \times 10^{-9}$	7.0×10^{-9}	6
Hydroxylamine, O-methyl-	CH_5NO	$2.9 \pm 1.3 \times 10^{-9}$	4.3×10^{-9}	33.1
Acetamide	C_2H_5NO	$2.4 \pm 1.8 \times 10^{-9}$	6.6×10^{-9}	64.5
Acetaldoxime	C_2H_5NO	$2.3 \pm 1.8 \times 10^{-9}$	7.7×10^{-9}	69.8
Formamide, N-methyl-	C_2H_5NO	$2.3 \pm 1.8 \times 10^{-9}$	5.3×10^{-9}	56.2
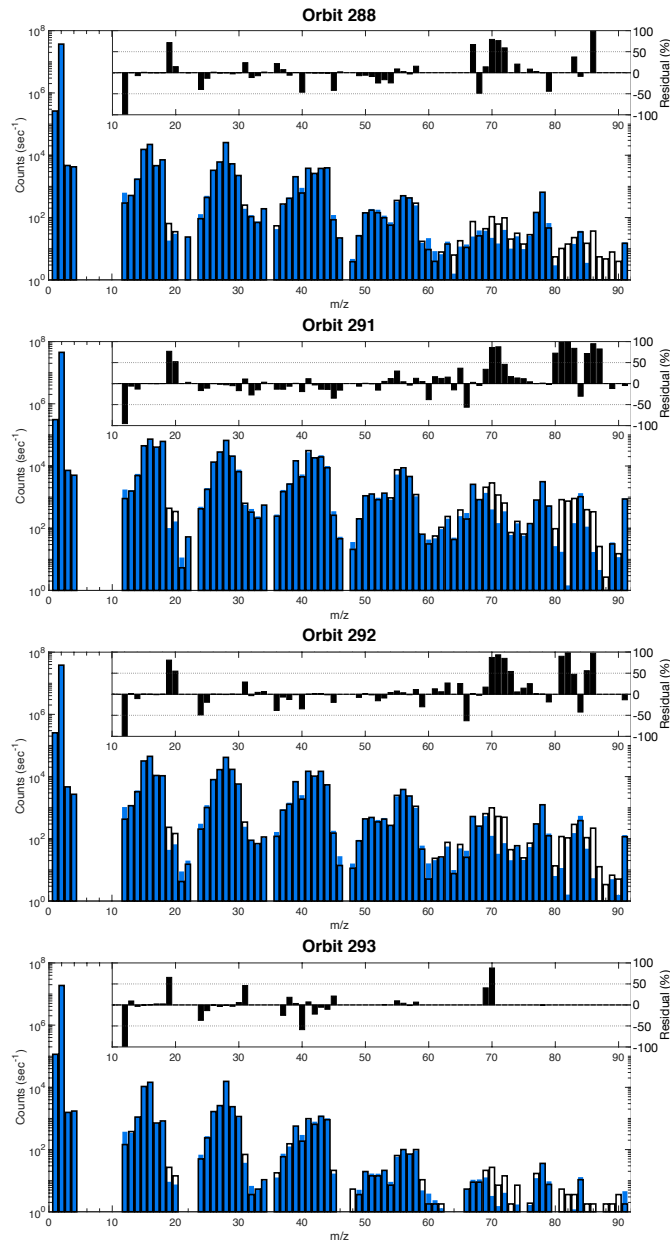
Figure 5.3: Mass spectral deconvolution results for the averaged mass spectra returned from orbits 288, 291, 292, and 293 (atmospheric entry). Black outline bars represent the measured INMS spectrum and blue bars represent the average of the top 10% (50,000) best-fitting simulations. The inset figures in the top right represent the residual to each mass channel. Residuals for mass channels 1 to 4 are not shown and are always below 1%. Residuals for any mass channel with less than 20 counts are not shown. Results for orbit 293 include adsorption corrections described in Section 3.3. The fit for orbit 290 can be found in Figure 5.1 in the text.
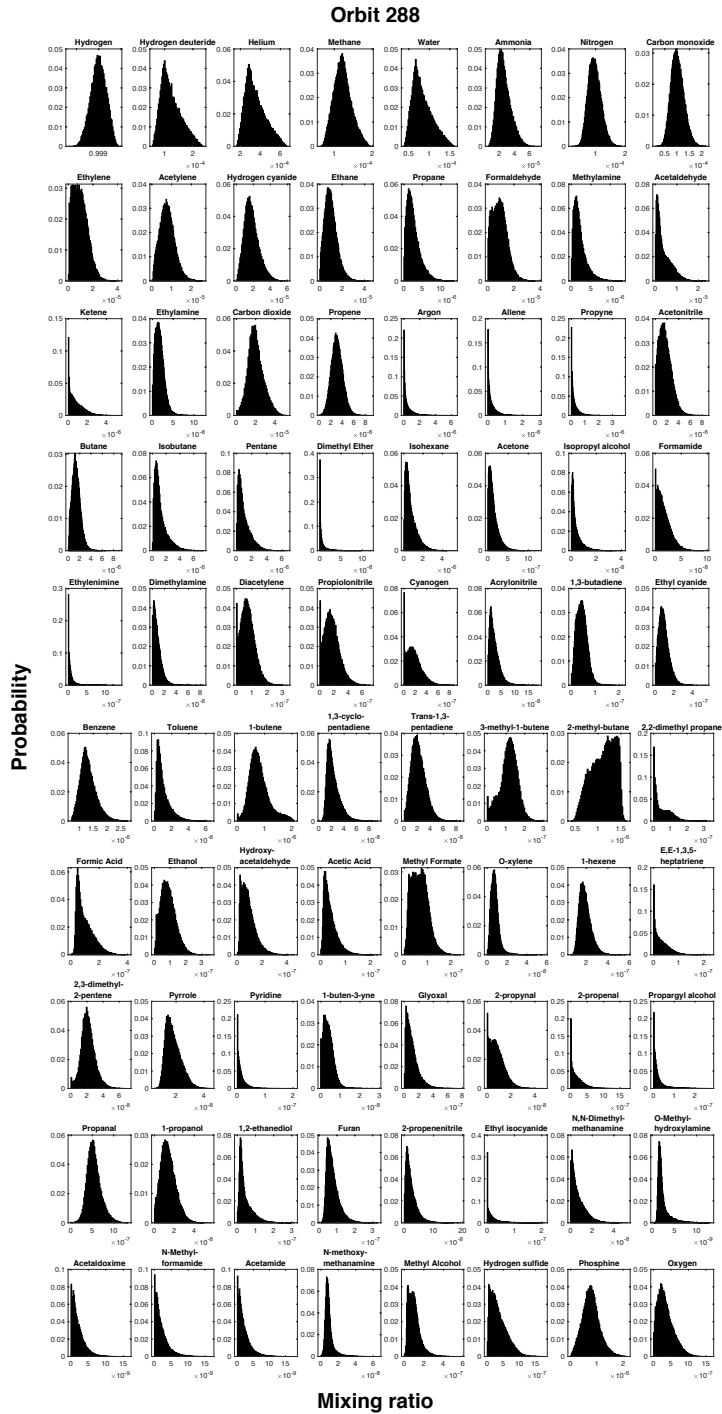
Figure 5.4: Probability densities of the mixing ratios of all species from the mass spectral deconvolution results for the best-fitting 10% (50,000) of simulations for orbit 288.
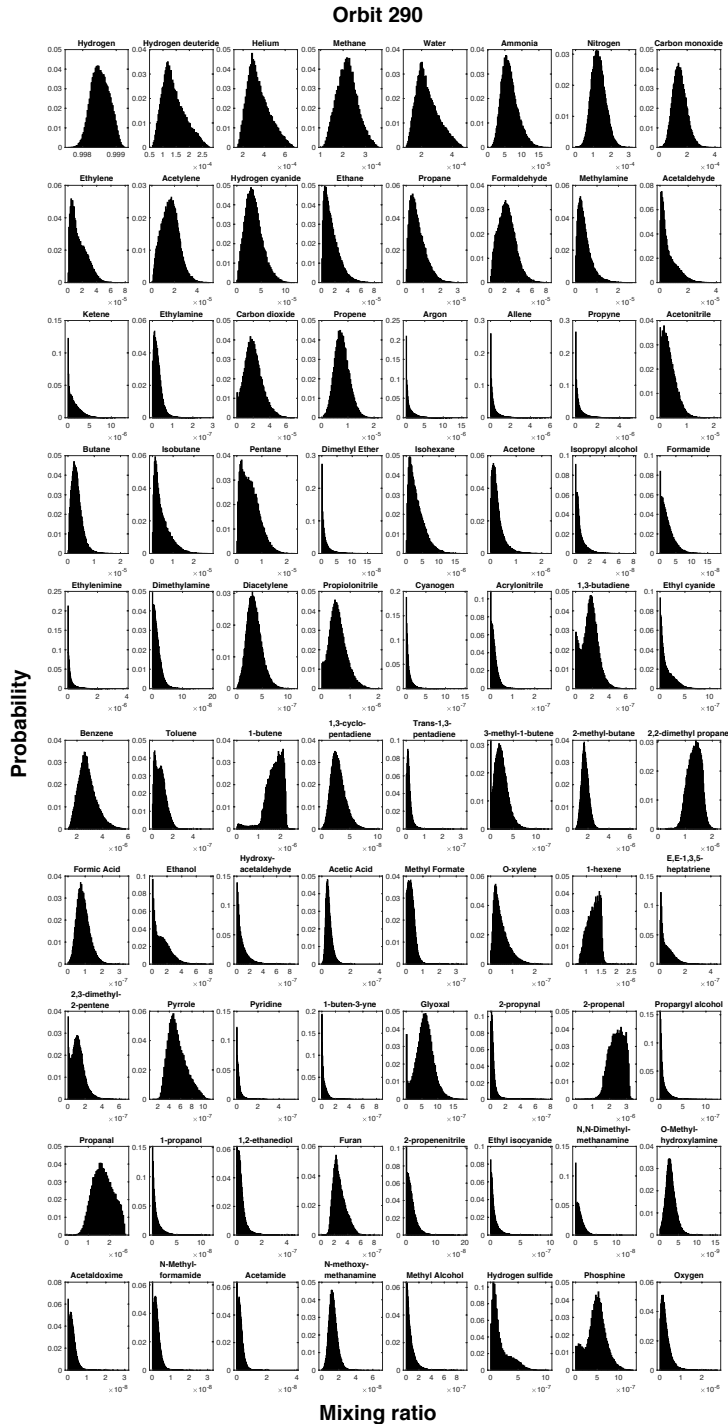
Figure 5.5: Probability densities of the mixing ratios of all species from the mass spectral deconvolution results for the best-fitting 10% (50,000) of simulations for orbit 290.
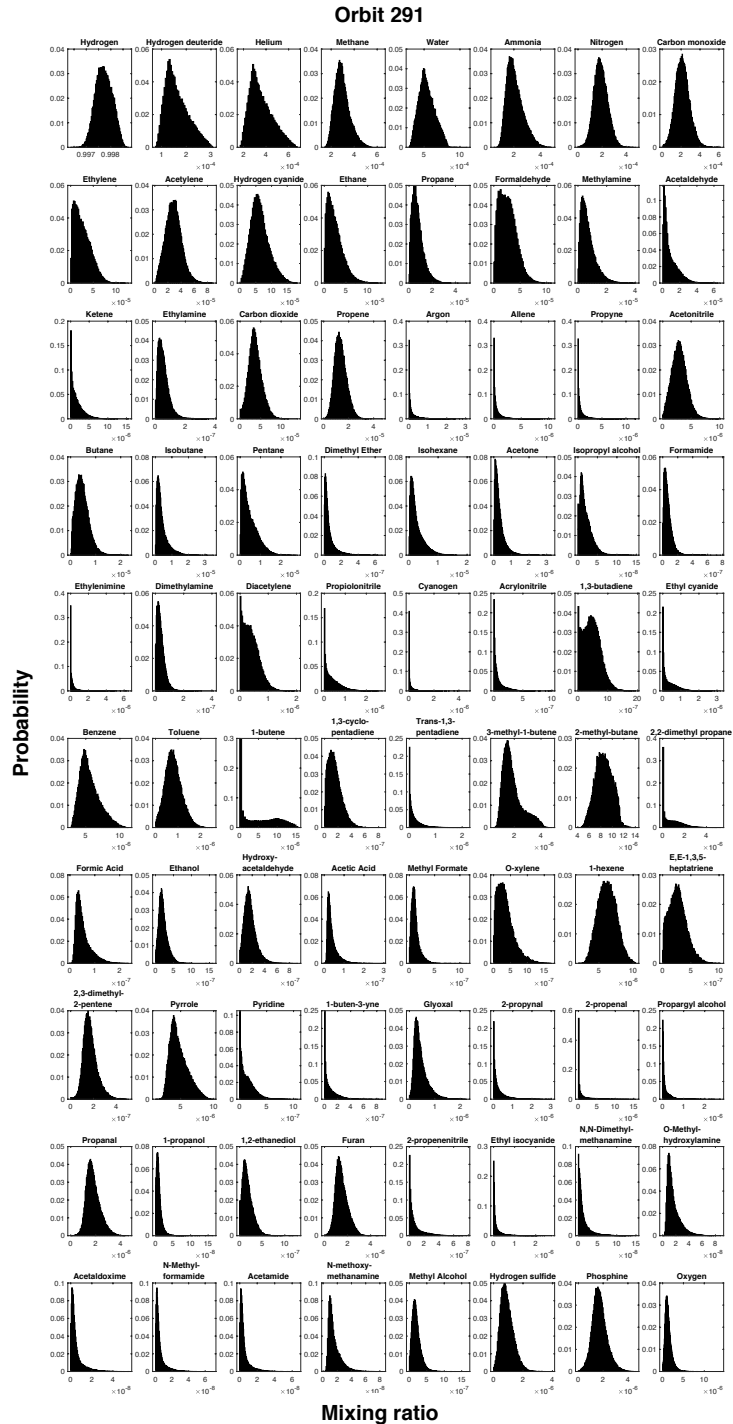
Figure 5.6: Probability densities of the mixing ratios of all species from the mass spectral deconvolution results for the best-fitting 10% (50,000) of simulations for orbit 291.
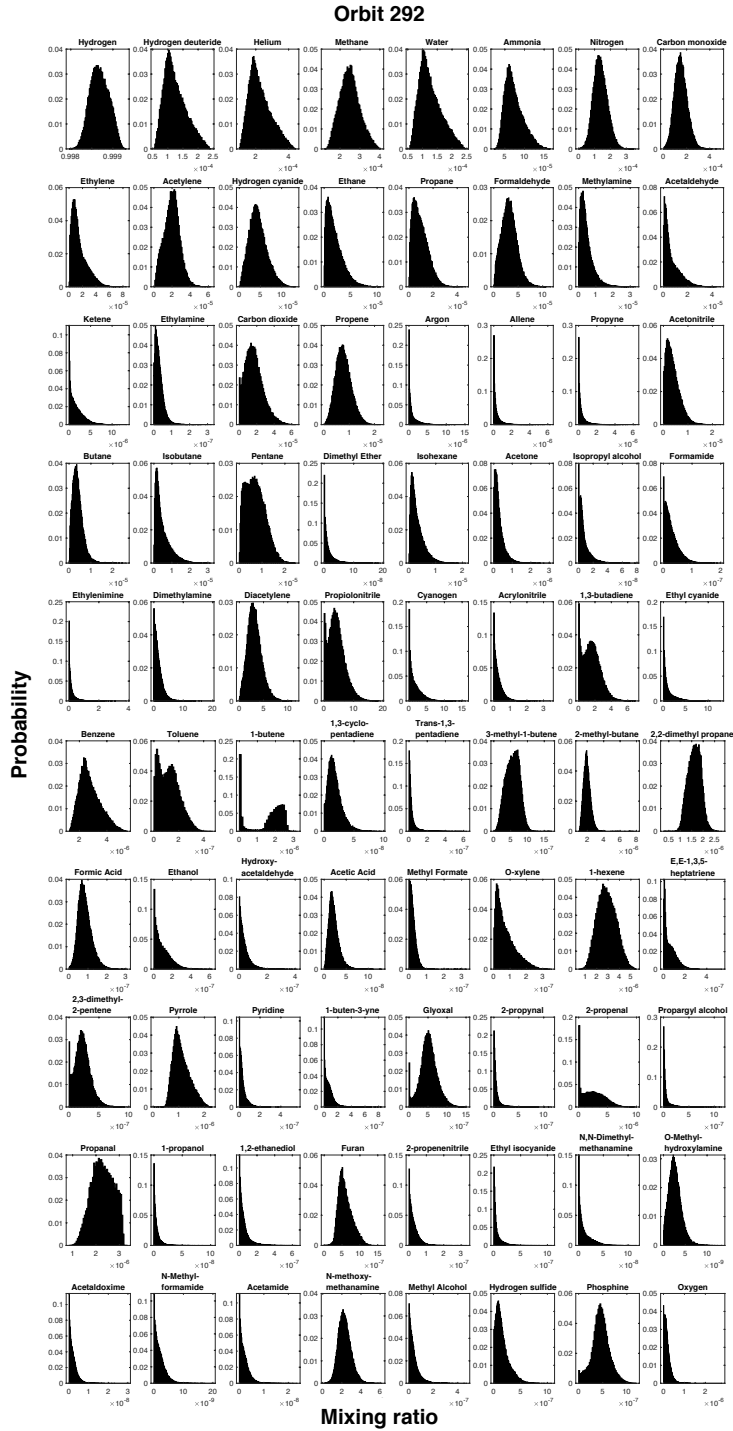
Figure 5.7: Probability densities of the mixing ratios of all species from the mass spectral deconvolution results for the best-fitting 10% (50,000) of simulations for orbit 292.
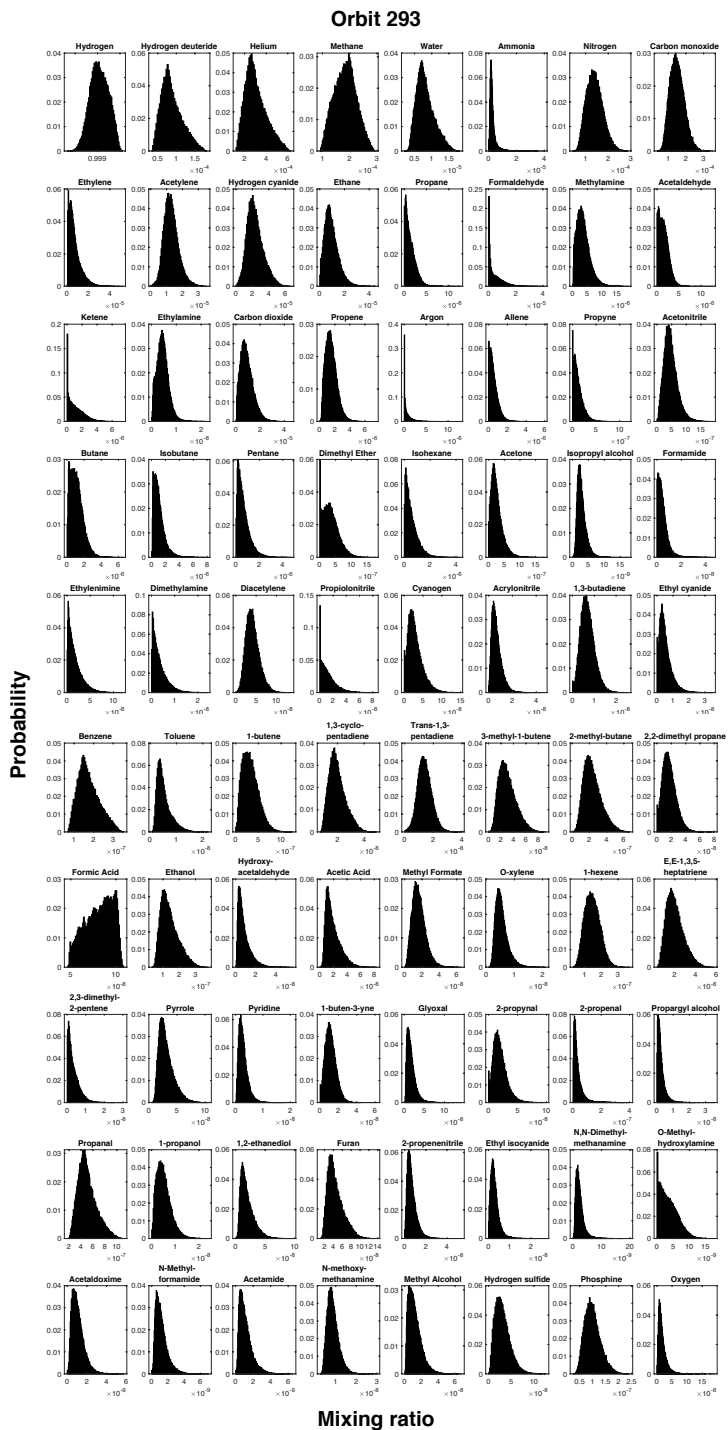
Figure 5.8: Probability densities of the mixing ratios of all species from the mass spectral deconvolution results for the best-fitting 10% (50,000) of simulations for orbit 293.

References

Chadney, JM, TT Koskinen, X Hu, M Galand, P Lavvas, YC Unruh, J Serigano, SM Hörst, and RV Yelle (submitted). "Energy deposition in Saturn's equatorial upper atmosphere". In: *Submitted to Icarus*.

Gautier, Thomas, Joshua A Sebree, Xiang Li, Veronica T Pinnick, Andrej Grubisic, Mark J Loeffler, Stephanie A Getty, Melissa G Trainer, and William B Brinckerhoff (2017). "Influence of trace aromatics on the chemical growth mechanisms of Titan aerosol analogues". In: *Planetary and Space Science* 140, pp. 27–34.

Hörst, Sarah M (2017). "Titan's atmosphere and climate". In: *Journal of Geophysical Research: Planets* 122.3, pp. 432–482.

Hörst, Sarah M and Margaret A Tolbert (2014). "The effect of carbon monoxide on planetary haze formation". In: *The Astrophysical Journal* 781.1, p. 53.

Hörst, Sarah M, Y Heidi Yoon, Melissa S Ugelow, Alex H Parker, Rui Li, Joost A de Gouw, and Margaret A Tolbert (2018). "Laboratory investigations of Titan haze formation: In situ measurement of gas and particle composition". In: *Icarus* 301, pp. 136–151.

Koskinen, TT, JI Moses, RA West, S Guerlet, and A Jouchoux (2016). "The detection of benzene in Saturn's upper atmosphere". In: *Geophysical Research Letters* 43.15, pp. 7895–7901.

Miller, K. E., J. H. Waite, R. S. Perryman, M. E. Perry, A. Bouquet, B. A. Magee, B. Bolton, T. Brockwell, M. M. Hedman, and C. R. Glein (2020). "Cassini INMS constraints on the composition and latitudinal fractionation of Saturn ring rain material". In: *Icarus* 339, p. 113595.

Perry, M. E., B. D. Teolis, D. M. Hurley, B. A. Magee, J. H. Waite, T. G. Brockwell, R. S. Perryman, and R. L. McNutt (2015). "Cassini INMS Measurements of Enceladus Plume Density". In: *Icarus* 257, pp. 139–162.

Perry, M. E., B. Teolis, H. T. Smith, R. L. McNutt, G. G. Fletcher, W. Kasprzak, B. Magee, D. G. Mitchell, and J. H. Waite (2010). "Cassini INMS observations

of neutral molecules in Saturn's E-ring". In: *Journal of Geophysical Research: Space Physics* 115.A10.

Sciamma-O'Brien, Ella, Claire L Ricketts, and Farid Salama (2014). "The Titan Haze Simulation experiment on COSmIC: Probing Titan's atmospheric chemistry at low temperature". In: *Icarus* 243, pp. 325–336.

Sciamma-O'Brien, Ella, Nathalie Carrasco, Cyril Szopa, A Buch, and Guy Cernogora (2010). "Titan's atmosphere: An optimal gas mixture for aerosol production?" In: *Icarus* 209.2, pp. 704–714.

Sebree, Joshua A, Melissa G Trainer, Mark J Loeffler, and Carrie M Anderson (2014). "Titan aerosol analog absorption features produced from aromatics in the far infrared". In: *Icarus* 236, pp. 146–152.

Trainer, Melissa G, Jose L Jimenez, Yuk L Yung, Owen B Toon, and Margaret A Tolbert (2012). "Nitrogen incorporation in CH4-N2 photochemical aerosol produced by far ultraviolet irradiation". In: *Astrobiology* 12.4, pp. 315–326.

Trainer, Melissa G, Joshua A Sebree, Y Heidi Yoon, and Margaret A Tolbert (2013). "The influence of benzene as a trace reactant in Titan aerosol analogs". In: *The Astrophysical Journal Letters* 766.1, p. L4.

Waite, J. H., R. S. Perryman, M. E. Perry, K. E. Miller, J. Bell, T. E. Cravens, C. R. Glein, J. Grimes, M. Hedman, J. Cuzzi, et al. (2018). "Chemical interactions between Saturn's atmosphere and its rings". In: *Science* 362.6410, eaat2382.

Yoon, Y Heidi, Sarah M Hörst, Raea K Hicks, Rui Li, Joost A de Gouw, and Margaret A Tolbert (2014). "The role of benzene photolysis in Titan haze formation". In: *Icarus* 233, pp. 233–241.

Chapter 6

Mixing ratio and density determination

After fitting the spectra using the mass spectral deconvolution algorithm described in Chapter 4, we use the results to determine the atmospheric mixing ratio and density of species included in the database. To determine these values one must take into account the electron impact ionization cross section, σ, which is unique to each species and quantifies the probability of a species to ionize within the instrument. Values for σ can be found in Table 4.1 and are taken from the literature when available. When σ is not available in the literature, we are able to calculate a theoretical ionization cross section using the semi-empirical formula defined in Fitch and Sauter (1983):

$$\sigma = 0.082 + \sum_{i=1}^{8} \alpha_i n_i \tag{6.1}$$

where α_i is a coefficient corresponding to each element and n_i is the number of atoms for that element. This equation is valid for small molecules composed of H, C, N, O, F, Cl, Br, or I atoms, which makes it suitable for our analysis. After taking the ionization cross sections into account, we can calculate atmospheric

mixing ratios for each species, X_s, based on the relative contribution of each species to the mass spectrum as determined by our modeling efforts:

$$X_s = \frac{N_s}{\sigma_s \sum\limits_{i=1}^{n} \frac{N_i}{\sigma_i}} \tag{6.2}$$

where N_s is the concentration of species s returned from the mass spectral deconvolution, σ_s is the ionization cross section for species s, and the summation in the denominator is the sum of the concentration of all species in our database.

We calculate mixing ratios for the averaged mass spectra as well as the ϕ binned mass spectra. The averaged mass spectra, which utilize signal in the same region of Saturn from ϕ of 6.69 to 6.66 $\times$ 10^8 J kg^{-1}, allow us to directly compare measurements from each orbit. Results for the most abundant species in our analysis (mixing ratios above 10^{-5}) are shown in Figure 6.1. H$_2$, which is not included in this figure, always has a mixing ratio greater than 0.998. Mixing ratio results for all species and all orbits can be found in Table 6.2.

H$_2$, HD, and He, which are native to Saturn, show less orbital variability when compared to the other most abundant species in the fit. The HD mixing ratio among orbits ranges from 8.9$\times10^{-5}$ to 1.6$\times10^{-4}$ with an orbital average of 1.3$\pm$0.4$\times10^{-4}$, and the He mixing ratio ranges from 2.3$\times10^{-4}$ to 3.6$\times10^{-4}$ with an orbital average of 3.2$\pm$0.9$\times10^{-4}$. The mixing ratios reported here are not representative of Saturn's bulk atmospheric mixing ratios since these measurements were taken in Saturn's upper thermosphere and well above the homopause. The majority of the remaining spectra is dominated by ices likely originating from the rings and falling into Saturn's atmosphere. CH$_4$

and H_2O are the next most abundant species, with average mixing ratios of $2.1\pm0.4\times10^{-4}$ and $2.0\pm0.5\times10^{-4}$, respectively, followed by CO, N_2, and NH_3. We include both corrected (filled data point) and uncorrected (unfilled data point) values for orbit 293 for H_2O and NH_3, which suffer from adsorption in the instrument as previously described in Section 3.3. Even with corrections to orbit 293, H_2O and NH_3 are still severely depleted during atmospheric entry. Orbit 293 sampled a different latitudinal region of Saturn at closest approach (9° N, compared to 5° S for other orbits) and did not cross the ring plane, which could explain the observed depletion in these measurements. The depletion and overall large variability with these species could also be due to other factors, which will be discussed in the following subsection.

Figure 6.2 shows the mixing ratio results after binning the data using ϕ bins of 0.01×10^8 J kg^{-1} and running each bin section as a separate mass spectrum. This provides a profile that allows for a better sense of any deviations among the species. Orbit 293 measurements extend down further than the other orbits since the spacecraft probed lower into Saturn's atmosphere before loss of signal. The extent of our ϕ binned analysis depends on the strength of the signal at higher altitudes (lower ϕ) and we utilize counts as long as the signal-to-noise ratio is sufficient for analysis. The H_2 mixing ratio profile (upper left subfigure) decreases deeper in the atmosphere due to the increasing abundances of other species, mainly HD and He, further into the planet. As the H_2 native to Saturn begins to decrease with height, the mixing ratio again decreases relative to the incoming material from the rings. Aside from HD and He, the mixing ratios of the other species are more or less constant, which
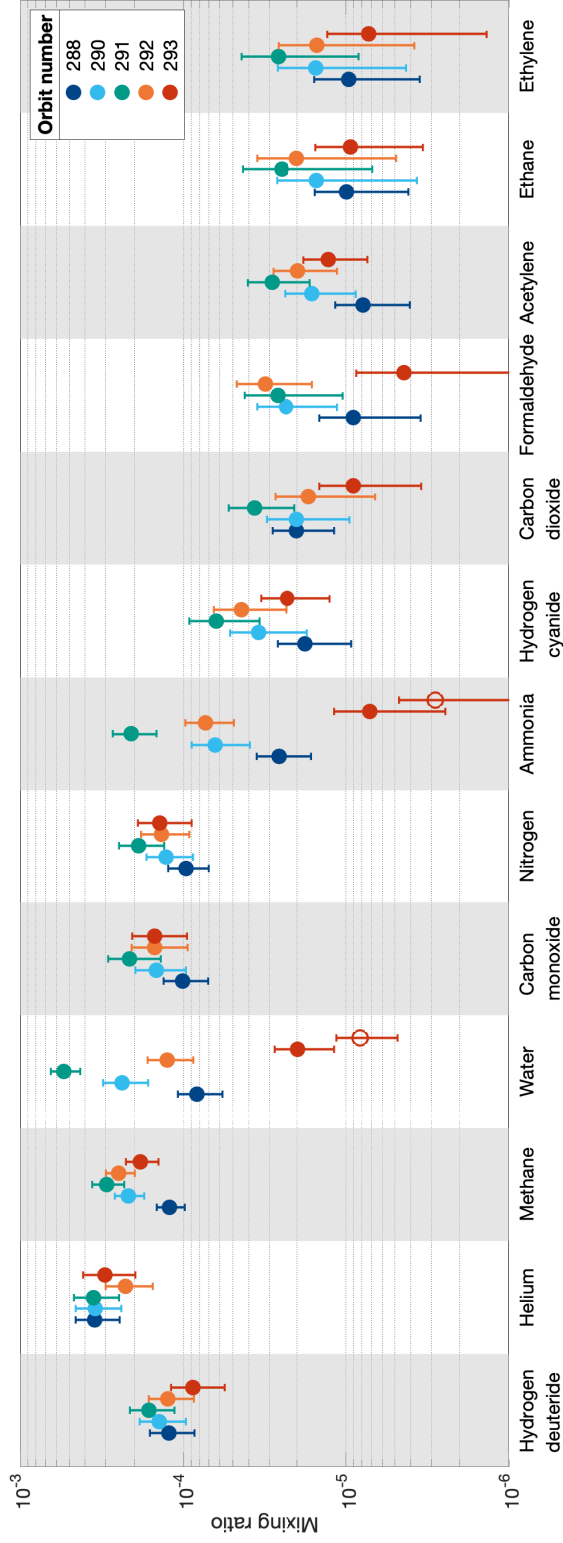
Figure 6.1: Mixing ratio results for the average mass spectrum for all orbits analyzed in this study. Average mass spectra include measurements taken between ϕ of 6.69 and 6.66×10^8 J kg^{-1}. The species included here are all species aside from H$_2$ with a mixing ratio above 10^{-5} after averaging the results of all orbits. Results for H$_2$O and NH$_3$ for orbit 293 include both adsorption corrected (filled data point) and uncorrected (unfilled data point) values. Error bars are a combination of 1σ uncertainties from counting statistics and 1σ uncertainties from the mass spectral deconvolution.

is expected for species with a downward external flux into the atmosphere. However, the mixing ratios do slightly increase at the top and bottom of the profiles in response to the H_2 mixing ratio profile. HD and He decrease in abundance with increasing altitude, which is expected for species native to the planet and following diffusive equilibrium above the homopause.

Similar to the mixing ratio profiles, we use our model results along with the corrections for sensitivity and ram enhancement discussed in Chapter 3 to determine density profiles for these species. We determine the density profiles for the most abundant species by weighting the count rate from the species' base peak with the relative contribution of that species returned by the model for each ϕ bin using the equation

$$n_s = \beta \times \frac{N_s}{REF \times sens_s} \text{ cm}^{-3} \tag{6.3}$$

where n_s is the number density of species s, N_s is the concentration of species s returned from the mass spectral deconvolution, and REF and $sens_s$ are the ram enhancement and sensitivity factors described in Chapter 3. β is a detector sensitivity correction factor of 2.2. This value is from a revised INMS instrument sensitivity model detailed in Teolis et al. (2015) after a post flight re-analysis of the instrument. Density results are shown in Figure 6.3. H_2 is plotted in the top left subfigure and the average H_2 density profile is plotted in all other subfigures in order to compare profiles. All species aside from HD and He follow a similar profile trend to H_2, again indicative of an external source for these species, while HD and He follow the trend of a species diffusively separating above the homopause.
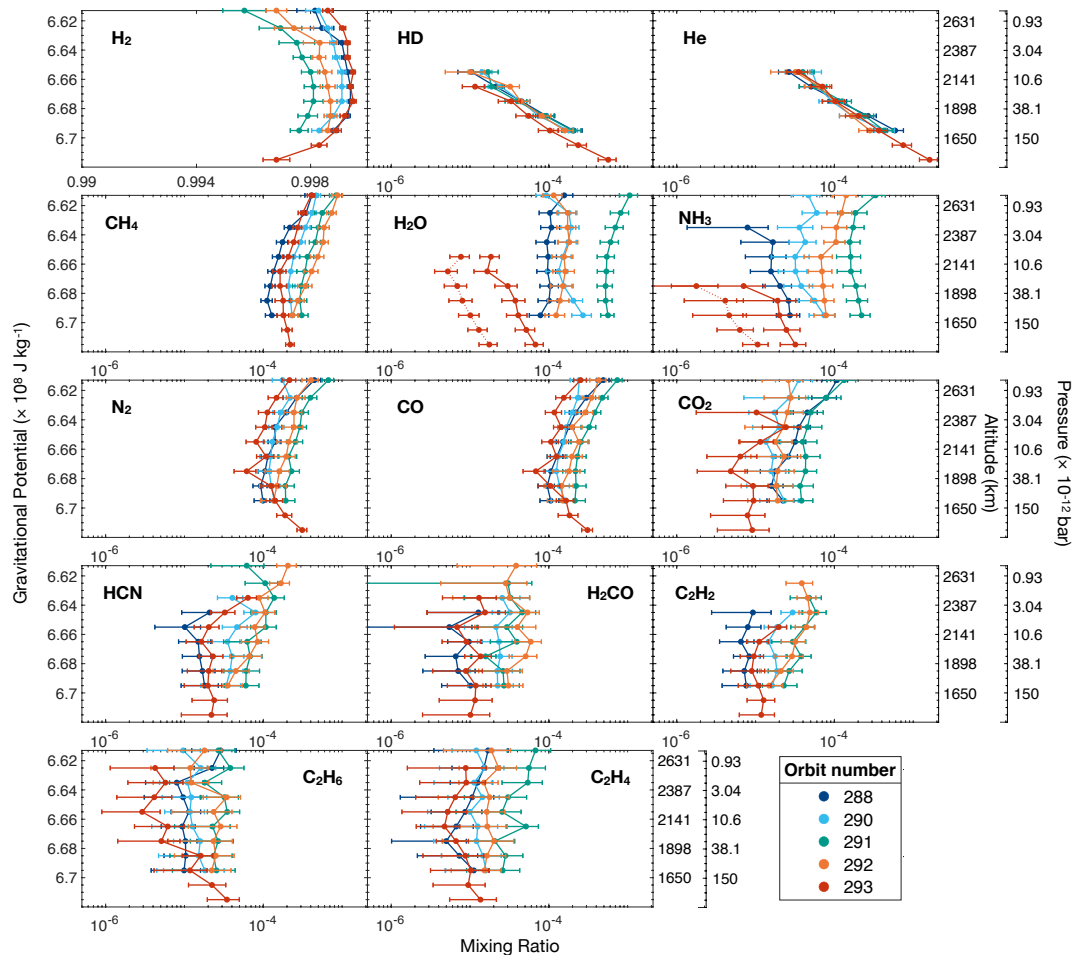
Figure 6.2: Inbound mixing ratio profiles of the most abundant species in our mass spectral fits. Profiles are constructed by averaging INMS measurements in gravitational potential bins of 0.01×10^8 J kg^{-1} and performing a mass spectral deconvolution for each individual bin. Results for H_2O and NH_3 for orbit 293 include both adsorption corrected (solid line) and uncorrected (dotted line) values. Error bars are a combination of 1σ uncertainties from counting statistics and 1σ uncertainties from the mass spectral deconvolution. The corresponding pressure and altitude above the 1 bar pressure level are presented on the right y axis.
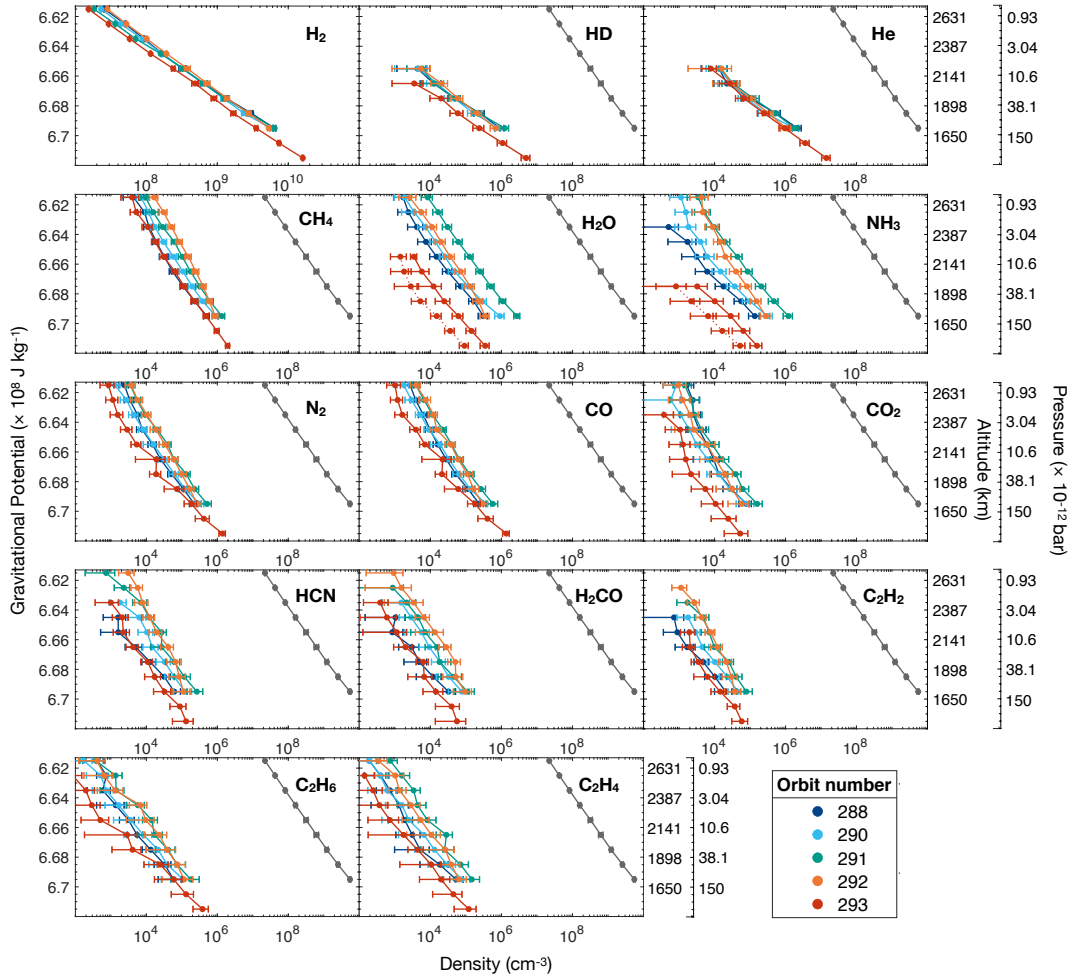
Figure 6.3: Inbound density profiles of the most abundant species in our mass spectral fits. The average H_2 density profile is plotted in grey on each subfigure in order to easily compare profiles. Profiles are constructed by averaging INMS measurements in gravitational potential bins of 0.01×10^8 J kg^{-1} and performing a mass spectral deconvolution for each individual bin. Results for H_2O and NH_3 for orbit 293 include both adsorption corrected (solid line) and uncorrected (dotted line) values. Error bars are a combination of 1σ uncertainties from counting statistics and 1σ uncertainties from the mass spectral deconvolution. The corresponding pressure and altitude above the 1 bar pressure level are presented on the right y axis.

6.1 Variability

Non-native species exhibit a greater overall variability from orbit to orbit, which is likely a consequence of the atmospheric dynamics associated with this very tenuous region. Measurements were taken at similar latitude and similar local solar time (aside from atmospheric entry) but did have a larger longitudinal range (see Table 2.1 in Chapter 2). Additionally, temporal variations could effect these results as these measurements were taken over the course of about a month from August to September of 2017. This region is exposed to the fluctuating solar wind, magnetospheric plasma, cosmic ray impacts, micrometeorite bombardment, and other high energy phenomena, which could impart excess energy into the region and change the temperature, dynamics, and chemistry affecting the inner rings. Any fluctuations could lead to varying amounts of infalling ring material as observed by the instrument. Also, as first noted by Waite et al. (2018), dynamical disruptions in the area, such as the D68 ringlet disruption noted in Hedman et al. (2014), may cause local disturbances that influence the influx of material.

The volatility and proton affinity of these species could play a role in the observed variability and could also be responsible for the surprising prevalence of non-water ice and high mass organics in the spectra. Figure 6.4 shows the sublimation pressure of the most abundant species at ring relevant temperatures of approximately 80 to 115 K (Filacchione et al. (2014) and Tiscareno et al. (2019)) taken from Fray and Schmitt (2009). Energetic events or disruptions in the area will lead to the liberation of molecules from larger ring particles and a molecule's ability to recondense back onto a ring

particle after liberation is highly dependent on the sublimation pressure. At ring relevant temperatures, N_2, CO, and CH_4, the most abundant nonwater ices in our fit, have the highest sublimation pressures. It's possible that these species are being preferentially lost into Saturn from the rings since their high sublimation pressures make it difficult to recondense back onto a ring particle. On the other hand, H_2O has the lowest sublimation pressure and can more easily recondense back onto a ring particle and evade loss into Saturn's atmosphere, which could explain why the abundance of H_2O is relatively low when compared to other volatile species from the rings.

The proton affinity of a species could also affect the abundances observed by INMS. Proton affinities of the most abundant non-native species are taken from Hunter and Lias (1998) and can be found in Table 6.1. A species with a higher proton affinity is more likely to be protonated after liberation from a ring particle. Any protonated molecule would evade detection by INMS in CSN mode since the instrument is only sensitive to neutral molecules in this mode. Thus, it's possible that species like H_2O and NH_3, which have higher proton affinities, are entering Saturn's atmosphere in a charged form (e.g., H_3O^+ and NH_4^+) and not being detected by INMS. CH_4, CO, and N_2, on the other hand, are the most abundant non-water volatiles and have some of the lowest proton affinities compared to other abundant volatiles. Unfortunately the INMS Open Source Ion (OSI) mode was only able to measure up to *m/z* 8 amu due to the high speed of the spacecraft during the last orbits (Waite et al., 2018), so detection of larger ions from in situ measurements is not possible. Remote observations do suggest that charged H_2O from the rings is entering

Table 6.1: Proton affinities of the most abundant non-native species, taken from Hunter and Lias (1998).

Species	Proton affinity (kJ/mol)
NH_3	853.6
H_2CO	712.9
HCN	712.9
H_2O	691.0
C_2H_4	680.5
C_2H_2	641.4
C_2H_6	596.3
CO	594.0
CH_4	543.5
CO_2	540.5
N_2	493.8

Saturn's atmosphere. Ground based observations from the Keck telescope discovered variations in Saturn's midlatitude H_3^+ intensity that they attribute to the presence of charged species derived from H_2O that were transported to Saturn's midlatitudes via regions of the rings that are magnetically linked to the atmosphere (O'Donoghue et al. (2013), O'Donoghue et al. (2017), and O'Donoghue et al. (2019)). Further ground and space based searches for definitive ion detections in this region would be very impactful. ALMA and JWST, with their unprecedented spectral and spatial resolutions, will certainly be able to improve our understanding of the relationship between Saturn's atmosphere and rings and the transport processes involved with this connection.
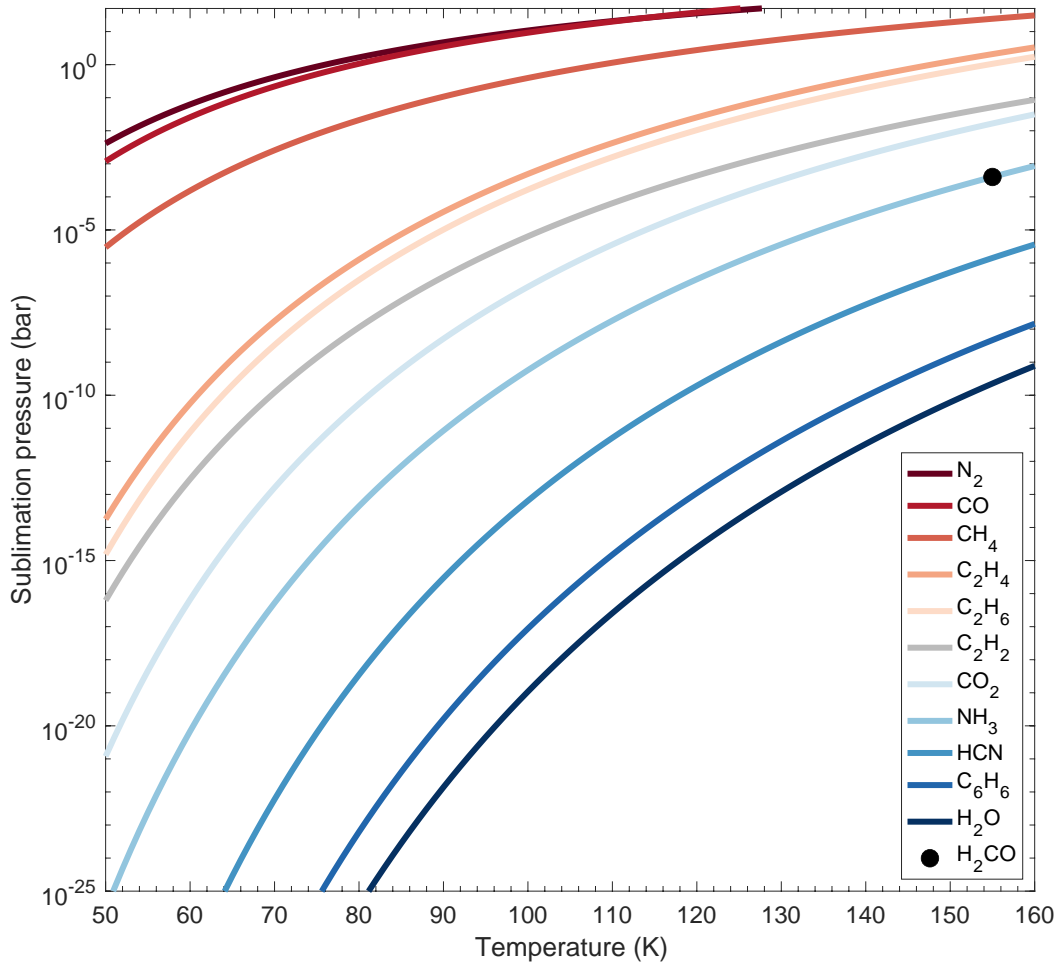
Figure 6.4: Sublimation pressure curves for the most abundant non-native species in our mass spectral fits at temperatures relevant to Saturn's rings. Values in this figure are taken from Fray and Schmitt (2009).

Table 6.2: Mixing ratio results for all species and all orbits. Species are listed from highest to lowest mixing ratio based on the average mixing ratio of all orbits (last column).

| Species name	Species formula	Orbit 288	Orbit 290	Orbit 291	Orbit 292	Orbit 293	Average
Hydrogen	H_2	$0.99 \pm (1.7\times10^{-5})$	$0.99 \pm (2.7\times10^{-5})$	$0.99 \pm (3.4\times10^{-5})$	$0.99 \pm (2.2\times10^{-5})$	$0.99 \pm (2.1\times10^{-5})$	$0.99 \pm (2.4\times10^{-5})$
Helium	He	$3.5 \pm 1\times10^{-4}$	$3.5 \pm 1\times10^{-4}$	$3.6 \pm 1\times10^{-4}$	$2.3 \pm 0.7\times10^{-4}$	$3 \pm 1\times10^{-4}$	$3.2 \pm 0.9\times10^{-4}$
Methane	CH_4	$1.2 \pm 0.2\times10^{-4}$	$2.2 \pm 0.5\times10^{-4}$	$3 \pm 0.6\times10^{-4}$	$2.5 \pm 0.5\times10^{-4}$	$1.8 \pm 0.4\times10^{-4}$	$2.1 \pm 0.4\times10^{-4}$
Water	H_2O	$8.3 \pm 2.4\times10^{-5}$	$2.4 \pm 0.7\times10^{-4}$	$5.4 \pm 1.1\times10^{-4}$	$1.3 \pm 0.4\times10^{-4}$	$2 \pm 0.6\times10^{-5}$	$2 \pm 0.5\times10^{-4}$
Carbon monoxide	CO	$1 \pm 0.3\times10^{-4}$	$1.5 \pm 0.5\times10^{-4}$	$2.1 \pm 0.8\times10^{-4}$	$1.5 \pm 0.6\times10^{-4}$	$1.5 \pm 0.4\times10^{-4}$	$1.5 \pm 0.5\times10^{-4}$
Nitrogen	N_2	$9.7 \pm 2.2\times10^{-5}$	$1.3 \pm 0.4\times10^{-4}$	$1.9 \pm 0.6\times10^{-4}$	$1.4 \pm 0.4\times10^{-4}$	$1.4 \pm 0.4\times10^{-4}$	$1.4 \pm 0.4\times10^{-4}$
Hydrogen deuteride	HD	$1.2 \pm 0.4\times10^{-4}$	$1.4 \pm 0.4\times10^{-4}$	$1.6 \pm 0.5\times10^{-4}$	$1.3 \pm 0.4\times10^{-4}$	$8.8 \pm 2.8\times10^{-5}$	$1.3 \pm 0.4\times10^{-4}$
Ammonia	NH_3	$2.6 \pm 0.9\times10^{-5}$	$6.4 \pm 2.4\times10^{-5}$	$2.1 \pm 0.6\times10^{-4}$	$7.3 \pm 2.3\times10^{-5}$	$7.2 \pm 4.4\times10^{-6}$	$7.6 \pm 2.4\times10^{-5}$
Hydrogen cyanide	HCN	$1.8 \pm 0.9\times10^{-5}$	$3.5 \pm 1.7\times10^{-5}$	$6.3 \pm 2.9\times10^{-5}$	$4.4 \pm 2.1\times10^{-5}$	$2.3 \pm 1\times10^{-5}$	$3.7 \pm 1.7\times10^{-5}$
Carbon dioxide	CO_2	$2 \pm 0.8\times10^{-5}$	$2 \pm 1.1\times10^{-5}$	$3.7 \pm 1.6\times10^{-5}$	$1.7 \pm 1\times10^{-5}$	$9 \pm 5.3\times10^{-6}$	$2.1 \pm 1\times10^{-5}$
Formaldehyde	H_2CO	$9 \pm 5.5\times10^{-6}$	$2.3 \pm 1.2\times10^{-5}$	$2.6 \pm 1.6\times10^{-5}$	$3.2 \pm 1.5\times10^{-5}$	$4.4 \pm 5\times10^{-6}$	$1.9 \pm 1.1\times10^{-5}$
Acetylene	C_2H_2	$7.9 \pm 3.7\times10^{-6}$	$1.6 \pm 0.8\times10^{-5}$	$2.9 \pm 1.2\times10^{-5}$	$2 \pm 0.8\times10^{-5}$	$1.3 \pm 0.5\times10^{-5}$	$1.7 \pm 0.7\times10^{-5}$
Ethane	C_2H_6	$9.9 \pm 5.5\times10^{-6}$	$1.5 \pm 1.1\times10^{-5}$	$2.5 \pm 1.8\times10^{-5}$	$2 \pm 1.5\times10^{-5}$	$9.4 \pm 5.5\times10^{-6}$	$1.6 \pm 1.1\times10^{-5}$
Ethylene	C_2H_4	$9.6 \pm 5.9\times10^{-6}$	$1.5 \pm 1.1\times10^{-5}$	$2.6 \pm 1.8\times10^{-5}$	$1.5 \pm 1.1\times10^{-5}$	$7.2 \pm 5.6\times10^{-6}$	$1.5 \pm 1\times10^{-5}$
Propene	C_3H_6	$3.1 \pm 1\times10^{-6}$	$7.7 \pm 2.8\times10^{-6}$	$1.4 \pm 0.5\times10^{-5}$	$7.7 \pm 3.1\times10^{-6}$	$1.5 \pm 0.7\times10^{-6}$	$6.7 \pm 2.5\times10^{-6}$
Propane	C_3H_8	$2.6 \pm 1.8\times10^{-6}$	$6.7 \pm 4.5\times10^{-6}$	$7.5 \pm 4.9\times10^{-6}$	$9.6 \pm 6.2\times10^{-6}$	$1.3 \pm 1.1\times10^{-6}$	$5.5 \pm 3.7\times10^{-6}$
Acetaldehyde	C_2H_4O	$3.9 \pm 3.4\times10^{-6}$	$6.1 \pm 5.7\times10^{-6}$	$8.7 \pm 8.2\times10^{-6}$	$6.7 \pm 6.3\times10^{-6}$	$1.4 \pm 1\times10^{-6}$	$5.4 \pm 4.9\times10^{-6}$
Methylamine	CH_5N	$2.2 \pm 1.7\times10^{-6}$	$4.2 \pm 3.2\times10^{-6}$	$7.1 \pm 5.1\times10^{-6}$	$4.6 \pm 3.7\times10^{-6}$	$3.8 \pm 2.2\times10^{-6}$	$4.4 \pm 3.2\times10^{-6}$
Pentane	C_5H_{12}	$1 \pm 0.8\times10^{-6}$	$5.4 \pm 3.5\times10^{-6}$	$4.7 \pm 3.7\times10^{-6}$	$7.1 \pm 4.2\times10^{-6}$	$6.4 \pm 5\times10^{-7}$	$3.8 \pm 2.5\times10^{-6}$
Isobutane	C_4H_{10}	$1.2 \pm 0.9\times10^{-6}$	$4.6 \pm 3.8\times10^{-6}$	$4 \pm 3.4\times10^{-6}$	$4.7 \pm 4.1\times10^{-6}$	$1.1 \pm 0.8\times10^{-6}$	$3.1 \pm 2.6\times10^{-6}$
Butane	C_4H_{10}	$1.4 \pm 0.7\times10^{-6}$	$3.3 \pm 2\times10^{-6}$	$4.7 \pm 2.6\times10^{-6}$	$4 \pm 2.4\times10^{-6}$	$1.1 \pm 0.7\times10^{-6}$	$2.9 \pm 1.7\times10^{-6}$
2-methyl-butane	C_5H_{12}	$1.1 \pm 0.3\times10^{-6}$	$1.7 \pm 0.4\times10^{-6}$	$8.5 \pm 1.5\times10^{-6}$	$2 \pm 0.4\times10^{-6}$	$2.4 \pm 1\times10^{-7}$	$2.7 \pm 0.5\times10^{-6}$
Benzene	C_6H_6	$1.3 \pm 0.3\times10^{-6}$	$2.8 \pm 0.7\times10^{-6}$	$5.6 \pm 1.4\times10^{-6}$	$2.8 \pm 0.8\times10^{-6}$	$1.7 \pm 0.5\times10^{-7}$	$2.5 \pm 0.6\times10^{-6}$
Acetonitrile	CH_3CN	$1.7 \pm 1.1\times10^{-6}$	$3.4 \pm 2.5\times10^{-6}$	$2.9 \pm 1.3\times10^{-6}$	$3.9 \pm 2.7\times10^{-6}$	$4.6 \pm 2.3\times10^{-7}$	$2.5 \pm 1.6\times10^{-6}$
1-hexene	C_6H_{12}	$1.9 \pm 0.5\times10^{-7}$	$1.2 \pm 0.2\times10^{-6}$	$6.2 \pm 1.3\times10^{-6}$	$2.9 \pm 0.8\times10^{-6}$	$1.5 \pm 0.5\times10^{-7}$	$2.1 \pm 0.5\times10^{-6}$
Isohexane	C_6H_{14}	$7.3 \pm 6\times10^{-7}$	$3.2 \pm 2.3\times10^{-6}$	$2.7 \pm 2.3\times10^{-6}$	$3.1 \pm 2.4\times10^{-6}$	$5.4 \pm 4.6\times10^{-7}$	$2 \pm 1.6\times10^{-6}$
1-butene	C_4H_8	$7.9 \pm 3.6\times10^{-7}$	$1.7 \pm 0.4\times10^{-6}$	$5 \pm 4.7\times10^{-6}$	$1.5 \pm 0.9\times10^{-6}$	$3.2 \pm 1.7\times10^{-7}$	$1.9 \pm 1.3\times10^{-6}$
Propanal	C_3H_6O	$5.4 \pm 1.6\times10^{-7}$	$1.7 \pm 0.5\times10^{-6}$	$1.8 \pm 0.6\times10^{-6}$	$2.3 \pm 0.5\times10^{-6}$	$5.1 \pm 1.5\times10^{-7}$	$1.4 \pm 0.4\times10^{-6}$
Ketene	C_2H_2O	$8 \pm 7.4\times10^{-7}$	$1.5 \pm 1.4\times10^{-6}$	$1.6 \pm 1.6\times10^{-6}$	$1.6 \pm 1.6\times10^{-6}$	$1.2 \pm 1\times10^{-6}$	$1.3 \pm 1.3\times10^{-6}$
Pyrrole	C_4H_5N	$1.8 \pm 0.5\times10^{-8}$	$5.4 \pm 1.6\times10^{-7}$	$4.7 \pm 1.3\times10^{-6}$	$1.1 \pm 0.3\times10^{-6}$	$3.1 \pm 1.3\times10^{-8}$	$1.3 \pm 0.4\times10^{-6}$
2-propenal	C_3H_4O	$1.9 \pm 1.9\times10^{-7}$	$2.4 \pm 0.4\times10^{-6}$	$9.3 \pm 9\times10^{-7}$	$2.4 \pm 1.9\times10^{-6}$	$3.4 \pm 3.7\times10^{-8}$	$1.2 \pm 0.9\times10^{-6}$
Argon	Ar	$4.6 \pm 4.1\times10^{-7}$	$9.8 \pm 9\times10^{-7}$	$1.6 \pm 1.4\times10^{-6}$	$9.5 \pm 9\times10^{-7}$	$7.5 \pm 7\times10^{-7}$	$9.5 \pm 9\times10^{-6}$
2,2-dimethyl propane	C_5H_{12}	$4.9 \pm 4.8\times10^{-8}$	$1.3 \pm 0.2\times10^{-6}$	$7.2 \pm 8.1\times10^{-7}$	$1.6 \pm 0.3\times10^{-6}$	$1.7 \pm 0.9\times10^{-8}$	$7.5 \pm 2.8\times10^{-7}$

Table 6.2 – continued from previous page

Species name	Species formula	Orbit 288	Orbit 290	Orbit 291	Orbit 292	Orbit 293	Average
Phosphine	PH_3	$7.8 \pm 3.2\times10^{-7}$	$4.8 \pm 2.2\times10^{-6}$	$1.7 \pm 0.6\times10^{-6}$	$4.6 \pm 1.8\times10^{-7}$	$9.9 \pm 3\times10^{-8}$	$7 \pm 2.7\times10^{-7}$
3-methyl-1-butene	C_5H_{10}	$1.1 \pm 0.5\times10^{-7}$	$2.3 \pm 1.4\times10^{-7}$	$1.9 \pm 0.7\times10^{-6}$	$5.6 \pm 2\times10^{-7}$	$3 \pm 1.4\times10^{-8}$	$5.6 \pm 2.3\times10^{-7}$
Furan	C_4H_4O	$7.5 \pm 3.5\times10^{-8}$	$2.8 \pm 0.9\times10^{-7}$	$1.5 \pm 0.5\times10^{-6}$	$5.9 \pm 1.9\times10^{-7}$	$4.5 \pm 1.8\times10^{-8}$	$4.9 \pm 1.7\times10^{-7}$
Oxygen	O_2	$3.4 \pm 2.3\times10^{-7}$	$2.8 \pm 2.4\times10^{-7}$	$1.3 \pm 0.8\times10^{-6}$	$1.7 \pm 1.4\times10^{-7}$	$1.8 \pm 1.4\times10^{-8}$	$4.3 \pm 2.8\times10^{-7}$
Allene	CH_2CCH_2	$2.2 \pm 2.6\times10^{-7}$	$3.5 \pm 4.8\times10^{-7}$	$5.6 \pm 8.4\times10^{-7}$	$3.1 \pm 4.3\times10^{-7}$	$5.7 \pm 4.6\times10^{-7}$	$4 \pm 4.9\times10^{-7}$
Glyoxal	$C_2H_2O_2$	$1.1 \pm 0.9\times10^{-7}$	$5.8 \pm 2.8\times10^{-7}$	$4.4 \pm 2.6\times10^{-7}$	$5.1 \pm 2.2\times10^{-7}$	$1.7 \pm 1.1\times10^{-8}$	$3.3 \pm 1.7\times10^{-7}$
Hydrogen sulfide	H_2S	$3.6 \pm 2.5\times10^{-7}$	$1.8 \pm 1.6\times10^{-7}$	$9.1 \pm 4.4\times10^{-7}$	$1.6 \pm 1.2\times10^{-7}$	$3.1 \pm 1.6\times10^{-8}$	$3.3 \pm 2\times10^{-7}$
Propyne	CH_3CCH	$2.2 \pm 2.7\times10^{-7}$	$3.6 \pm 5.1\times10^{-7}$	$5.9 \pm 8.9\times10^{-7}$	$3.3 \pm 4.5\times10^{-7}$	$1.2 \pm 1\times10^{-7}$	$3.2 \pm 4.5\times10^{-7}$
Propiolonitrile	C_2HCN	$1.7 \pm 1.1\times10^{-7}$	$5.6 \pm 2.9\times10^{-7}$	$3.6 \pm 3.7\times10^{-7}$	$4.2 \pm 2.7\times10^{-7}$	$1.2 \pm 1.1\times10^{-8}$	$3.1 \pm 2.1\times10^{-7}$
Acetone	C_3H_6O	$1.4 \pm 1.2\times10^{-7}$	$2.6 \pm 2.3\times10^{-7}$	$3.2 \pm 2.9\times10^{-7}$	$2.9 \pm 2.7\times10^{-7}$	$2.6 \pm 1.8\times10^{-7}$	$2.5 \pm 2.2\times10^{-7}$
Diacetylene	C_4H_2	$7.4 \pm 4.5\times10^{-8}$	$3.4 \pm 1.4\times10^{-7}$	$3.9 \pm 2.8\times10^{-7}$	$3.2 \pm 1.4\times10^{-7}$	$4.1 \pm 1.6\times10^{-8}$	$2.3 \pm 1.3\times10^{-7}$
Toluene	C_7H_8	$1 \pm 0.8\times10^{-8}$	$7.8 \pm 5\times10^{-8}$	$8 \pm 3.6\times10^{-7}$	$1.2 \pm 0.8\times10^{-7}$	$5.2 \pm 2.7\times10^{-9}$	$2 \pm 1\times10^{-7}$
1,3-Butadiene	C_4H_6	$4.4 \pm 2.2\times10^{-8}$	$1.7 \pm 0.9\times10^{-7}$	$4.6 \pm 2.9\times10^{-7}$	$1.6 \pm 1\times10^{-7}$	$6.9 \pm 3.2\times10^{-9}$	$1.7 \pm 1\times10^{-7}$
Ethylenimine	C_2H_5N	$6.6 \pm 9.7\times10^{-8}$	$1.9 \pm 2.6\times10^{-7}$	$2.4 \pm 4\times10^{-7}$	$1.9 \pm 2.5\times10^{-7}$	$1.7 \pm 1.1\times10^{-8}$	$1.4 \pm 2\times10^{-7}$
Ethyl cyanide	C_2H_5CN	$9.2 \pm 5.4\times10^{-8}$	$1.3 \pm 1.3\times10^{-7}$	$3.4 \pm 3.8\times10^{-7}$	$1 \pm 1.3\times10^{-7}$	$5.2 \pm 3.8\times10^{-9}$	$1.3 \pm 1.4\times10^{-7}$
Ethanol	C_2H_6O	$8.7 \pm 4.7\times10^{-8}$	$1.3 \pm 1.1\times10^{-7}$	$2.1 \pm 1.2\times10^{-7}$	$9.1 \pm 8.2\times10^{-8}$	$1.4 \pm 0.5\times10^{-7}$	$1.3 \pm 0.8\times10^{-7}$
Cyanogen	C_2N_2	$1.8 \pm 1.3\times10^{-7}$	$6.5 \pm 8\times10^{-8}$	$1.4 \pm 2.4\times10^{-7}$	$1.6 \pm 1.7\times10^{-7}$	$2.9 \pm 1.9\times10^{-8}$	$1.2 \pm 1.3\times10^{-7}$
2,3-Dimethyl-2-pentene	C_7H_{14}	$2.1 \pm 0.9\times10^{-8}$	$1.1 \pm 0.7\times10^{-7}$	$1.7 \pm 0.6\times10^{-7}$	$2.3 \pm 1.3\times10^{-7}$	$3.4 \pm 3\times10^{-9}$	$1.1 \pm 0.6\times10^{-7}$
o-xylene	C_8H_{10}	$7.8 \pm 4.3\times10^{-9}$	$4.8 \pm 3.4\times10^{-8}$	$3.5 \pm 2.5\times10^{-7}$	$7.3 \pm 5.9\times10^{-8}$	$5.5 \pm 2.2\times10^{-9}$	$9.8 \pm 7\times10^{-8}$
Formamide	CH_3NO	$1.6 \pm 1.3\times10^{-8}$	$2.3 \pm 2\times10^{-8}$	$6.8 \pm 5.4\times10^{-8}$	$2.8 \pm 2.4\times10^{-8}$	$3.4 \pm 3\times10^{-7}$	$9.6 \pm 8.3\times10^{-8}$
Dimethyl Ether	C_2H_6O	$5.8 \pm 9.6\times10^{-9}$	$1.2 \pm 1.7\times10^{-8}$	$6 \pm 6.7\times10^{-8}$	$1.5 \pm 1.9\times10^{-8}$	$3.4 \pm 3.1\times10^{-7}$	$8.6 \pm 8.5\times10^{-8}$
E,E-1,3,5-heptatriene	C_7H_{10}	$3 \pm 2.9\times10^{-8}$	$5.2 \pm 4.8\times10^{-8}$	$2.7 \pm 1.5\times10^{-7}$	$5.8 \pm 5.3\times10^{-8}$	$2 \pm 0.8\times10^{-8}$	$8.6 \pm 5.8\times10^{-8}$
Methyl Alcohol	CH_4O	$1 \pm 0.6\times10^{-7}$	$6.8 \pm 7\times10^{-8}$	$2 \pm 1.2\times10^{-7}$	$4.1 \pm 4\times10^{-8}$	$1.2 \pm 0.8\times10^{-8}$	$8.4 \pm 5.9\times10^{-8}$
Formic Acid	CH_2O_2	$9.9 \pm 5.8\times10^{-8}$	$8.8 \pm 3.7\times10^{-8}$	$5.3 \pm 3\times10^{-8}$	$8.3 \pm 3.5\times10^{-8}$	$8.1 \pm 1.5\times10^{-8}$	$8.1 \pm 3.5\times10^{-8}$
2-propynal	C_3H_2O	$8.2 \pm 6\times10^{-9}$	$4.2 \pm 6.2\times10^{-8}$	$2.6 \pm 3.3\times10^{-7}$	$5.9 \pm 8.9\times10^{-8}$	$2 \pm 1.2\times10^{-8}$	$7.8 \pm 0.1\times10^{-8}$
Hydroxy-acetaldehyde	$C_2H_4O_2$	$8.8 \pm 5.6\times10^{-8}$	$7.9 \pm 8.8\times10^{-8}$	$1.7 \pm 0.9\times10^{-7}$	$3.7 \pm 3.8\times10^{-8}$	$8.3 \pm 6.2\times10^{-9}$	$7.6 \pm 5.7\times10^{-8}$
Ethylamine	C_2H_7N	$1.8 \pm 1.1\times10^{-8}$	$2.7 \pm 2.1\times10^{-8}$	$5.4 \pm 3.7\times10^{-8}$	$3 \pm 2.3\times10^{-8}$	$2.2 \pm 1.2\times10^{-7}$	$7 \pm 4.2\times10^{-8}$
1,2-ethanediol	$C_2H_6O_2$	$4.4 \pm 3.7\times10^{-8}$	$3.6 \pm 3.6\times10^{-8}$	$1.8 \pm 1.1\times10^{-7}$	$5.3 \pm 6\times10^{-8}$	$2 \pm 1.1\times10^{-8}$	$6.6 \pm 5.2\times10^{-8}$
Propargyl alcohol	C_3H_4O	$2.3 \pm 3.3\times10^{-8}$	$7.7 \pm 9.6\times10^{-8}$	$1.4 \pm 2\times10^{-7}$	$5.2 \pm 8\times10^{-8}$	$2.5 \pm 2.4\times10^{-9}$	$5.9 \pm 8.1\times10^{-8}$
Ethyl isocyanide	C_3H_5N	$1.7 \pm 2.3\times10^{-8}$	$6.3 \pm 7.1\times10^{-8}$	$1.4 \pm 2.2\times10^{-7}$	$6.1 \pm 7.9\times10^{-8}$	$2.9 \pm 2.1\times10^{-9}$	$5.7 \pm 7.8\times10^{-8}$
trans-1,3-pentadiene	C_5H_8	$2.2 \pm 1.1\times10^{-8}$	$1.7 \pm 1.7\times10^{-8}$	$1.8 \pm 2.2\times10^{-7}$	$3.3 \pm 4.8\times10^{-8}$	$1.4 \pm 0.5\times10^{-8}$	$5.4 \pm 6.1\times10^{-8}$
Methyl Formate	$C_2H_4O_2$	$6.6 \pm 3.5\times10^{-8}$	$3.1 \pm 2.2\times10^{-8}$	$1.2 \pm 0.8\times10^{-7}$	$2.2 \pm 1.8\times10^{-8}$	$1.6 \pm 0.8\times10^{-8}$	$5 \pm 3.2\times10^{-8}$
Dimethylamine	C_2H_7N	$8.4 \pm 6.7\times10^{-9}$	$1.6 \pm 1.3\times10^{-8}$	$3.8 \pm 2.8\times10^{-8}$	$1.6 \pm 1.4\times10^{-8}$	$1.7 \pm 1.4\times10^{-7}$	$4.9 \pm 4.1\times10^{-8}$
1,3-cyclopentadiene	C_5H_6	$2.3 \pm 1\times10^{-8}$	$2.9 \pm 1.3\times10^{-8}$	$1.5 \pm 1\times10^{-7}$	$1.8 \pm 1.2\times10^{-8}$	$2 \pm 0.6\times10^{-8}$	$4.8 \pm 2.8\times10^{-8}$
Pyridine	C_5H_5N	$1.4 \pm 1.7\times10^{-8}$	$2.1 \pm 2.5\times10^{-8}$	$1.4 \pm 1.3\times10^{-7}$	$3.2 \pm 3.3\times10^{-8}$	$2.8 \pm 1.7\times10^{-9}$	$4.2 \pm 4.1\times10^{-8}$
1-buten-3-yne	C_4H_4	$3.9 \pm 2.6\times10^{-9}$	$3.6 \pm 4.4\times10^{-8}$	$8.1 \pm 9.5\times10^{-8}$	$6.9 \pm 6.8\times10^{-8}$	$1.1 \pm 0.6\times10^{-8}$	$4 \pm 4.3\times10^{-8}$

Continued on next page

98

Table 6.2 – continued from previous page

Species name	Species formula	Orbit 288	Orbit 290	Orbit 291	Orbit 292	Orbit 293	Average
Isopropyl alcohol	C_3H_8O	$3.8 \pm 4.1\times10^{-9}$	$6.6 \pm 7.2\times10^{-9}$	$2 \pm 1.5\times10^{-8}$	$7.4 \pm 7.7\times10^{-9}$	$1.5 \pm 0.7\times10^{-8}$	$3.8 \pm 2.1\times10^{-8}$
Acetic Acid	$C_2H_4O_2$	$3.8 \pm 2.6\times10^{-8}$	$4.9 \pm 2.2\times10^{-8}$	$3.9 \pm 2.5\times10^{-8}$	$2.2 \pm 1.2\times10^{-8}$	$1.9 \pm 1.1\times10^{-8}$	$3.3 \pm 1.9\times10^{-8}$
2-propenenitrile	C_3H_3N	$2.3 \pm 1.9\times10^{-8}$	$1.8 \pm 1.6\times10^{-8}$	$7.6 \pm 9.7\times10^{-8}$	$2.7 \pm 2.7\times10^{-8}$	$6.8 \pm 4.5\times10^{-9}$	$3 \pm 3.3\times10^{-8}$
Acrylonitrile	C_2H_3CN	$2.4 \pm 1.8\times10^{-8}$	$1.7 \pm 1.6\times10^{-8}$	$7.3 \pm 9.3\times10^{-8}$	$2.7 \pm 2.7\times10^{-8}$	$6.7 \pm 4.2\times10^{-9}$	$3 \pm 3.2\times10^{-8}$
Methanamine, N-methoxy-	C_2H_7NO	$9.4 \pm 5.1\times10^{-9}$	$1.3 \pm 0.5\times10^{-8}$	$1.6 \pm 0.9\times10^{-8}$	$2.3 \pm 0.7\times10^{-8}$	$8.6 \pm 2.8\times10^{-9}$	$1.4 \pm 0.6\times10^{-8}$
Methylamine, N,N-dimethyl-	C_3H_9N	$7.1 \pm 6.4\times10^{-8}$	$1 \pm 0.9\times10^{-8}$	$1.3 \pm 1.6\times10^{-8}$	$1.2 \pm 1.3\times10^{-8}$	$2.3 \pm 1.5\times10^{-9}$	$9 \pm 9.2\times10^{-9}$
1-propanol	C_3H_8O	$1.4 \pm 0.7\times10^{-8}$	$8.3 \pm 8\times10^{-9}$	$9.6 \pm 8\times10^{-9}$	$4.9 \pm 5.8\times10^{-9}$	$5.1 \pm 3\times10^{-9}$	$8.4 \pm 6.8\times10^{-9}$
Hydroxylamine, O-methyl-	CH_5NO	$2.4 \pm 1.4\times10^{-9}$	$2.9 \pm 1.3\times10^{-9}$	$1.6 \pm 1\times10^{-8}$	$2.7 \pm 1.4\times10^{-9}$	$3.6 \pm 2.7\times10^{-9}$	$5.5 \pm 3.3\times10^{-9}$
Formamide, N-methyl-	C_2H_5NO	$2.1 \pm 2\times10^{-9}$	$2.3 \pm 1.8\times10^{-9}$	$5.2 \pm 5.9\times10^{-9}$	$2 \pm 1.8\times10^{-9}$	$1.2 \pm 0.7\times10^{-9}$	$2.6 \pm 2.4\times10^{-9}$
Acetamide	C_2H_5NO	$2 \pm 1.9\times10^{-9}$	$2.4 \pm 1.8\times10^{-9}$	$5.1 \pm 5.8\times10^{-9}$	$2 \pm 1.9\times10^{-9}$	$1.1 \pm 0.7\times10^{-9}$	$2.5 \pm 2.4\times10^{-9}$
Acetaldoxime	C_2H_5NO	$2 \pm 1.8\times10^{-9}$	$2.3 \pm 1.8\times10^{-9}$	$5.2 \pm 5.8\times10^{-9}$	$2 \pm 1.9\times10^{-9}$	$1.1 \pm 0.6\times10^{-9}$	$2.5 \pm 2.4\times10^{-9}$

References

Filacchione, G., M. Ciarniello, F. Capaccioni, R. N. Clark, P. D. Nicholson, M. M. Hedman, J. N. Cuzzi, D. P. Cruikshank, C. M. Dalle Ore, R. H. Brown, et al. (2014). "Cassini–VIMS observations of Saturn's main rings: I. Spectral properties and temperature radial profiles variability with phase angle and elevation". In: *Icarus* 241, pp. 45–65.

Fitch, William L and Andrew D Sauter (1983). "Calculation of relative electron impact total ionization cross sections for organic molecules". In: *Analytical chemistry* 55.6, pp. 832–835.

Fray, N. and B. Schmitt (2009). "Sublimation of ices of astrophysical interest: A bibliographic review". In: *Planetary and Space Science* 57.14-15, pp. 2053–2080.

Hedman, M. M., J. A. Burt, J. A. Burns, and M. R. Showalter (2014). "Non-circular features in Saturn's D ring: D68". In: *Icarus* 233, pp. 147–162.

Hunter, E. P. L. and S. G. Lias (1998). "Evaluated gas phase basicities and proton affinities of molecules: an update". In: *Journal of Physical and Chemical Reference Data* 27.3, pp. 413–656.

O'Donoghue, J., L. Moore, J. E. P. Connerney, H. Melin, T. S. Stallard, S. Miller, and K. H. Baines (2017). "Redetection of the Ionospheric Signature of Saturn's 'Ring Rain'". In: *Geophysical Research Letters* 44.23, pp. 11–762.

O'Donoghue, J., T. S. Stallard, H. Melin, G. H. Jones, S. W. H. Cowley, S. Miller, K. H. Baines, and J. S. D. Blake (2013). "The domination of Saturn's low-latitude ionosphere by ring 'rain'". In: *Nature* 496.7444, p. 193.

O'Donoghue, James, Luke Moore, Jack Connerney, Henrik Melin, Tom S Stallard, Steve Miller, and Kevin H Baines (2019). "Observations of the chemical and thermal response of 'ring rain'on Saturn's ionosphere". In: *Icarus* 322, pp. 251–260.

Teolis, Ben D, HB Niemann, JH Waite, DA Gell, RS Perryman, WT Kasprzak, KE Mandt, RV Yelle, AY Lee, FJ Pelletier, et al. (2015). "A revised sensitivity

model for Cassini INMS: Results at Titan". In: *Space Science Reviews* 190.1, pp. 47–84.

Tiscareno, M. S., P. D. Nicholson, J. N. Cuzzi, L. J. Spilker, C. D. Murray, M. M. Hedman, J. E. Colwell, J. A. Burns, S. M. Brooks, R. N. Clark, et al. (2019). "Close-range remote sensing of Saturn's rings during Cassini's ring-grazing orbits and Grand Finale". In: *Science* 364.6445, eaau1017.

Waite, J. H., R. S. Perryman, M. E. Perry, K. E. Miller, J. Bell, T. E. Cravens, C. R. Glein, J. Grimes, M. Hedman, J. Cuzzi, et al. (2018). "Chemical interactions between Saturn's atmosphere and its rings". In: *Science* 362.6410, eaat2382.

Chapter 7

Diffusion of ring material into Saturn's atmosphere

To quantify the influx of material from the rings, we use a 1-D model to understand the exospheric temperature and external flux into the upper atmosphere. This model was first detailed in Yelle et al. (2018), where we use the model to provide a detailed analysis of the He and CH_4 distribution in Saturn's upper atmosphere and to demonstrate that CH_4 must be inflowing into the atmosphere from Saturn's rings. We also utilize this model to determine the influx of many other species into Saturn's atmosphere from the rings, as described below.

7.1 Temperature profile

We first focus on measurements from atmospheric entry, which probed deeper into Saturn's atmosphere than the other orbits and was the only set of measurements that detected an increase in temperature in the thermosphere. In order

to properly analyze the density profiles, we adopt a thermospheric tempera-
ture profile similar to the classical Bates profile (Bates, 1951) and modify the
vertical coordinate into units of gravitational potential. Thus, the temperature
profile can be expressed as

$$T(\phi) = T_\infty \left(1 - ae^{-\tau x}\right) \tag{7.1}$$

with

$$x = \frac{\phi - \phi_\circ}{RT_\infty}$$

$$a = 1 - \frac{T_\circ}{T_\infty} \tag{7.2}$$

$$\tau = \frac{RT_\infty}{T_\infty - T_\circ} \left.\frac{dT}{d\phi}\right|_\circ$$

where ϕ_o is the gravitational potential at the reference surface, $T_\circ$ is the temper-
ature on that surface, T_∞ is the asymptotic temperature at high altitudes, and
R is the gas constant for H_2. Adopting this temperature profile and integrating
the hydrostatic equilibrium equation along the direction of gravity gives

$$p_a(\phi) = p_a(\phi_\circ) \exp\left(x + \frac{1}{\tau}\ln\left(\frac{1 - ae^{-\tau x}}{1 - a}\right)\right) \tag{7.3}$$

with density, N_a, and temperature, T, related to pressure, p_a, through the ideal
gas law

$$p_a = N_a k_b T \tag{7.4}$$

where k_b is Boltzmann's constant.

The best fit temperature profile and the match to the H_2 density profile
are shown in Figure 7.1. These results were originally published in Yelle
et al. (2018) and the temperature profile is used throughout the rest of this

analysis. The asymptotic temperature in the upper atmosphere is T_∞ = 354 K, while the pressure and temperature at the base of the measurements are p = 1.2 × 10^{-4} Pa and T_o = 298 K, respectively. The temperature gradient at the base of the atmosphere is given by dT/ds = $(dT/d\phi)g$ = 0.4 K/km, where s is the distance in the direction normal to surfaces of constant ϕ. The thermal conduction flux associated with this gradient is -7.3 × 10^{-5} W/m². This is roughly consistent with the results of Koskinen et al. (2015) who find thermal conduction fluxes from 5 × 10^{-5} to 12 × 10^{-5} W/m² from analysis of Cassini UltraViolet Imaging Spectrometer (UVIS) occultation measurements of Saturn's thermosphere.

The other orbits analyzed in this work probe higher in the atmosphere and we determine the temperature by fitting an isothermal model to the H_2 density profiles. We determine the isothermal temperature using measurements taken between ϕ of 6.69 and 6.61 × 10^8 J kg^{-1}, where the atmosphere appears to be isothermal and the quality of the measurements is high. Results for the isothermal temperature for each orbit can be found in Table 7.1. Uncertainties associated with these temperature values are 1σ values from the fit, based on the assumption of isothermality. As the local times and latitudes are similar for these orbits, the variability in temperature among these orbits may be with longitude or may be secular. These temperatures are consistent with values determined from ultraviolet occultation measurements as reported in Koskinen et al. (2013), Koskinen et al. (2015), and Koskinen and Guerlet (2018). For example, Koskinen et al. (2013) reported upper thermospheric temperatures that ranged from 373 ± 20 K to 534 ± 15 K with the coldest
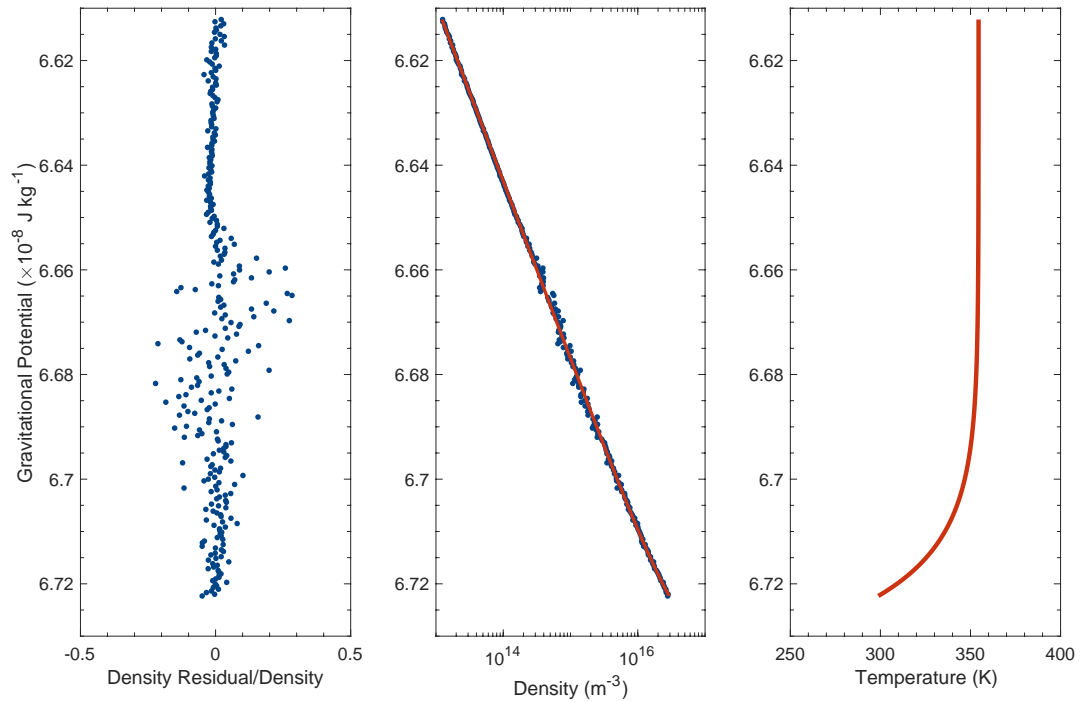
Figure 7.1: Model temperature profile fit to the INMS H_2 data from atmospheric entry. Left panel: The residuals from the fit. Middle panel: The measured densities (blue data points) and the model fit in red. Right panel: The model temperature profile. These results were originally published in Yelle et al. (2018) and the model temperature profile is used throughout the rest of this analysis.

values near the equator. The values derived here for the equatorial region range from 340 to 372 K and are thus consistent within uncertainties. We note that our values are much lower than the 612 K found by Shemansky and Liu (2012) from a stellar occultation at 3.6°S but are consistent with the reanalysis of these data by Koskinen et al. (2015).

7.2 1-D diffusion model

To determine the influx of material from the rings into Saturn we assume that the distribution of minor constituents is governed by the diffusion equation

$$\vec{F}_i = -D_i N_i \left(\vec{\nabla} \ln (p_i) + \frac{m_i}{k_b T} \vec{\nabla} \phi \right) - K N_i \left(\vec{\nabla} \ln (p_i) + \frac{m_a}{k_b T} \vec{\nabla} \phi \right) \qquad (7.5)$$

where $\vec{F}_i$ is the flux of the ith constituent, p_i is its partial pressure, N_i is its density, and m_i is its mass. The first term on the RHS of Equation 7.5 follows from Equation 8.3.12 in Chapman and Cowling (1970), assuming hydrostatic equilibrium for the atmosphere and that the diffusing species is a minor constituent of the atmosphere. Following Colegrove, Johnson, and Hanson (1966) we include the eddy term (second term on the RHS) by replacing the diffusion coefficient, D_i, with an eddy diffusion coefficient, K, and replacing m_i by the mean atmospheric mass, m_a. We assume that the atmosphere is uniform on constant potential surfaces, therefore the only non-zero component of the gradients and the flux are in the direction of gravity, perpendicular to constant potential surfaces. This leads to

$$F_i = -(D_i + K) \frac{d \left(\ln (X_i) \right)}{d\phi} g - D_i \frac{m_i - m_a}{k_b T} g \qquad (7.6)$$

where g is the magnitude of the gravitational acceleration. A species native to the atmosphere with no presence in the rings, such as He, should have a negligible external downward flux. Thus, the measurements of He should be able to be fit with $F_i = 0$ and Equation 7.6 then has the solution

$$X_i(\phi) = X_i(\phi_\circ) \exp \int_{\phi_\circ}^{\phi} \frac{D_i}{D_i + K} \frac{m_i - m_a}{kT(\phi')} d\phi' \qquad (7.7)$$

For an exogenous species falling into the atmosphere with a non-zero external flux, we rewrite Equation 7.6 as

$$\frac{dX_i}{d\phi} + \frac{D_i}{D_i + K}\frac{m_i - m_a}{k_b T}X_i = -\frac{F_i}{g N_a (D_i + K)} \tag{7.8}$$

which has the solution:

$$X_i(\phi) = X_i(\phi_\circ)\exp\int_{\phi_\circ}^{\phi} d\phi' \frac{D_i}{D_i + K}\frac{m_i - m_a}{RT}$$

$$-\int_{\phi_\circ}^{\phi} d\phi' \frac{F_i}{g N_a (D_i + K)}\exp\left(\int_{\phi_\circ}^{\phi} d\phi'' \frac{D_i}{D_i + K}\frac{m_i - m_a}{RT}\right) \tag{7.9}$$

We use this equation to describe the distribution of exogenous material into Saturn's atmosphere using the results from our mass spectral deconvolution and adopt an eddy diffusion profile of the form

$$\log(K(p)) = \frac{1}{2}\log\left(K_\infty/K_\circ\right)\tanh\left(\gamma\log\left(p_\circ/p\right)\right) + \frac{1}{2}\log\left(K_\circ K_\infty\right) \tag{7.10}$$

where $K_\circ$ is the asymptotic value at high pressure, K_∞ is the asymptotic value at low pressure, and γ determines rate of transition from $K_\circ$ to K_∞. Molecular diffusion coefficients, D_i, for He and CH_4 in H_2 are taken from Mason and Marrero (1970). Molecular diffusion coefficients for other species are described in Section 7.2.2.

Figure 7.2 shows an example of the results from our model for He and CH_4 during atmospheric entry. As measurements of CH_4 exist deeper down in Saturn's atmosphere, we can attempt to connect our observations of CH_4 with INMS to the fully mixed deeper atmosphere below. We adopt mole fractions of He and CH_4 in the deep atmosphere ($X_i(\phi_\circ)$) of 0.11 and 4.6 $\times$

10^{-4}, respectively (Koskinen and Guerlet, 2018). We use the results from Koskinen and Guerlet (2018), who combined limb profiles of the middle atmosphere for the Cassini Composite Infrared Spectrometer (CIRS) with UVIS occultation measurements of the thermosphere and we adopt their model ST14M10D03S7 as it is most consistent with our measurements of the equatorial region. The INMS measurements span pressures from 6×10^{-8} to 1.2×10^{-4} Pa. We use the Koskinen and Guerlet (2018) model at pressures greater than 10^{-3} Pa and assume that the temperature varies linearly with gravitational potential for the region between 1.2×10^{-4} and 10^{-3} Pa. More sophisticated approaches are possible, but the algorithm used here produces a relatively smooth temperature profile that is adequate for modeling diffusive separation in the atmosphere. The resulting temperature profile is shown in black in the left panel of Figure 7.2.

As expected, He measurements can be fit by a model with no external flux ($F_i = 0$) into the atmosphere. Since these measurements are taken well above Saturn's homopause, we are not able to uniquely constrain K in this analysis. We use $K_\circ = 30$ m^2/s, $K_\infty = 1.4 \times 10^4$ m^2/s, and $\gamma = 0.6$ for the results presented here, however a wide variety of K profiles can be used to fit the data. Our intention here is not to precisely determine the eddy diffusion profile or constrain the deep atmosphere mole fraction of He (or other species), but to show that the He distribution is consistent with a simple diffusion model with no external flux into the atmosphere while the distribution of other species detected in our analysis can only be explained with an external source supplying Saturn's upper atmosphere.
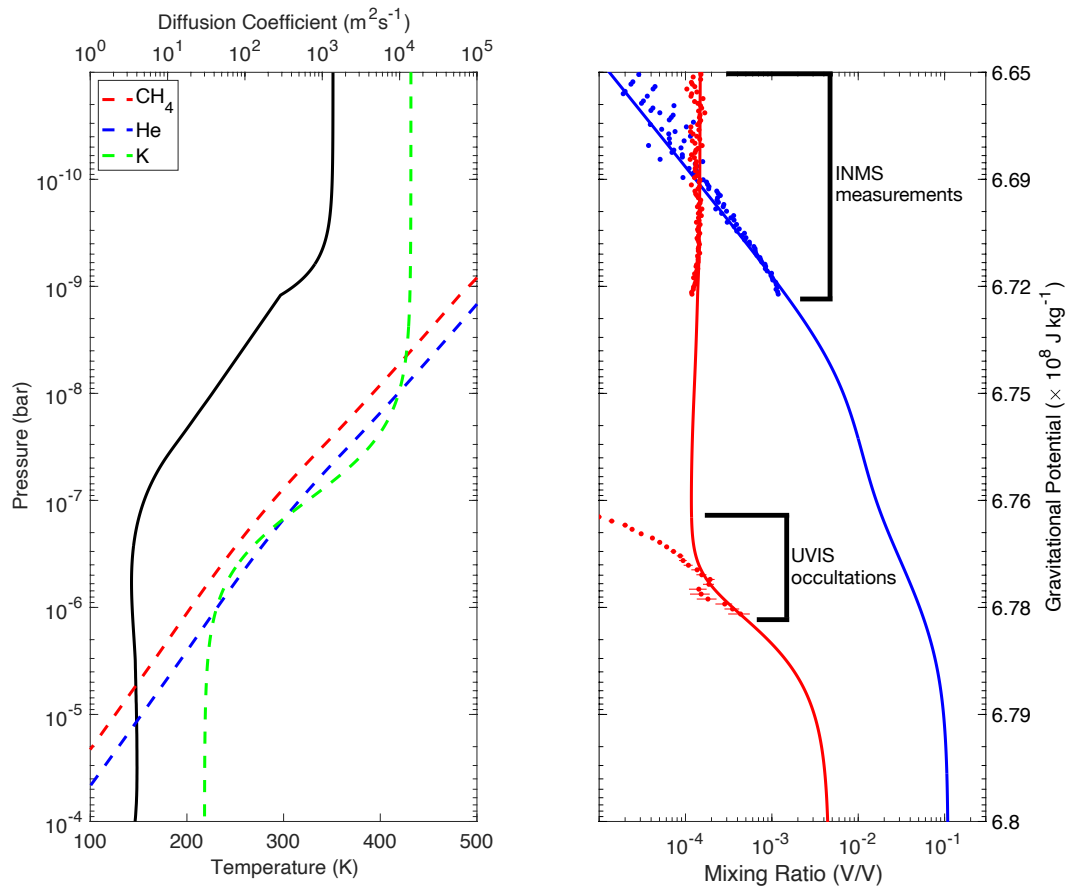
Figure 7.2: Results of our 1-D diffusion model for He (blue) and CH_4 (red). Left panel: The solid black curve shows the temperature profile, while the dashed curves show the eddy diffusion coefficient (green) and molecular diffusion coefficients for He and CH4 for our model atmosphere. Right panel: Comparison of our 1-D diffusion model with INMS data from atmospheric entry (orbit 293) and UVIS occultation data at a similar latitude (Koskinen and Guerlet, 2018). These results were originally published in Yelle et al. (2018).

Results from our modeling efforts confirm that the distribution of He in the upper atmosphere, at pressures less than 10^{-2} Pa, is dominated by molecular diffusion. This implies that the internal CH_4 on Saturn should be confined to deep pressures, consistent with the diffusive separation seen also in the occultation results. This further confirms that the CH_4 detected in the upper atmosphere by INMS must have an external source. The altitude profile of CH_4 is consistent with this, as the downward flux of a heavy constituent should have a roughly constant mole fraction (Connerney and Waite, 1984). Our best fitting model returns a downward flux for CH_4 of $F_i = 1.2 \times 10^{13}$ $\mathrm{m}^{-2}\mathrm{s}^{-1}$. These results provide a good match to the INMS measurements, however CH_4 results from UVIS occultations between 0.01 and 0.1 Pa are not accurately fit. This is likely due to the simplicity of using a 1-D model in an attempt to understand a very complicated system. The CH_4 distribution likely varies latitudinally and spreads out as it diffuses downward through the atmosphere, which is not captured in our model and which would modify our results to be more in agreement with the occultation measurements. Further work is needed to understand the transport of the material from the rings to Saturn in a 2-D or 3-D sense, which is beyond the scope of this work.

7.2.1 Isothermal approximation

All orbits analyzed here aside from atmospheric entry recorded measurements in the isothermal, diffusively separated region of the atmosphere. In this region, equation 7.9 has the approximate solution

$$X_i \sim \frac{H_i F_i}{N_a D_i} \tag{7.11}$$

The product $N_a D_i$ is constant because D_i varies as the inverse of atmospheric number density. Thus, X_i is constant if F_i is constant. Diffusion times in the upper thermosphere are much faster than chemical loss times, so F_i should be constant. We can use Equation 7.11, along with mixing ratio results from our mass spectral deconvolution, to estimate F_i for all exogenous species. Since the molecular diffusion of a species in H_2, D_i, is not always available in the literature, we calculate this parameter using the theoretical approach based on the Lennard-Jones potential found in Hirschfelder et al. (1954) and detailed in the following subsection.

7.2.2 Molecular diffusion coefficient

The molecular diffusion coefficient, D_i, is species specific and is calculated using the theoretical approach based on the Lennard-Jones potential found in Hirschfelder et al. (1954):

$$D_{12} = 0.0026280 \frac{\sqrt{T^3(M_1 + M_2)/2M_1M2}}{p\sigma_{12}^2 \Omega_{12}^{(1,1)}(T_{12}^*)} \tag{7.12}$$

where T is the temperature, M_1 and M_2 are the molecular weights of H_2 and the diffusing species, p is the pressure, σ_{12} is the Lennard-Jones parameter that quantifies the binary collision diameter, $\Omega_{12}^{(1,1)}$ is the collision integral used for calculating the transport coefficient for the Lennard-Jones (6-12) potential, and T_{12}^* is the reduced temperature equivalent to $k_B T/\epsilon_{12}$. In the reduced temperature calculation, ϵ_{12}/k_B is another Lennard-Jones parameter quantifying the energy involved with the interaction. The integral $\Omega_{12}^{(1,1)}$ is taken from Hirschfelder et al. (1954) and the Lennard-Jones parameters for

species are taken from Bird, Stewart, and Lightfoot (2006). Results from this calculation are plotted in Figure 7.3 for species in H_2. The average of all species in this figure is used for many minor species in the database since the necessary parameters are not always available in the literature.
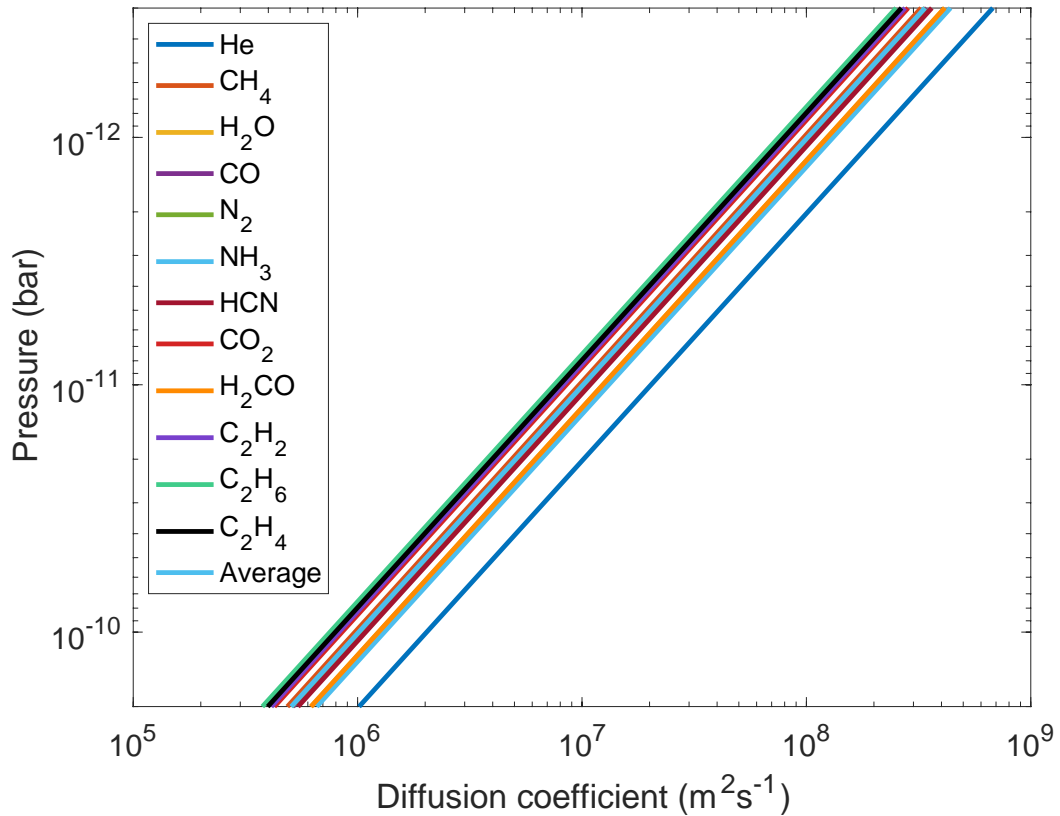
Figure 7.3: Molecular diffusion coefficients for the most abundant species in our spectral fits. The average of all species is used for many minor species since the necessary parameters are not always available in the literature.

7.3 Diffusion results

Using the model described above, we determine the downward flux for all of the major species found in Figure 6.1. We again use the region of Saturn

where all orbits have data, from ϕ of 6.69 to 6.66 $\times 10^8$ J kg^{-1}. In this region mixing ratios of external species are constant, leading to a constant downward flux. HD and He, which are native to Saturn and should have no external flux, are able to be fit with a downward flux of 0 m^{-2}s^{-1}, as expected. All other major species are fit with a downward flux on the order of 10^{12} to 10^{13} m^{-2}s^{-1}. These results can be found in Table 7.1. The remaining minor species in the database constitute a much lower signal than the previously discussed species, representing an average combined mixing ratio of only 6.3 $\times 10^{-5}$. The flux of these species, along with the mass deposition rates discussed below, are calculated for each species separately and are reported here as combined values. Since the parameters needed to determine the theoretical molecular diffusion coefficient are not always available in the literature, the molecular diffusion coefficient we use for the combined influx calculation of minor species is the average diffusion coefficient used for the major species. Since the molecular diffusion coefficient does not vary widely among the major species, this is an appropriate approximation when the needed parameters are not available.

Table 7.1: Temperature, flux, and mass deposition rate results.

Orbit Number	Temperature (K)	Species	Flux ($\times 10^{12}$ m^{-2}s^{-1})	Mass Deposition Rate ($\times 10^2$ kg s^{-1})
288	368.8 $\pm$ 1.1	CO	15 $\pm$ 3.9	47 $\pm$ 12
		N_2	14 $\pm$ 3.1	44 $\pm$ 1.0
		H_2O	9.2 $\pm$ 2.6	18 $\pm$ 5.3
		CH_4	9.3 $\pm$ 1.7	16 $\pm$ 3.1
		CO_2	3.9 $\pm$ 1.6	19 $\pm$ 7.6
		HCN	2.7 $\pm$ 1.3	8.0 $\pm$ 3.8
		H_2CO	1.7 $\pm$ 1.0	5.8 $\pm$ 3.5
				Continued on next page

Table 7.1 – continued from previous page

Orbit Number	Temperature (K)	Species	Flux ($\times\ 10^{12}\ \mathrm{m^{-2}s^{-1}}$)	Mass Deposition Rate ($\times\ 10^{2}\ \mathrm{kg\ s^{-1}}$)
		NH_3	2.9 ± 1.0	5.4 ± 1.9
		C_2H_6	1.1 ± 0.6	3.8 ± 2.1
		C_2H_4	1.1 ± 0.7	3.4 ± 2.1
		C_2H_2	0.9 ± 0.4	2.5 ± 1.2
		Remaining	7.0 ± 1.2	44 ± 6.9
		Total	69 ± 6.5	218 ± 21
290	363.7 ± 1.0	CO	21 ± 7.1	67 ± 22
		N_2	18 ± 5.5	58 ± 17
		H_2O	26 ± 7.9	53 ± 16
		CH_4	17 ± 3.4	30 ± 6.1
		CO_2	3.8 ± 2.0	19 ± 9.7
		HCN	5.1 ± 2.6	16 ± 7.7
		H_2CO	4.4 ± 2.3	15 ± 7.6
		NH_3	7.1 ± 2.6	13 ± 5.0
		C_2H_6	1.7 ± 1.3	5.8 ± 4.4
		C_2H_4	1.7 ± 1.2	5.4 ± 3.9
		C_2H_2	1.8 ± 0.8	5.1 ± 2.4
		Remaining	18 ± 2.8	120 ± 19
		Total	126 ± 14	406 ± 41
291	339.6 ± 1.2	CO	32 ± 11	100 ± 35
		N_2	28 ± 8.5	88 ± 26
		H_2O	61 ± 12	120 ± 25
		CH_4	23 ± 5.0	41 ± 8.9
		CO_2	7.4 ± 3.2	36 ± 16
		HCN	9.7 ± 4.4	29 ± 13
		H_2CO	5.2 ± 3.1	17 ± 10
		NH_3	23 ± 6.9	45 ± 13
		C_2H_6	3.0 ± 2.1	10 ± 7.2
		C_2H_4	3.1 ± 2.1	9.6 ± 6.5
		C_2H_2	3.2 ± 1.3	9.3 ± 3.9
		Remaining	33 ± 4.1	231 ± 27
		Total	233 ± 22	741 ± 65
292	372.1 ± 1.0	CO	22 ± 8.0	68 ± 25
		N_2	20 ± 6.2	61 ± 19

Table 7.1 – continued from previous page

Orbit Number	Temperature (K)	Species	Flux ($\times 10^{12}$ m^{-2}s^{-1})	Mass Deposition Rate ($\times 10^2$ kg s^{-1})
		H_2O	14 ± 4.1	28 ± 8.2
		CH_4	19 ± 3.7	34 ± 6.6
		CO_2	3.2 ± 1.9	16 ± 9.4
		HCN	6.5 ± 3.0	20 ± 9.1
		H_2CO	5.9 ± 2.9	20 ± 9.6
		NH_3	8.0 ± 2.5	15 ± 4.8
		C_2H_6	2.3 ± 1.7	7.7 ± 5.8
		C_2H_4	1.7 ± 1.3	5.3 ± 3.9
		C_2H_2	2.1 ± 0.9	6.2 ± 2.6
		Remaining	21 ± 3.3	142 ± 22
		Total	125 ± 13	423 ± 44
293	351.1 ± 1.2	CO	23 ± 6.2	72 ± 19
		N_2	21 ± 5.5	66 ± 17
		H_2O	2.3 ± 0.7	4.6 ± 1.5
		CH_4	15 ± 3.2	26 ± 5.6
		CO_2	1.8 ± 1.1	9.0 ± 5.2
		HCN	3.6 ± 1.5	11 ± 4.5
		H_2CO	0.9 ± 1.0	2.9 ± 3.3
		NH_3	0.8 ± 0.5	1.5 ± 0.9
		C_2H_6	1.1 ± 0.7	3.8 ± 2.2
		C_2H_4	0.9 ± 0.7	2.7 ± 2.1
		C_2H_2	1.5 ± 0.5	4.2 ± 1.5
		Remaining	9.0 ± 3.1	50 ± 16
		Total	81 ± 9.7	254 ± 32

Note. The "Remaining" value represents the results of the remaining minor species in the database which constitute a much lower signal than the previously reported species and are reported here as combined flux and MDR values.

Our total influx results range from 6.9×10^{13} to 2.3×10^{14} m^{-2}s^{-1}, which is a considerable and unsustainable amount of material from the rings. We quantify the amount of material being deposited into the atmosphere from the rings by converting these flux values into mass deposition rates. We

approximate the mass deposition rate (MDR) using the equation:

$$MDR = F_i m_i \times 2\pi r_{Saturn}^2 \theta, \qquad (7.13)$$

where F_i is the flux of molecule i, m_i is the molecular mass of molecule i, and θ represents the latitudinal width for the influx region. We choose a latitudinal width of $\pm 8°$ from the ring plane, which corresponds to the region where most of the major constituents are above the noise level. It is possible that the latitudinal extent is broader than this, however we do not have sufficient signal further from the ring plane to determine this. Results from this calculation are also found in Table 7.1.

We calculate a total mass deposition rate on the order of 10^4 kg/s, with results ranging from 2.2 to 7.4 $\times 10^4$ kg/s. Since this calculation depends on the mass of individual molecules entering the atmosphere, it's worth noting that species with the highest mixing ratios are not necessarily the species that contribute the most to this mass calculation. On average, CO and N_2 provide the largest contribution by mass to these results, followed by H_2O, CH_4, and CO_2. Results of the total mass contribution are similar to previous estimates from Waite et al. (2018) (0.5 to 4.5 $\times 10^4$ kg/s) and Perry et al. (2018) (1 to 20 $\times 10^4$ kg/s), though it should be noted that Perry et al. (2018) only report a value for orbit 290. Slight differences in these results are not surprising given that this is a completely independent analysis using different methods. Waite et al. (2018) determine a downward diffusion velocity based on a limiting flux equation (and alternatively by using a hydrostatic model to determine diffusion coefficients) and calculate a mass influx based on an $8°$ latitudinal

width for the influxing region. Perry et al. (2018) use a latitudinal width of $20°$ and determine the diffusion velocity of an infalling molecule by assuming the material entering Saturn's atmosphere is settling in the Epstein regime by viscous drag which allows them to calculate the diffusion velocity as the terminal velocity. Regardless of differences in calculating these values, all independent analyses of this data set have arrived at the conclusion that the amount of influx from the rings is surprisingly large and unsustainable over a long period of time.

Recent gravity measurements from the Grand Finale orbits estimate the total mass of the rings to be $1.54 \pm 0.49 \times 10^{19}$ kg (Iess et al. (2019)). If we use very straightforward assumptions that the rings are able to spread over time (via viscous spreading, satellite interactions, and micrometeoritic bombardment) and continuously feed the influx of material into the atmosphere, that our influx values are constant over time, and that there are no other sources replenishing the rings, then our mass deposition results suggest that the entire ring system could be depleted in just tens of millions of years. More realistically, viscous spreading throughout the rings is not effective enough to deplete the entirety of the ring system (Salmon et al., 2010). The bulk of this infalling material is coming from Saturn's diffuse innermost D ring, which could result in an extremely short lifetime for the D ring, which may be fed by the C ring, and no notable effects for the more massive rings that are located further from the planet. Although the total mass of the rings is well constrained, individual ring masses are not as well determined due to the correlations among the rings. Iess et al. (2019) estimate the C ring to be approximately 0.024 Mimas

masses, which agrees with previous estimates from UVIS stellar occultations (Baillié et al. (2011)). The D ring is assumed to be no more than 1% of the total mass of the C ring (Waite et al. (2018)), bringing the estimated mass of the D ring to 9×10^{15} kg and the combined mass of the C and D rings to 9.09×10^{17} kg. If the mass deposition rate determined by INMS measurements is a constant source of influx into Saturn's atmosphere, the entire D ring would be depleted in a matter of thousands of years. It's likely that the C ring supplies material to the D ring over time via viscous spreading or other energetic events that perturb the rings. Assuming this is an efficient process, the combined C and D rings would only last on the order of 10^5 to 10^6 years. Our assumptions here are straightforward and assume that all material in these rings would act in a similar manner to the material detected by INMS, which we know is not the case. It's likely that our simplified timescale calculations are more of a lower limit, however a more elaborate analysis of ring dynamics as related to mass loss into Saturn is beyond the scope of this work. The lifetimes we report here are extremely small on planetary timescales and combined with recent estimates of the age of the rings (≤ 150 Myr (Zhang et al. (2017)) suggest that deposition of large amounts of ring material reported here is likely not representative of the typical influx over the lifetime of the ring system. This further suggests that the massive influx is likely a transient phenomenon that could be a consequence of recent perturbations in this region, such as the D68 disturbance noted in Hedman et al. (2014).

References

Baillié, Kévin, Joshua E Colwell, Jack J Lissauer, Larry W Esposito, and Miodrag Sremčević (2011). "Waves in Cassini UVIS stellar occultations: 2. The C ring". In: *Icarus* 216.1, pp. 292–308.

Bates, D. R. (1951). "The temperature of the upper atmosphere". In: *Proceedings of the Physical Society. Section B* 64.9, p. 805.

Bird, R Byron, Warren E Stewart, and Edwin N Lightfoot (2006). *Transport Phenomena*. Vol. 1. John Wiley & Sons.

Chapman, Sydney and TG Cowling (1970). "The Mathematical Theory of Non-uniform Gases: An Account of the Kinetic Theory of Viscosity, Thermal Conduction and Diffusion in Gases". In:

Colegrove, FD, FS Johnson, and WB Hanson (1966). "Atmospheric composition in the lower thermosphere". In: *Journal of Geophysical Research* 71.9, pp. 2227–2236.

Connerney, J. E. P. and J. H. Waite (1984). "New model of Saturn's ionosphere with an influx of water from the rings". In: *Nature* 312.5990, p. 136.

Hedman, M. M., J. A. Burt, J. A. Burns, and M. R. Showalter (2014). "Non-circular features in Saturn's D ring: D68". In: *Icarus* 233, pp. 147–162.

Hirschfelder, J. O., C. F. Curtiss, R. B. Bird, and M. G. Mayer (1954). *Molecular theory of gases and liquids*. Vol. 26. Wiley New York.

Iess, L., B. Militzer, Y. Kaspi, P. Nicholson, D. Durante, P. Racioppa, A. Anabtawi, E. Galanti, W. Hubbard, M. J. Mariani, et al. (2019). "Measurement and implications of Saturn's gravity field and ring mass". In: *Science* 364.6445, eaat2965.

Koskinen, T. T. and S. Guerlet (2018). "Atmospheric structure and helium abundance on Saturn from Cassini/UVIS and CIRS observations". In: *Icarus* 307, pp. 161–171.

Koskinen, T. T., B. R. Sandel, R. V. Yelle, D. F. Strobel, I. C. F. Müller-Wodarg, and J. T. Erwin (2015). "Saturn's variable thermosphere from Cassini/UVIS occultations". In: *Icarus* 260, pp. 174–189.

Koskinen, T. T., B. R. Sandel, R. V. Yelle, F. J. Capalbo, G. M. Holsclaw, W. E. McClintock, and S. Edgington (2013). "The density and temperature structure near the exobase of Saturn from Cassini UVIS solar occultations". In: *Icarus* 226.2, pp. 1318–1330.

Mason, E. A. and T. R. Marrero (1970). "The diffusion of atoms and molecules". In: *Advances in Atomic and Molecular Physics*. Vol. 6. Elsevier, pp. 155–232.

Perry, M. E., J. H. Waite, D. G. Mitchell, K. E. Miller, T. E. Cravens, R. S. Perryman, L. Moore, R. V. Yelle, H-W Hsu, M. M. Hedman, et al. (2018). "Material flux from the rings of Saturn into its atmosphere". In: *Geophysical Research Letters* 45.19, pp. 10–093.

Salmon, J., S. Charnoz, A. Crida, and A. Brahic (2010). "Long-term and large-scale viscous evolution of dense planetary rings". In: *Icarus* 209.2, pp. 771–785.

Shemansky, D. E. and X. Liu (2012). "Saturn upper atmospheric structure from Cassini EUV and FUV occultations". In: *Canadian Journal of Physics* 90.8, pp. 817–831.

Waite, J. H., R. S. Perryman, M. E. Perry, K. E. Miller, J. Bell, T. E. Cravens, C. R. Glein, J. Grimes, M. Hedman, J. Cuzzi, et al. (2018). "Chemical interactions between Saturn's atmosphere and its rings". In: *Science* 362.6410, eaat2382.

Yelle, R. V., J. Serigano, T. T. Koskinen, S. M. Hörst, M. E. Perry, R. S. Perryman, and J. H. Waite (2018). "Thermal structure and composition of Saturn's upper atmosphere from Cassini/Ion Neutral Mass Spectrometer measurements". In: *Geophysical Research Letters* 45.20, pp. 10–951.

Zhang, Z, AG Hayes, MA Janssen, PD Nicholson, JN Cuzzi, I de Pater, and DE Dunn (2017). "Exposure age of Saturn's A and B rings, and the Cassini Division as suggested by their non-icy material content". In: *Icarus* 294, pp. 14–42.

Chapter 8

Discussion and Conclusions

The surprisingly complex measurements returned by INMS provide us with the unique opportunity to measure the composition of the rings and upper-most atmosphere of Saturn and understand the impact of ring-atmosphere coupling like never before. This thesis provides an in-depth analysis of the composition and distribution of neutral gas near Saturn's equatorial ring plane using in situ measurements returned from the Ion and Neutral Mass Spectrometer during Cassini's last few Grand Finale orbits. The unique trajectories of these orbits allowed for the first in situ measurements of this region with INMS returning rich spectra full of components native to Saturn (H_2, HD, He) as well as an unexpectedly large amount of ices and higher mass organics likely originating from the rings and falling into the atmosphere. The sections below briefly summarize the content of this thesis. Future photochemical modeling of this region utilizing the results presented here is crucial in understanding the processes at play in this unique, interconnected region of our solar system. The surprisingly complex composition found in Saturn's upper thermosphere could have implications for the radiative balance and dynamics of the region,

and even cloud and haze production as these molecules could ultimately serve as cloud condensation nuclei. Without Cassini's presence in the Saturn system, future in situ measurements of this region may be decades away. We must rely on ground and space based observatories, such as ALMA and JWST with their unprecedented spectral and spatial resolution, to help illuminate the many outstanding questions pertaining to Saturn's ring-atmosphere coupling.

8.1 Observations and data reduction

In this thesis we analyze the signal from the entire mass range returned by INMS for Cassini orbits 288, 290, 291, 292, and 293. The instrument, observations, and methods to calibrate and correct the raw data can be found in Chapters 2 and 3. All orbits aside from atmospheric entry (orbit 293) measure Saturn at closest approach at a similar latitude and local solar time. While these orbits approached Saturn near $5°$ S and around noon LST, measurements during atmospheric entry occurred around $9°$ N and approximately an hour earlier than other orbits. All mass spectra from these orbits have a similar general trend, with signal attributed to native Saturn species, volatile ices, and higher mass organics. Orbit 291 returned a higher signal and included more exogenous material than other orbits while orbit 293 was depleted in many exogenous species, namely H_2O and NH_3. It's possible that the differences in composition observed for orbit 293 are a consequence of the spacecraft entering Saturn's atmosphere before crossing the equatorial ring plane, where we assume the majority of exogenous ring material is located. Compositional differences among the other orbits are likely due to general dynamical and

temporal fluctuations associated with this tenuous region.

The instrument's excellent performance throughout the spacecraft's 13 years in orbit allowed for an extensive amount of studies that drastically improved our understanding of the composition of regions throughout the Saturn system. Thus, a detailed understanding of the instrument and how it functions under the varying conditions of the Saturn system has existed for some time. We perform corrections and calibrations to the raw data returned from the spacecraft in order to handle these various instrumental effects. These include corrections for background subtraction and dead time correction for detector fatigue, calibration sensitivity, and ram pressure enhancement, which are detailed in Chapter 3. Many of these effects have been detailed before for the analysis of measurements returned during Titan flybys (Cui et al., 2009a; Cui et al., 2012) and we utilize these corrections here when applicable. Corrections for the saturation of the primary detector in mass channel 2 as well as corrections for wall adsorption within the instrument have been re-characterized for Saturn conditions in this thesis. Due to wall adsorption effects within the instrument, we focus the entirety of our analysis on only inbound measurements as these measurements are not as affected by desorption in the instrument at a later time.

8.2 Mass spectral deconvolution

Deconvolving a unit resolution mass spectrum in order to identify and quantify the constituents present in the signal is a degenerate process since fragments from different species overlap and contribute to the same mass channels.

This is further complicated by the fact that INMS calibration data do not exist for all species of interest and measurements from the standard NIST mass spectral library are not an identical substitute for INMS calibration values. We create a database that is composed of native Saturn species, volatile ices, and organics, which are chosen based on our understanding of diffuse environments of the outer solar system. After creating a database of 80 species to fit the mass spectra that is a combination of INMS and NIST calibration values, we adopt a mass spectral deconvolution tool that uses Monte Carlo randomization to vary the peak intensities of each fragment in order to fit the measurements (Gautier et al. (2020)). This method allows us to generate thousands of simulated databases to model the INMS measurements. We allow fragmentation peak intensities to vary by $\pm30\%$, although intensities rarely exceed $\pm15\%$ in our best fitting simulations. We use an interior-point least-square method that is suitable for large matrices such as the mass spectra we analyze here, save 500,000 simulations that meet a residual fitting threshold, and analyze the top 10% (50,000) of these simulations based on the minimal residuals to the data.

INMS returned spectra from Saturn with a very large range of signal spanning seven orders of magnitude, which complicates residual best fits since mass channels with higher signal dominate the resulting residual. To handle this, we separate the spectra into three different sections and fit each section individually. These sections include (1) the high mass, low signal region (m/z 31 to 36 amu, 46 to 100 amu), (2) the low mass, high signal region (m/z 3 to 30 amu, 37 to 45 amu), and (3) H_2, which has a much higher signal

than any other mass channels. We perform this deconvolution for an averaged mass spectrum of each orbit in order to directly compare results, as well as spectra divided into ϕ bins of $0.01 \times 10^8 \, \text{J kg}^{-1}$ in order to retrieve mixing ratio and density profiles of all major species. An explanation of the mass spectral deconvolution algorithm and the results of our best fitting simulations can be found in Chapters 4 and 5.

8.3 Compositional results

We use the results from our mass spectral deconvolution to determine the atmospheric mixing ratio and density profiles of species included in the database as detailed in Chapter 6. We determine an average mixing ratio for all species using the averaged mass spectrum from each orbit. We determine mixing ratio and density profiles of the major species in our spectral fits. Our best-fitting models attribute much of the signal at lower masses to native Saturn species (H_2, HD, and He) and volatile ices, namely CH_4, NH_3, H_2O, CO, N_2, and CO_2, and the bulk of the higher mass signal to organics. These measurements are taken well above Saturn's homopause and native Saturn species behave as expected for constituents in diffusive separation above an atmosphere's homopause. On the other hand, the density profiles of all other species track that of H_2, suggesting this material comes from an external source which must be Saturn's innermost D ring. The possibility of some constituents, especially more complex organic species, being products of photochemistry in Saturn's upper thermosphere cannot be excluded. We rule out contamination from previous INMS targets as the source of this material since the spectra returned

from all targets differ significantly in certain regions. Additional INMS observations near Saturn's F ring and at higher altitudes between Saturn and the D ring strengthen the idea that this material is native to the rings. Spectra from these orbits are much lower in signal, however mass channels that are consistently above the noise level include channels associated with H_2, CH_4, 28 amu (mostly CO/N_2), and CO_2. Although isotopic values can be deduced from our best fitting models, we do not report any isotopic measurements since these measurements were taken in Saturn's diffuse uppermost atmosphere which makes it difficult to discern any meaningful isotopic information.

The prevalence of non-water ices in the spectrum that seem to be native to the rings is a surprising result from INMS analyses. We speculate that the volatility and proton affinity of these species could be playing a role in the measured abundances. Once a molecule is liberated from a ring particle via an energetic event, its ability to recondense back onto a ring particle is dictated by its proton affinity and volatility. A species with a higher proton affinity is more likely to be protonated after liberation from a ring particle, which would cause that species to evade detection by INMS in CSN mode. A more volatile species, defined by its sublimation pressure curve, will have a more difficult time recondensing back onto a ring particle and be preferentially lost into Saturn. In our analyses, the most prominent non-native species (e.g., CH_4, N_2, CO) are also the species with lower proton affinities and higher sublimation pressures at ring relevant temperatures. Conversely, H_2O has a higher proton affinity and lower sublimation pressure, making it easier for H_2O molecules to recondense back onto a ring particle after liberation or be lost into Saturn's

atmosphere in charged form. Additionally, it is likely that the majority of ring material measured by INMS is predominantly from the D ring, which is known to be darker in appearance and dirtier (i.e., lower relative content of H_2O) than the bulk of the rings. Measuring the composition of Saturn's diffuse rings is also a notoriously difficult task. Thus, it's possible that these minor species in the D ring have simply eluded detection until now.

8.4 Diffusion of ring material into Saturn's atmosphere

In Chapter 7 we quantify the influx of ring material into Saturn's upper atmosphere using our 1-D diffusion model as first detailed in Yelle et al. (2018). For atmospheric entry, which probed deeper into Saturn's atmosphere and detected and increase in temperature at depth, we adopt a Bate's temperature profile for the thermosphere (Bates, 1951). All other orbits measured the isothermal region of Saturn's thermosphere and we determine the isothermal temperature based on the H_2 density profile. Our derived temperature values, which range from 340 to 372 K, are consistent with recent UV occultation measurements reported in Koskinen et al. (2013), Koskinen et al. (2015), and Koskinen and Guerlet (2018).

Using the diffusion equation and modifying the vertical coordinate into units of gravitational potential we are able to determine the influx of exogenous material into Saturn's atmosphere. The total influx of material from the rings amounts to 6.9×10^{13} to 2.3×10^{14} m^{-2}s^{-1}, which translates to a mass

deposition rate of 2.2 to 7.4 $\times 10^4$ kg/s of material entering Saturn's atmosphere from the rings. Our results are consistent with other recent analyses of the same data set (Waite et al., 2018; Perry et al., 2018) and are much higher than in situ measurements taken during the same orbits with MIMI and CDA aboard Cassini. These other instruments detect nanograins and dust particles much larger in mass than the neutral gas molecules detected by INMS and our results suggest that the material measured by INMS may be representative of the bulk of ring material entering Saturn's atmosphere.

INMS recorded a significant amount of ring material entering Saturn's atmosphere that would deplete the D ring of all material on the order of thousands of years. The unsustainable deposition rates calculated in our analysis suggest that this is likely a transient phenomenon due to a recent perturbation in the D ring. This hypothesis is supported by observations of recent D ring perturbations such a the D68 ringlet disruption noted in Hedman et al. (2014).

8.5 Future work

Without Cassini's presence in the Saturn system, future in situ measurements of this region may be decades away. We must rely on ground and space based observatories such as the Atacama Large Millimeter Array (ALMA) and the James Webb Space Telescope (JWST) to help illuminate the many outstanding questions pertaining to Saturn's ring-atmosphere coupling. ALMA's unprecedented spatial and spectral resolution at radio wavelengths can provide high resolution mapping to determine the latitudinal distribution of CO, HCN,

H$_2$O, and other minor species in Saturn's atmosphere that may contribute to our understanding of ring-atmosphere interactions in a similar manner to the Herschel Space Observatory which ceased operation in 2013 (Hartogh et al., 2011; Cavalié et al., 2019). ALMA and other radio observatories are also capable of measuring the thermal emission as well as the forward and backward scattering efficiency of ring particles, properties that could be useful in determining composition (see e.g., Zhang et al. (2017a), Zhang et al. (2017b), and Zhang et al. (2019)).

JWST is equipped with filters and other advanced optics that will allow for a significant reduction in noise and an increased spatial resolution compared to the Hubble Space Telescope and other observatories operating at similar wavelengths. This will greatly improve thermal mapping of the rings. The unprecedented collecting area and NIR spectrometer aboard JWST will allow for high resolution spectra of faint objects such as the rings and will also be able to observe in the 5 to 8 μm region, a region that the instruments aboard Cassini could not observe. Furthermore, JWST will be capable of observing the 10 μm region which may provide the first detection of silicate absorption from the rings and yield crucial insight into the rings' non-water ice component (Tiscareno et al., 2016).

Photochemical models of Saturn's thermosphere are severely underdeveloped due to the lack of compositional measurements of this region to constrain models. Photochemical modeling of this region utilizing the results presented here is crucial in understanding the processes at play in Saturn's thermosphere which could have implications for cloud and haze production

in the upper atmosphere. Recent results by Chadney et al. (submitted) have already highlighted the significance of external CH_4 on the chemical inventory of Saturn's thermosphere using results from our INMS analysis.

8.6 Final thoughts

As with any successful and revolutionary planetary mission, the Cassini spacecraft bestowed on the community an extraordinary breadth of new knowledge related to the Saturn system and, importantly, generated a multitude of new, unanswered questions. The results returned from INMS raise new questions regarding the compositional inventory and chemical evolution of Saturn's ring system, especially the origin and fate of the elusive non-water ice material in the rings. The unsustainable influx of material into Saturn from the rings reminds us that this is an interconnected system with many mysteries still to be solved. The planet, rings, satellites, and dynamic plasma environment surrounded by Saturn's magnetic field influence the dynamics, structure, and evolution of the system in processes that are not entirely known. We have made significant strides in understanding the Saturn system since Cassini's arrival and these unanswered questions provide many enticing reasons to one day return to this unique region of our solar system. There are currently no plans to return to the system with a spacecraft dedicated to studying Saturn's atmosphere and rings, however Cassini's legacy will live on in missions like Dragonfly, a mission predicated largely on the wealth of understanding gained from the spacecraft and its Huygens probe at Titan. It is clear that Cassini's success will continue to inspire for generations to come.

References

Bates, D. R. (1951). "The temperature of the upper atmosphere". In: *Proceedings of the Physical Society. Section B* 64.9, p. 805.

Cavalié, Thibault, V Hue, Paul Hartogh, R Moreno, E Lellouch, H Feuchtgruber, Christopher Jarchow, T Cassidy, LN Fletcher, F Billebaud, et al. (2019). "Herschel map of Saturn's stratospheric water, delivered by the plumes of Enceladus". In: *Astronomy & Astrophysics* 630, A87.

Chadney, JM, TT Koskinen, X Hu, M Galand, P Lavvas, YC Unruh, J Serigano, SM Hörst, and RV Yelle (submitted). "Energy deposition in Saturn's equatorial upper atmosphere". In: *Submitted to Icarus*.

Cui, J., R. V. Yelle, V. Vuitton, J. H. Waite, W. T. Kasprzak, D. A. Gell, H. B. Niemann, I. C. F. Müller-Wodarg, N. Borggren, G. G. Fletcher, et al. (2009a). "Analysis of Titan's neutral upper atmosphere from Cassini Ion Neutral Mass Spectrometer measurements". In: *Icarus* 200.2, pp. 581–615.

Cui, J., R. V. Yelle, D. F. Strobel, I. C. F. Müller-Wodarg, D. S. Snowden, T. T. Koskinen, and M. Galand (2012). "The CH_4 structure in Titan's upper atmosphere revisited". In: *Journal of Geophysical Research: Planets* 117.E11.

Gautier, T., J. Serigano, J. Bourgalais, S. M. Hörst, and M. G. Trainer (2020). "Decomposition of electron ionization mass apectra for space application using a Monte-Carlo approach". In: *Rapid Communications in Mass Spectrometry* 34.8, e8684.

Hartogh, P, E Lellouch, R Moreno, D Bockelée-Morvan, N Biver, T Cassidy, M Rengel, C Jarchow, T Cavalié, J Crovisier, et al. (2011). "Direct detection of the Enceladus water torus with Herschel". In: *Astronomy & Astrophysics* 532, p. L2.

Hedman, M. M., J. A. Burt, J. A. Burns, and M. R. Showalter (2014). "Noncircular features in Saturn's D ring: D68". In: *Icarus* 233, pp. 147–162.

Koskinen, T. T. and S. Guerlet (2018). "Atmospheric structure and helium abundance on Saturn from Cassini/UVIS and CIRS observations". In: *Icarus* 307, pp. 161–171.

Koskinen, T. T., B. R. Sandel, R. V. Yelle, D. F. Strobel, I. C. F. Müller-Wodarg, and J. T. Erwin (2015). "Saturn's variable thermosphere from Cassini/UVIS occultations". In: *Icarus* 260, pp. 174–189.

Koskinen, T. T., B. R. Sandel, R. V. Yelle, F. J. Capalbo, G. M. Holsclaw, W. E. McClintock, and S. Edgington (2013). "The density and temperature structure near the exobase of Saturn from Cassini UVIS solar occultations". In: *Icarus* 226.2, pp. 1318–1330.

Perry, M. E., J. H. Waite, D. G. Mitchell, K. E. Miller, T. E. Cravens, R. S. Perryman, L. Moore, R. V. Yelle, H-W Hsu, M. M. Hedman, et al. (2018). "Material flux from the rings of Saturn into its atmosphere". In: *Geophysical Research Letters* 45.19, pp. 10–093.

Tiscareno, Matthew S, Mark R Showalter, Richard G French, Joseph A Burns, Jeffrey N Cuzzi, Imke de Pater, Douglas P Hamilton, Matthew M Hedman, Philip D Nicholson, Daniel Tamayo, et al. (2016). "Observing planetary rings and small satellites with the James Webb Space Telescope: science justification and observation requirements". In: *Publications of the Astronomical Society of the Pacific* 128.959, p. 018008.

Waite, J. H., R. S. Perryman, M. E. Perry, K. E. Miller, J. Bell, T. E. Cravens, C. R. Glein, J. Grimes, M. Hedman, J. Cuzzi, et al. (2018). "Chemical interactions between Saturn's atmosphere and its rings". In: *Science* 362.6410, eaat2382.

Yelle, R. V., J. Serigano, T. T. Koskinen, S. M. Hörst, M. E. Perry, R. S. Perryman, and J. H. Waite (2018). "Thermal structure and composition of Saturn's upper atmosphere from Cassini/Ion Neutral Mass Spectrometer measurements". In: *Geophysical Research Letters* 45.20, pp. 10–951.

Zhang, Z, AG Hayes, MA Janssen, PD Nicholson, JN Cuzzi, I de Pater, DE Dunn, PR Estrada, and MM Hedman (2017a). "Cassini microwave observations provide clues to the origin of Saturn's C ring". In: *Icarus* 281, pp. 297–321.

Zhang, Z, AG Hayes, MA Janssen, PD Nicholson, JN Cuzzi, I de Pater, and DE Dunn (2017b). "Exposure age of Saturn's A and B rings, and the Cassini Division as suggested by their non-icy material content". In: *Icarus* 294, pp. 14–42.

Zhang, Z, AG Hayes, I de Pater, DE Dunn, MA Janssen, PD Nicholson, JN Cuzzi, BJ Butler, RJ Sault, and S Chatterjee (2019). "VLA multi-wavelength microwave observations of Saturn's C and B rings". In: *Icarus* 317, pp. 518–548.

Joseph Serigano IV

<table>
<tr><td>CONTACT
INFORMATION</td><td>Department of Earth and Planetary Sciences
3400 N. Charles St, 301 Olin Hall
Baltimore, MD 21218</td><td><i>Mobile:</i> (631) 943-8573
<i>Email:</i> jserigano4@jhu.edu</td></tr>
</table>

<table>
<tr><td>EDUCATION</td><td>Johns Hopkins University, Baltimore, MD
Ph.D. Candidate in Planetary Science</td><td>2017 − Present</td></tr>
<tr><td></td><td>Johns Hopkins University, Baltimore, MD
M.A. in Planetary Science</td><td>2015 - 2017</td></tr>
<tr><td></td><td>Boston University, Boston, MA
B.A. in Astronomy and Physics</td><td>2010 − 2014</td></tr>
<tr><td></td><td>Université de Genève, Geneva, Switzerland
Boston University Geneva Physics Program</td><td>January 2013 − July 2013</td></tr>
</table>

RESEARCH INTERESTS

Interests include in situ and remote observations and modeling of atmospheres of the outer solar system, astrobiology, and design and development of future planetary exploration missions. Previous work has focused on the composition and dynamics of Titan's atmosphere through ground-based submillimeter observations/photochemical modeling. Recent work has focused on a compositional analysis of Saturn's upper atmosphere and rings using data from the Ion and Neutral Mass Spectrometer aboard the Cassini Spacecraft.

RESEARCH EXPERIENCE

Johns Hopkins University, Baltimore, MD   **August 2015 − Present**
Graduate Research Assistant with Professor Sarah Hörst

- Determining the composition and structure of Saturn's upper atmosphere and rings from Cassini/INMS measurements and improving our understanding of ring-atmosphere coupling.

NASA Goddard Space Flight Center, Greenbelt, MD   **June 2014 − August 2015**
Research Scientist with Dr. Conor Nixon

- Spatial and spectral modeling of molecules in Titan's atmosphere using the Atacama Large Millimeter Array (ALMA).

Boston University, Boston, MA   **August 2013 − May 2014**
Research Assistant with Professor Tereasa Brainerd

- Investigating the dependency of host-satellite galaxy interactions on various physical parameters using the Sloan Digital Sky Survey.

CERN, Geneva, Switzerland   **January 2013 − July 2013**
Research Assistant with Dr. Augusto Ceccucci

- Simulation development for a hadron calorimeter (HAC) for the NA62 experiment to determine the effects of calorimeter shape on performance and background suppression.

PROFESSIONAL AFFILIATIONS

American Geophysical Union, Division for Planetary Sciences - American Astronomical Society

PROFESSIONAL SERVICE

Graduate Student President for the Department of Earth and Planetary Sciences at Johns Hopkins University   **2017 − 2018**
Referee for *Icarus*
Executive secretary for NASA PICASSO panel

<table>
<tr><td>TEACHING
EXPERIENCE</td><td>Graduate Teaching Assistant, Johns Hopkins University
AS.020.334: Planets, Life, and the Universe
AS.270.114: Guided Tour: The Planets</td><td>Fall 2017, 2018
Spring 2018, 2019</td></tr>
</table>

Guest lecturer for Planets, Life, and the Universe, JHU (2 lectures)
Guest lecturer for Guided Tour: The Planets, JHU (3 lectures)

<table>
<tr><td>PUBLIC
OUTREACH</td><td>Helped create <i>Titan on a Sphere</i>, a short educational film to increase public understanding of recent scientific discoveries about Titan through the use of NOAA's Science on a Sphere educational program. (https://sos.noaa.gov/datasets/titan-tours/)</td></tr>
</table>

Regular participant in the **_Skype a Scientist_** program intended to expose K-12 classrooms to scientists via online video conference.

<table>
<tr><td>PRESS</td><td>Blog post, Ça Se Passe Là Haut, "Saturne: Les Anneaux Se Désagrègent Vraiment" (June 2020)</td></tr>
</table>

Press Release, NRAO/AUI/NSF, "Organic Molecules in Titan's Atmosphere Are Intriguingly Skewed" (October 2014)

Press Release, NASA GSFC, "NASA-led Study Sees Titan Glowing at Dusk and Dawn" (October 2014)

<table>
<tr><td>WORKSHOPS
& SUMMER
SCHOOLS</td><td>Titan after Cassini-Huygens Workshop. ESAC, Madrid, Spain.
Titan Through Time IV. NASA GSFC, Greenbelt, MD.
Titan Aeronomy and Climate Workshop. Reims, France.
Vatican Observatory Summer School 2016. Albano Laziale, Italy. <i>Water in the Solar System and Beyond.</i>
ESO Planets 2015 Workshop. Santiago, Chile. <i>Ground and space observatories: A joint venture in planetary science.</i></td><td>September 2019
April 2017
June 2016

June 2016

March 2015</td></tr>
</table>

<table>
<tr><td>PUBLICATIONS:
FIRST AND
SECOND AUTHOR</td><td>
[1] Serigano, J., Hörst, S. M., He, C., Gautier, T., Yelle, R. V., Koskinen, T. T., Trainer, M.G., "Compositional Measurements of Saturn's Upper Atmosphere and Rings from Cassini INMS: An Extended Analysis of Measurements from Cassini's Grand Finale Orbits", <i>submitted to JGR Planets</i>
[2] Serigano, J., Hörst, S. M., He, C., Gautier, T., Yelle, R. V., Koskinen, T. T., Trainer, M.G., "Compositional Measurements of Saturn's Upper Atmosphere and Rings from Cassini INMS", <i>JGR Planets</i>, 125, e2020JE006427 (2020)
[3] Gautier, T., Serigano, J., Bourgalais, J., Hörst, S. M., Trainer, M. G., "Decomposition of Electron Ionization Mass Spectra for Space Application using a Monte-Carlo Approach", <i>Rapid Communications in Mass Spectrometry</i>, 34(8), e8684.
[4] Yelle, R.V., Serigano, J., Koskinen, T.T., Hörst, S.M., and 4 others. "Thermal Structure and Composition of Saturn's Upper Atmosphere from Cassini/INMS Measurements", <i>GRL</i>, 45 (2018)
[5] Serigano, J., Nixon, C.A., Cordiner, M.A., and 4 others. "Isotopic Ratios of Carbon and Oxygen in Titan's CO Using ALMA", <i>ApJL</i>, 821, L8 (2016)</td></tr>
<tr><td>PUBLICATIONS:
CO-AUTHOR</td><td>
[6] Chadney, J., Koskinen, T.T., Hu, X., Galand, M., Lavvas, P., Unruh, Y.C., Serigano, J., and 2 others. "Energy Deposition in Saturn's Equatorial Upper Atmosphere", <i>submitted to Icarus</i>
[7] Nixon, C.A., Thelen, A.E., Cordiner, M.A., Kisiel, Z., Charnley, S.B., Molter, E.M., Serigano, J., and 3 others. "Detection of Cyclopropenylidene on Titan with ALMA", <i>AJ</i> 160 (5), 205 (2020)</td></tr>
</table>

[8] Thelen, A. E., Nixon, C. A., Chanover, N. J., Cordiner, M. A., Molter, E. M., Teanby, N. A., Irwin, P.G.J., **Serigano, J.**, and 1 other. "Abundance Measurements of Titan's Stratospheric HCN, HC$_3$N, C$_3$H$_4$, and CH$_3$CN from ALMA Observations", *Icarus*, 319, 417-432 (2019)

[9] Müller-Wodarg, I.C.F., Koskinen, T.T., Moore, L., **Serigano, J.**, and 4 others. "Atmospheric Waves and their Possible Effect on the Thermal Structure of Saturn's Thermosphere", *GRL*, 46, 2372-2380 (2019)

[10] Teanby, N.A. and Cordiner, M.A. and Nixon, C.A. and Irwin, P.G.J. and Hörst, S.M., and Sylvestre, M., **Serigano, J.**, and 3 others. "The Origin of Titan's External Oxygen: Further Constraints from ALMA Upper Limits on CS and CH$_2$NH", *AJ*, 155, 251 (2018)

[11] Thelen, A.E., Nixon, C.A., Chanover, N.J., Molter, E.M., Cordiner, M.A., Achterberg, R.K., **Serigano, J.**, and 3 others. "Spatial Variations in Titan's Atmospheric Temperature: ALMA and Cassini Comparisons from 2012 to 2015", *Icarus*, 307, 380 (2017)

[12] Molter, E.M., Nixon, C.A., Cordiner, M.A., **Serigano, J.**, and 4 others. "ALMA Observations of HCN and its Isotopologues on Titan", *AJ*, 152, 42 (2016)

[13] Cordiner, M.A., Palmer, M.Y., Nixon, C.A., Irwin, P.G.J., Teanby, N.A., Charnley, S.B., Mumma, M.J., Kisiel, Z., **Serigano, J.**, and 2 others. "Ethyl Cyanide on Titan: Spectroscopic Detection and Mapping Using ALMA", *ApJL*, 800, L14 (2015)

[14] Cordiner, M.A., Nixon, C.A, Teanby, N.A., Irwin, P.G.J., **Serigano, J.**, and 8 others. "ALMA Measurements of the HNC and HC$_3$N Distributions in Titan's Atmosphere", *ApJL*, 795, L30 (2014)

INVITED SEMINARS   University of Arizona, Lunar and Planetary Laboratory, Tucson, AZ   *Aug 2020*

CONFERENCE PRESENTATIONS   **Serigano, J.**, Hörst, S.M., He, C., and 3 others, "Compositional Measurements of Saturn's Upper Atmosphere and Rings from Cassini INMS", AAS DPS Meeting, Virtual. Oral presentation (Oct 2020)

Serigano, J., Hörst, S.M., He, C., and 3 others, "Compositional Measurements of Saturn's Upper Atmosphere and Rings from Cassini INMS", AAS DPS Meeting, Virtual. Oral presentation (Oct 2020)

Serigano, J., Hörst, S.M., Yelle, R.V., Koskinen, T.T., He, C., "Investigating the Interactions between Saturn's Upper Atmosphere and Rings from Cassini INMS Measurements", Titan after Cassini-Huygens Workshop, Madrid, Spain. Oral presentation (Sep 2019)

Gautier, T., **Serigano, J.**, Hörst, S.M., Trainer, M.G.,, "Volatiles in Titan's Lower Atmosphere: Reinterpretation of Huygens-GCMS Data", Titan after Cassini-Huygens Workshop, Madrid, Spain. Oral presentation (Sep 2019) *Given on behalf of T. Gautier.*

Serigano, J., Hörst, S.M., Yelle, R.V., Koskinen, T.T., He, C., "Investigating the Interactions between Saturn's Upper Atmosphere and Rings from Cassini INMS Measurements", EPSC-DPS Joint Meeting, Geneva, Switzerland. Oral presentation (Sep 2019) ***Invited talk.***

Gautier, T., **Serigano, J.**, Hörst, S.M., Trainer, M.G.,, "Volatiles in Titan's Lower Atmosphere: Reinterpretation of Huygens-GCMS Data", EPSC-DPS Joint Meeting, Geneva, Switzerland. Oral presentation (Sep 2019) *Given on behalf of T. Gautier.*

Serigano, J., Hörst, S.M., Yelle, R.V., and 6 others, "The Composition and Thermal Structure of Saturn's Upper Atmosphere from Cassini/INMS Measurements", AAS DPS Meeting, Knoxville, TN. Oral presentation (Oct 2018)

Serigano, J., Yelle, R.V., Koskinen, T.T., Hörst, S.M., and the INMS team, "The Composition of Saturn's Upper Atmosphere from Cassini/INMS Measurements", Cassini Science Symposium, Boulder, CO. Oral presentation. (Aug 2018)

Serigano, J., Hörst, S.M., Mandt, K.E., "The Influence of Eddy Diffusion on Ions and Neutral Species in Titan's Upper Atmosphere", Titan Through Time IV, NASA GSFC, Greenbelt, MD. Poster presentation (Apr 2017)

Serigano, J., Nixon, C.A., Cordiner, M.A., and 4 others, "Isotopic Ratios of Carbon and Oxygen in Titan's CO Using ALMA", Titan Aeronomy and Climate Workshop, Reims, France. Poster presentation (Jun 2016)

Serigano, J., Nixon, C.A., Cordiner, M.A., and 4 others, "Observations of CO in Titan's Atmosphere Using ALMA", AAS DPS Meeting, National Harbor, MD. Oral presentation (Nov 2015)

Serigano, J., Nixon, C.A., Cordiner, M.A., and 4 others, "Isotopic Ratios from CO in Titan's Atmosphere Using ALMA", ESO Planets Workshop, Santiago, Chile. Poster presentation (Mar 2015)

Serigano, J., Nixon, C.A., Cordiner, M.A., and 4 others, "Probing Titan's Atmosphere with ALMA", Astrobiology Science Conference, Chicago, Il. Oral presentation (Jun 2015)

Serigano, J., Nixon, C.A., Cordiner, M.A., and 10 others. "Probing Titan's Atmosphere with ALMA", AGU Fall Meeting, San Francisco, CA. Poster presentation (Dec 2014)